City Research Online

City St George's, University of London

Citation: Kumar, R. (2020). Development of novel optical fibre sensors based on upconverting and gold nanoparticles. (Unpublished Doctoral thesis, City, University of London)

Development of Novel Optical Fibre Sensors based on Upconverting and Gold Nanoparticles

Submitted by

Rahul Kumar

Thesis submitted for the degree of Doctor of Philosophy

Supervised by

Professor Tong Sun

and

Professor Kenneth T.V. Grattan

City, University of London
School of Mathematics, Computer Science and Engineering
EC1V 0HB, London, UK
September 2020

Table of Contents

Table of Contents

Dedicated to my grandfather B.D. Mishra

and

parents D.S. Mishra and Geeta Mishra

Table of Figures

Table of Tables

Acknowledgement

First and foremost, I would like to express my heartfelt gratitude to my supervisors Professor Tong Sun and Professor Kenneth Grattan for their technical guidance, financial and moral support that helped me immensely in successfully completing this research programme. It was an honour and a privilege to work under such professional and kind-hearted experts in the field. I have matured as a researcher in both technical and non-technical aspects because of their guidance and erudite inputs during discussions.

I would also like to thank Dr. Lourdes Alwis and Leonardo Binetti for their continuous support with material characterisation. I also want to thank Dr. Arti Agrawal for introducing me to City Doctoral Fellowship and co-supervising me throughout the first year of my PhD degree.

Special thanks to my fellow researchers, Dr. Matthias Fabian, Dr. Miodrag Vidakovic, Dr. Hien Nguyen, Dr. Bruno Rente, Dr. Kasun Dissanayak, Dr. Souvik Ghosh, Dr. Israt Kabir, Dr. Papiya Dhara and Dr. Sunny Chug for discussions, suggestions and ideas. Without their encouraging words and insightful chats, my journey would have been a much longer and a lonely one.

I would like to thank my parents and siblings for their sacrifices and keeping me away from family responsibilities, which enable me to concentrate on my research. I would like to extend my warmest gratitude to my wife Nusrat Tamanna for making my stay in UK, a memorable one. Without her love, support and encouragement, I could not have finished this thesis on time.

Finally, I would like to pay my salutations to sages of India who preserved the spiritual knowledge and transferred it selflessly from one generation to another. Be it yoga or meditation, or devotional songs, these techniques kept me calm and focussed through thick and thin part of my journey.

In one’s life, there are contributions from many people, and it is not possible to mention everyone here. However, I thank them all.

Copyright Declaration

Abstract

In this work, the Upconverting and Gold nanoparticles were chemically synthesized, coated on the multimode optical fibres and with their performance were evaluated for sensing two keys environmental parameters, temperature and heavy metals present in the aqueous medium, each of which has shown competitive performance with current devices.

In Upconverting Nanoparticles (UCNPs – $NaYF_4$: (18%) Yb^{3+}, (2%) Er^{3+}), thermally coupled green band emission from excited Er^{3+} ions was used to create optical thermometer, working in the useful range of 295 K – 473 K, with a sensitivity of 4.91×10^{-3} K^{-1}, a temperature resolution of ± 2.7 K and response time of ~ 5 seconds. The mixture of UCNPs and polydimethylsiloxane shows an excellent linear response ($R^2 = 0.991$) in entire working range of the sensor. The highlights of the developed sensor are its linear response and low temperature synthesis where the required synthesis temperature is around 400 K less than the previously reported Er^{3+} doped glass-based temperature sensors.

The colloidal solution of Gold Nanoparticles (GNPs) was synthesised, coated on the optical fibre and suitably functionalized with MUA ($HS(CH_2)_{10}CO_2H$) to make them selective towards heavy metal ions present in the aqueous solution. The concentration of the heavy metal can be determined from the link between binding rate and the shift of the localized surface plasmon resonance wavelength. The Pb^{2+} ion sensitivity of the sensor thus created has been determined to be 0.28 nm/mM.

At last, several colloidal solutions of Gold Nano Rods (GNRs) were synthesised, and their quality was determined by developing an algorithm to readily calculate the aspect ratios (ARs) distribution. This is achieved by theoretically fitting the localised longitudinal plasmon resonance of GNRs obtained by UV-visible spectroscopy. The ARs distribution obtained from the use of the algorithm developed have shown good agreement with those theoretically generated one as well as with the previously reported results. The comparison of obtained results with experimentally derived results from the use of expensive transmission electron microscopic images and dynamic light scattering technique shows that the algorithm developed offers a fast and thus potentially cost-effective method to determine the quality of the synthesized GNRs.

Glossary of Abbreviations, Symbols and Chemicals

Abbreviations:

AFM	Atomic Force Microscopy
AR	Aspect Ratio
ATR-FTIR	Attenuated Total Reflection Fourier-Transform InfraRed spectra
BPO	Bellman's dynamic programming Principle of Optimality
BSA	Bovine Serum Albumin
CEA	Carcinoembryonic Antigens
CR	Cross-Relaxation
CR	Cooperative Luminescence
CS	Cooperative Sensitization
DI water	Deionized water
DLS	Dynamic Light Scattering
Dox	Antitumor Drug Doxorubicin
ECL	Electrogenerated chemiluminescence
EDS	Energy Dispersive Spectroscopy
EELS	Electron Energy Loss Spectroscopy
EPR	Enhanced Permeation and Retention
ES	Electrical Sensors
ESA	Excited State Absorption
ETU	Excited State Upconversion
FBGs	Fibre Bragg Gratings
GNPs	Gold Nanoparticles (represents Gold nanospheres unless stated otherwise)
GNRs	Gold Nanorods
GSA	Ground State Absorption
J	Total Angular Momentum
L	Orbital Angular Momentum
L-LSPR	Longitudinal Localised Surface Plasmon Resonance

LED	light-emitting Diodes
LN	Lead Nitrate
LPGs	Long Period Gratings
LSA	Least Squares Approximation
LSPR	Longitudinal Surface Plasmon Resonance
LSS	liquid–solid–solution
MOFs	Metal Organic Frameworks
NIR	Near Infrared
OF	Optical Fibre
OFS	Optical Fibre-based Sensors
PA	Photon Avalanche
PDT	Photo-dynamic therapy
PL	Photoluminescence
PTT	Photo-thermal Therapy
QDs	Quantum Dots
RB	Rose Bengal dye
RE	Rare-Earth
RI	Refractive Index
S	Total Spin
SEM	Scanning Electron Microscope
SET	Successive Energy Transfer
SSE	Summed Square Error
STEM	Scanning Transmission Electron Microscope
STM	Scanning Tunneling Microscope
T-LSPR	Transverse Localised Surface Plasmon Resonance
TCL	Thermally Coupled Radiative Energy Levels
UCNPs	Upconverting Nanoparticles
UCNPs-PDMS	Upconverting Nanoparticles - Polydimethylsiloxane
W_{S-A}	Energy Transfer Probability
XRD	X-ray Diffraction

Glossary of Abbreviations and Chemicals

Symbols :

h	Plank Constant
c	Speed of Light
n	Refractive Index
τ_S	Intrinsic Lifetime
r_{S-A}	Distance between sensitizer-activator
Q_{abs}	Integrated absorption cross-section of the activator
$f_{em}^{S}(E)$	Normalized emission line-shaped function of the sensitizer
$f_{abs}^{A}(E)$	Normalized absorption line-shaped function of the activator
k_{nr}	Non-radiative relaxation rate constant
ΔE	Energy difference between populated level and next lower energy level
$\hbar$	Reduced Plank Constant
ω	Angular frequency of the radiative transitions
k_B	Boltzmann’s constant
δE	Error in ΔE aross temperature
I_S	Area under the emission intensity curve over the wavelength range 532.8 nm to 562 nm
I_H	Area under the emission intensity curve between wavelength 514 nm and 532.3 nm
λ	Wavelength
T	Temperature
δI_H	Standard error in I_H
δI_S	Standard error in I_S
S_A	Absolute thermal sensitivity
S_R	Relative thermal sensitivity
R	The ratio of the integrated emission intensities of the green bands
g	Degeneracy of the given energy level

A	Emission cross-section
t_{90}	Time taken to reach 90% of saturated level
t_{10}	Time taken to reach 10% of saturated level
γ	Absorption coefficient of the GNRs in the colloidal solution
N	Number of GNRs per unit volume
V	Volume per particle
ε_m	Dielectric constant of the surrounding medium
ε_1	Dielectric constant of real part of the permittivity for the gold
ε_2	Dielectric constant of imaginary part of the permittivity for the gold
$\boldsymbol{A_{\lambda_x}^{exp}}$	Experimentally obtained value of the absorption at λ_x
($W_{S\text{-}A}$)	Energy transfer probability between sensitizer and activator ions

Abbreviations of Chemicals used in this work:

$C_{18}H_{36}$	1-Octadecene
$C_{19}H_{42}NBr$	Cetyltrimethylammonium bromide (CTAB)
C_2H_5OH	Ethanol
$(C_2H_6OSi)_n$	Polydimethylsiloxane (PDMS)
$C_{18}H_{34}O_2$	Oleic acid
C_6H_{12}	Cyclohexane
$C_6H_8O_6$	Ascorbic acid
CH_3OH	Methanol
$ErCl_3{\cdot}6H_2O$	Erbium(III) chloride hexahydrate
$H_2N(CH_2)_3Si(OCH_3)_3$	3-Aminopropyl trimethoxysilane (APTMS)
H_2O_2	Hydrogen peroxide
H_2SO_4	Sulphuric acid
$HAuCl_4.3H_2O$	Chloroauric acid

$HS(CH_2)_{10}CO_2H$	11-Mercaptoundecanoic acid (MUA)
$Na_3C_6H_5O_7.H_2O$	Sodium citrate tribasic dehydrate
$NaBH_4$	Sodium borohydride
$NaOH$	Sodium hydroxide
NH_4F	Ammonium fluoride
$Pb(NO_3)_2$	Lead nitrate
$YbCl_3 \cdot 6H_2O$	Ytterbium (III) chloride hexahydrate
$YCl_3 \cdot 6H_2O$	Yttrium (III) chloride hexahydrate

Chapter 1

Introduction

1.1 Background

Nanoparticles, having a size less than 100 nm in all three dimensions, have been known about for many centuries, if not identified as such. The Lycurgus cup in the British museum, shown in Fig. 1.1, illustrate that even in 4th century AD, Roman craftsmen empirically knew of ways to stain glasses with of gold and silver nanoparticles [1]. In seventeenth century, Kunckel established the industrial manufacturing of stained glass with colloidal particles [2]. However, in 1857 Michael Faradays showed for the first time various practical approaches of synthesizing gold colloidal solutions, thus marking the birth of modern colloidal chemistry [3]. The advancement of quantum mechanics and the consequently burgeoning of various nanoscale characterization instrumentation such as Transmission Electron Microscopy (TEM), X-ray diffraction and Raman Spectroscopy has, in last 50 years, given better insight into size related thermal, electrical, mechanical and optical properties of the materials [4].This deeper understanding coupled with better controlled over the synthesis processes have led to several organic and inorganic nanoparticles and their applications in various fields: these being as diverse as imaging, energy harvesting, drug delivery, tissue ablation and sensing [5]. Among the several fields where the nanoparticles have been used, in this work their usage in sensing has been explored because sensing is an important and growing sector. This is evident from the fact that overall projected market value of sensors is expected to reach $320 billion by 2025 with a current compounded annual growth rate of >10% [6].

Figure 1. 1: The Lycurgus cup. Left and right images show the colour of cup when it is illuminated from outside (under reflection) and inside (under transmission) respectively. The man illustrated in cup is the mythological King Lycurgus who is being dragged into the underworld by Greek nymph Ambrosia, disguised in form of vine [1].

Currently, Electrical Sensors (ESs) dominate the global market due to their typically low cost, relative ease of miniaturization and easy integration with available electrical and mechanical devices [7–9]. ESs depend on electrical parameters, typically voltage and current changes, as the basis of their sensing mechanism, therefore, they are not often a natural choice for chemical sensing because of material degradation or corrosion occurring in the presence of aqueous or gaseous media. Further, ESs often can suffer from inherent low signal-to-noise ratios and may be sensitive to external electromagnetic interference. However, many drawbacks of ESs mentioned above can be overcome by the use of Optical Fibre-based Sensors (OFSs), as their transduction effect is entirely optical. In fact, initially optical fibres were developed mainly as optical waveguides as an alternative to copper wires for the benefit of the telecommunication industry. However, they gradually became popular for sensing applications especially after discovery of photosensitivity in optical fibre by Kenneth Hill in 1978 [10]. This has enabled Fibre Bragg Gratings (FBGs) and Long Period Gratings (LPGs) to be written in the core of optical fibre which has made fibre highly sensitive to external strain and temperature. The availability of various types of optical fibres, such as multimode, single mode, small core, hollow core, photonic crystal fibre, and polymer-based fibre have given significant flexibility to the sensor designer. The plethora of different optical fibres make OFSs promising alternatives to ES, particularly for specialist or safety-critical situations where electrical sensors often fail [11,12]. The development of new and better optical fibre sensors for a range of chemical species is important for the burgeoning environmental sensing market and the need for better monitoring, to allow remedial action to be taken to enhance the environment. Consequently, this thesis focuses on developing novel & portable optical fibre sensors for detecting heavy metals in an aqueous medium and with that temperature, using gold nanoparticles and Upconverting Nanoparticles (UCNPs) respectively.

The name “upconverting” suggests in UCNPs, these nanoparticles upconvert Near Infrared (NIR) photons to visible photons by absorbing two or more NIR photons sequentially. Since this upconversion is achieved by sequential absorption of photons rather than spontaneous absorption (unlike in conventional two-photon generation), this effect can be achieved at much lesser source power. The need for a low power source, exploiting the transparency of tissues to NIR light has made these UCNPs a good candidates for biological imaging [13]. However, their sensing capabilities have not as yet been fully explored as relatively very fewer papers have been reported on the potential use of UCNPs based sensors [14] and moreover, their combination with optical fibre is even more limited. The research reported in this thesis has addressed this gap and has targeted the use of UCNPs and UNCPs-polymer composites to develop portable optical fibre-based temperature sensors. The importance of temperature sensing can be judged from the fact that around 75-80% of world’s sensors are temperature sensors [15]. The two main advantages of the sensor addressed in this work over previously reported temperature sensors are: the relatively inexpensive equipment needed for synthesis which can be achieved in conventional chemistry synthesis laboratory and the linear response in the useful range of 298 K to 493 K.

The development of an OFSs to detect heavy metal ions, a species important as it is often seen as a contaminant in the environment (particularly in soil) and is harmful to human health is a further focus of this work. The novelty addressed is targeting ease of manufacture, with an aim to create a simple, portable and robust Longitudinal Surface Plasmon Resonance (LSPR)-based OFS system, operating in reflection mode and designed to detect the lead ions (Pb^{2+}). Out of several heavy metal pollutants, lead is used to demonstrate the sensing capabilities of the developed sensor because lead poisoning is one of the global key issues and as per UN report, every year approximately 0.8 million people die worldwide due to it [16]. The Lead and/or lead based compounds are widely use in various household products such as batteries, cosmetics, polyvinyl chloride toys, tin pots, water pipes and paints [17]. Recently, Nicolie *et al.* published an article highlighting unusual domestic source of lead poisoning [18].

Knowing the aspect ratio (the length divided by the width) distribution of asymmetric Gold Nano Rods (GNRs) in a colloidal solution is important to achieve uniform and long self-assemblies, allowing their usage in various sensing applications [19]. Therefore, the last part of this thesis deals with the determination of aspect-ratio by examining theoretically spectral Longitudinal Localised Surface Plasmon Resonance (L-LSPR) of the spectrum obtained from the UV-Visible spectroscopy of a GNRs' colloidal solutions.

1.2 Aims and objectives of this work

The primary aim of this work is to harness the advantages associated with combining nanoparticles, used as coatings on optical fibre to develop and then evaluate the performance of nanoparticle-based optical fibre sensors for sensing two keys parameters important for better environmental monitoring:

1) temperature (through a simple to fabricate lost cost, low temperature approach) and

2) heavy metals present in the aqueous medium

with the view of creating easy to fabricate, low-cost sensors, competitive in performance with current devices.

Given that primary aim, the major objectives of the work undertaken and reported in this thesis are:

- To conduct a literature review of nanoparticles, their synthesis and characterization methods and determine the state-of-the-art of nanoparticle-based optical fibre sensor research which underpins this work and thus to determine novel methods to measure both temperature and the presence of heavy metals, optimizing the use of resources in so doing.
- To synthesize hexagonal phase UCNPs using a bottom-up approach and subsequently a UCNPs-polydimethylsiloxane composite, prior to using them as the basis of creating a sensing element in a novel optical fibre sensor probe.
- To evaluate the fluorescence emission and thermal response of the developed OFSs and compare their thermal and other performance aspects with those of previously reported Er^{3+}, Yb^{3+}/Er^{3+} doped glasses.
- To synthesize GNPs, coat them on optical fibre to realize reflection-based LSPR optical fibre sensors and evaluate their performance for varying refractive indices.

- To functionalize the GNPs-based LSPR optical fibre sensor probes appropriately to make them selective to heavy metals ions and evaluate their sensitivity for various concentration of Pb^{2+} ions present in the aqueous solution.
- To synthesis GNRs with several different aspect ratios, measure their UV-Visible spectra and use these spectra to determine aspect ratio distribution: thus to evaluate the quality of synthesized GNRs specifically needed for many potential applications for the advanced sensor systems, by developing an appropriate algorithm.
- To summarize the key results obtained throughout the project period, draw conclusions and outline the directions for future research.
- To disseminate the research output to wider audiences through publication in peer reviewed journals and presentation at international conferences.

1.3 Structure of the thesis

The thesis spans into six chapters describing the work carried out to achieve the above set out aims and objectives.

Chapter 1 discuss briefly the background to the work and the gaps in the market, setting out clearly the prime aim and the key objectives and the structure of the thesis.

Chapter 2 focuses on the brief review of nanoparticles, relevant bottom-up synthesis processes and characterization mechanisms. Afterwards, it discusses in detail about the fundamentals of upconversion, choice of dopants, ways to increase upconversion efficiency and previously reported applications. This chapter ends with short discussion on nanoparticles realised from gold and use of LSPR phenomenon for sensing.

Chapter 3 describes the synthesis process undertaken to realise UCNPs and UCNPs-polydimethylsiloxane composite, their coating methodology on multimode optical fibre and experimental setup to realise a practical temperature sensor. This is followed by discussion of the obtained results and finally comparison of the thermal response and other performance issues of the sensors developed, with the previously reported lanthanide doped glass based optical temperature sensors.

Chapter 4 reports the synthesis and characterization of LSPR based GNPs, their coating on the optical fibre and functionalization to make it selective towards heavy metals ions. The response of the developed sensor calibrated with various concentrations of lead nitrate aqueous solution is discussed.

Chapter 5 expounds the algorithm developed to obtained aspect-ratio distribution of GNRs in a colloidal solution from its UV-Vis spectrum. Further, the synthesis process of GNRs for various aspect ratios and the comparison of the results obtained from algorithm with TEM and DLS are presented.

Chapter 6 summarises the thesis with a critical evaluation of aims and objectives stated in Chapter 1, thus highlighting the main achievements of this work. Finally, based on the experience gained while working in the area of nanoparticle based optical fibre sensing, some interesting ideas are been suggested which would be worth pursuing in the future research.

1.4 Summary

The brief background to the subject of nanoparticles, optical fibres-based sensors and an exploration of the “gap in the market”, which led to fixing important aims and objective of this work are discussed in the first section. The next section explicitly delineates the aims and objectives of this work followed by a discussion of the structure of thesis considering in detail, the contents of each chapter.

Chapter 2

Literature review

2.1 Introduction

Nanoparticles, having dimension ≤ 100 nm in all three directions, show size and shape dependent properties such as their optical, magnetic, chemical, and electronic properties, amongst others. These properties coupled with significantly higher surface to volume ratio than that is seen in their bulk counterpart makes them very attractive for several diverse applications including sensing, imaging, drug delivery, security and energy harvesting and electronics, for example.

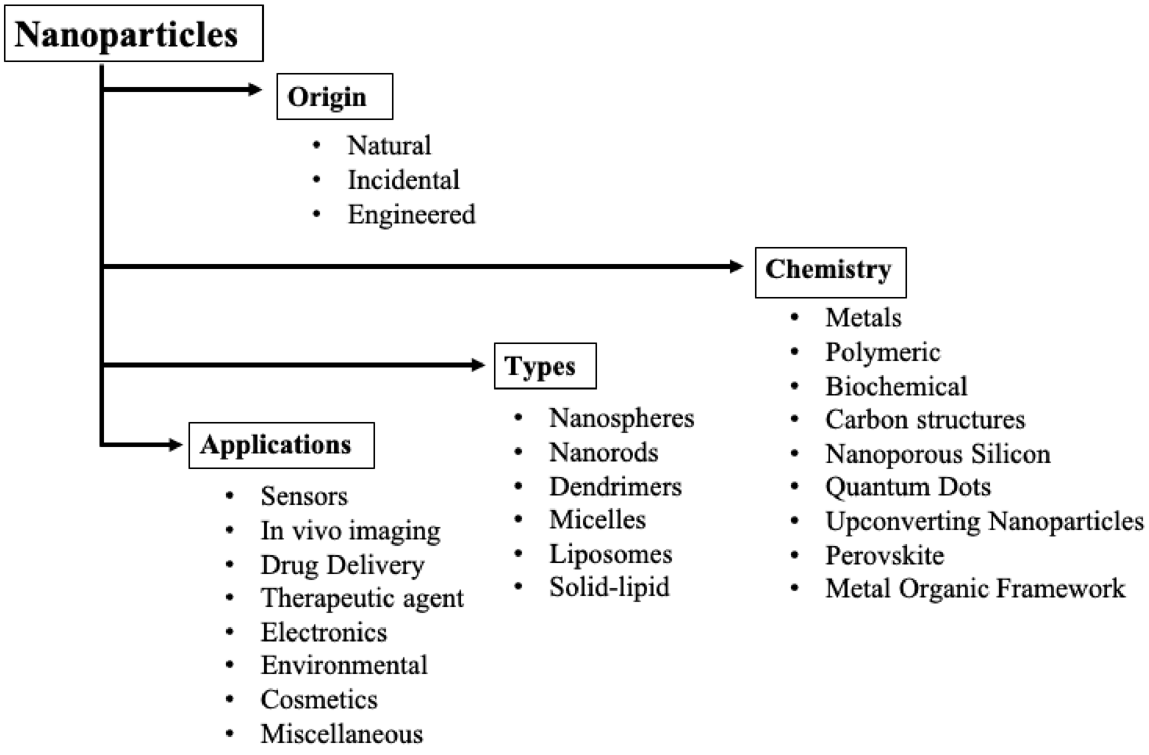

Figure 2. 1: Nanoparticles Classifications [20].

The plethora of available nanoparticles can be classified in a way based on several criteria such as their origin, chemical composition, physical structures (shapes) and applications, for example, as shown in Fig. 2.1. It is not possible to consider here all the available nanoparticles: therefore, in this chapter, several of the most frequently used nanoparticles in the field of sensing and measurement will be introduced and two type of nanoparticles in particular i.e., ‘Upconverting’ and ‘Gold’ nanoparticles will be considered in detail, in the light of their relevance to the work discussed herein. Furthermore, the underlying mechanism of three of the most interesting and relevant ‘bottom up’ synthesis of nanoparticles and a brief overview of the available characterization techniques will also be presented.

The structure of this chapter is as follows: next section is dedicated to nanoparticles, their synthesis and characterisation techniques. The following section to that deals about upconverting nanoparticles, their fundamentals and the several interesting applications reported in the literature during last ten years. The second last section deals about nanoparticles derived from gold and basic of localised surface plasmonic resonance. The last section summarizes the complete chapter.

2.2 Nanoparticles

2.2.1 Classification

A. Quantum dots:

Quantum Dots (QDs) are semiconductor-based nanoparticles having diameter in the range of 2-10 nm [21]. Because of their size being smaller than the exciton Bohr radius, their energy levels show a discrete quantization effect, as seen in Fig. 2.2(a) and consequently this gives rise to their different electrical and optical properties from their bulk counterparts [22]. It can be seen from the schematic shown in the figure that the energy band gap in case of QDs is dependent on the size of the nanoparticles and this increases on decreasing of the size of the QDs. This effect, popularly known as the quantization effect, causes a ‘size-based’ photoluminescence effect, as shown in Fig. 2.2(b), where on decreasing the size of the CdSe QDs considered, the emitted wavelength shifts to higher energy photons, i.e., red to blue wavelength due to increase in energy band gap. A number of the other important QDs that have been reported in literature are those bases on materials such as ZnO, InP, HgS, ZnS and CdS [21]. Unlike organic dyes, QDs do not suffer from the deleterious photobleaching effect and therefore, several applications based on QDs have been reported in the literature such as fluorescence based bioimaging [23], solar cells [24], and optoelectronics devices such as LEDs [25,26], lasers [27] and optical amplifiers [28]. However, a more full potential of the applications and the use of QDs is limited by their cytotoxic effect which is still under study [29].

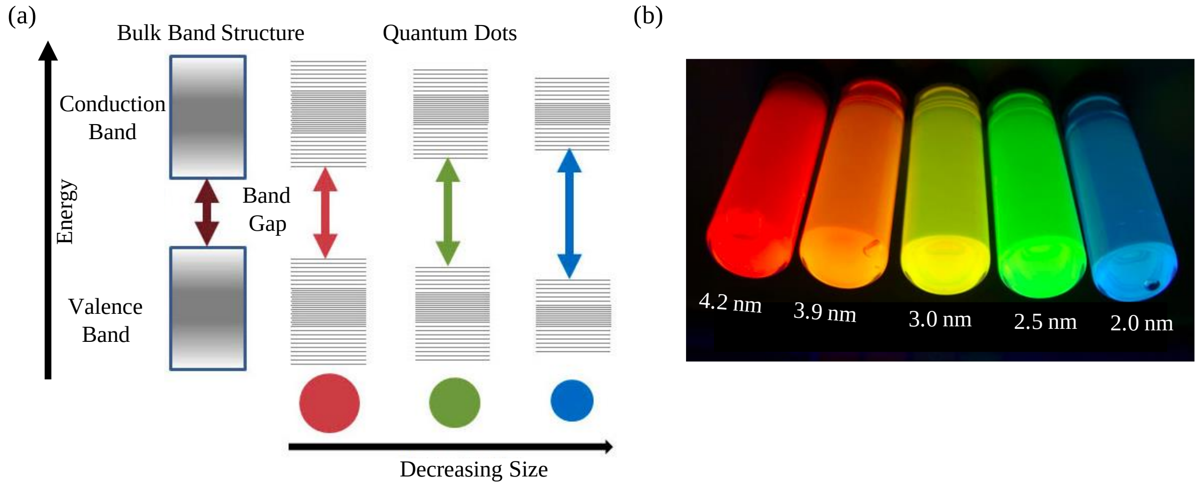

Figure 2. 2: (a) Schematic representation showing the splitting of energy levels in QDs and increase in the band gap due to decrease in size [30]. *(b) Photoluminescence of CdSe QDs showing blue shift of emission on decreasing their diameter. These colloidal solutions are excited with broadband UV source* [31].

B. Metallic nanoparticles

Metal nanoparticles, due to availability of free electrons exhibit unique properties that are not found in other nanoparticles. These free electrons interact with the oscillating electric field of the incident electromagnetic radiation and at the resonant frequency this shows enhanced light absorption, scattering and local confinement of the electric field in the nanoscale region at particles surfaces. This phenomenon, known as LSPR is used in developing several applications in sensing [32], photothermal therapies [33,34], surface enhanced spectroscopies [35], optical waveguides [36] and photocatalysts [37]. The most commonly used nanoparticles are those using Al, Cu, Au and Ag. Magnesium nanoparticles showing plasmonic effects are relatively new in the field [38]. The underlying physics of LSPR is discussed in the second last section of this chapter.

C. Metal halide perovskite

Perovskites are all inorganic or inorganic-organic nanoparticles represented by the chemical formulae ABX_3, where A is an organic or alkali metal cation, B is a divalent metal cation and X is a halide anion binding to both cations, as shown in the schematic in Fig. 2.3(a). They exhibit strong absorption which can be tuned from the visible to NIR region by appropriately changing the anionic and cationic components. Due to the small exciton binding energies, large carrier mobilities, and long and balanced charge diffusion length, they have shown important potential in sensing [39], photovoltaic solar cells, light-emitting diodes (LED), photodetectors and transistors [40–42].

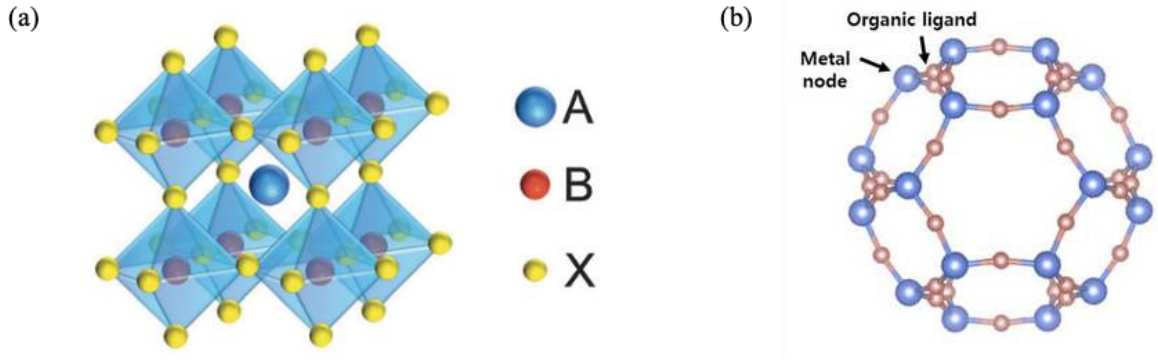

Figure 2. 3: Schematic showing (a) Perovskite having a ABX_3 structures, where A is an organic (e.g. $CH_3NH_3^+$) or alkali metal (e.g. Cs^+) cation, B is a divalent metal cation (e.g. Pb2+, Sn2+) and X is halide anion (e.g. Cl^-, Br^-, I^-)[40] *(b) Metal Organic Frameworks (MOF)* [43].

D. Metal organic frameworks:

Metal Organic Frameworks (MOFs) are also inorganic-organic hybrid crystalline porous structures which consist of a regular array of positively charged metal ions (acting as node) surrounded by organic ligands (acting as linker), thus giving raise to hollow cage-like structure, as shown in Fig. 2.3(b) [44]. To date, more than 20,000 different MOFs have be reported in the literature [43]. Due to their large internal surface area (100 -10000 m^2g^{-1}), MOFs have been used several applications including sensing [45], gas & liquid storage and purification [46] and electrochemical energy storage [47].

E. Upconverting nanoparticles:

Upconverting Nanoparticles (UCNPs) are fluorescent particles which absorb two or more low energy photons, mostly in the Near-Infrared (NIR) and emit a single photon in the visible region [13]. This upconversion process ($\lambda_{absorbtion} > \lambda_{emission}$) differs from traditional two-photon absorption and second-harmonic generation in the sense that the former is a sequential but the latter two are spontaneous processes. Upconversion process being sequential in nature can be achieved at much lesser laser overall power. The two essential requirements for the sequential upconversion, i.e. 'ladder shaped' energy levels and a long excited state lifetime can readily be obtained in rare-earth elements. Therefore, the majority of UCNPs reported in literature are realised using rare-earth ions. The typical UCNP consists of an inorganic crystalline host lattice (which provides an active site of dopants), activator ions (acting as a luminescence centre) and sensitizer ions (used to increase the NIR absorption efficiency; transfer the energy to the activator during de-excitation) and usually represented by “Host matrix: Sensitizer (mol%), Activator (mol%)” [48]. For example, in NaYF$_4$:Yb^{3+} (18%), Er^{3+} (2%), NaYF$_4$ is the host matrix, Yb^{3}+ is the sensitizer, Er^{3+} is an activator and Y^{3+}:Yb^{3+}:Er^{3+} ions are in a mole ratio of 80:18:2. In a few cases, one or more inert or suitably doped shells are grown around the core [49]. In one of such UCNPs was developed by Zhong *et al.*, where they grew two shells on the core [50]. A schematic of nanoparticle is shown in Fig. 2.4(a). By varying the composition of the dopant, the authors have shown that the emitted fluorescence of the developed UCNPs lies the visible spectral range, as shown in Fig. 2.4(b). Considering the relevance of UCNPs in this work, both fundamentals and their key applications are discussed in more details in the next section.

Figure 2. 4: (a) Schematic diagram showing core-shell of UCNPs. Blue, pink and yellow represents the core, the inner shell and the outer shell respectively. (b) Photographs of the luminescence (1-3) NaGdF$_4$:Yb,0.5%Tm,xEr@NaGdF$_4$:Yb@NaNdF$_4$:Yb (x= 0, 0.2, and 1%), (4) NaGdF$_4$:Yb,1% Er@NaGdF4:Yb @NaNdF4:Yb, (5-6) NaGdF$_4$:Yb,0.5%Tm,xEr@NaGdF$_4$:Yb,15%Eu@NaNdF$_4$:Yb (x = 1 and 0.2%), (7-9) NaGdF$_4$:Yb,0.5%Tm@NaGdF$_4$:Yb,xEu@NaNdF$_4$:Yb (x = 15, 10 and 5%). Excitation wavelength is 800 nm. [50].

2.2.2 Synthesis methods

There are several bottom up synthesis methods for nanoparticles described in the literature including inert Gas-condensation, sonochemical (ultrasonic) processing, sol-get decomposition, co-precipitation, microemulsion, chemical precipitation, and hydrothermal/solvothermal synthesis, for example. Out of these processes, the underlying principle of three of these processes i.e. coprecipitation, hydrothermal/solvothermal and seed-mediated method have been described below in details, given their relevance to the synthesis of Upconverting and Gold nanoparticles (and rods) considered in this thesis.

A. *Coprecipitation*

Coprecipitation, as the name suggest, involves the simultaneous occurrence of nucleation, growth coarsening and/or agglomeration when anion and cation solutions are mixed, as depicted in the flowchart in Fig 2.5. Nucleation, where a large number of small particles are produced is a primary and key step. These small particles grow into large particles following an Ostwald ripening process and once the supersaturation condition is reached, then precipitation happens. The precipitate is often filtered and calcinated (heated at high temperature in presence of air or oxygen). Calcination not only increases the crystallinity of material but also removes any impurities present on the surface. The major advantages of the coprecipitation process are: short reaction time, mild reaction conditions, simple protocols and inexpensive equipment [51]. However, this method is not applicable to uncharged species. Further, traces of impurities become precipitated with the product and it does not work well if reactants have very different precipitation rates [51]. Coprecipitation methods are mostly preferred for synthesizing oxide-, fluoride- or oxyfluoride-based nanophosphors like Fe_3O_4 [52].

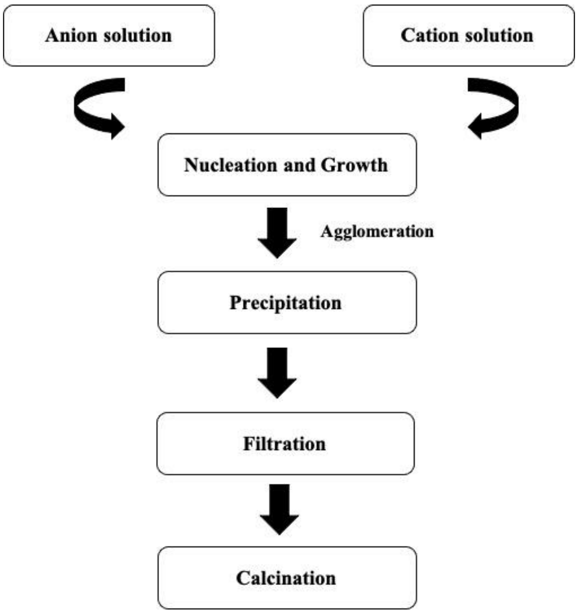

Figure 2. 5: Schematic of the typical co-precipitation method used for nanoparticles synthesis [53].

B. *Seed-Mediated method*

The seed-Mediated method has been traditionally used for synthesizing noble metal nanoparticles with different shapes and sizes [54]. It typically involves two steps: the synthesis of the seed and their growth (by introducing in growth solution containing metal precursors, reducing agents and shape directing agents). This method gives better control over the nanoparticle shape and size by isolating nucleation and growth as two separate synthesis steps, unlike in the process involving spontaneous nucleation and growth such as co-precipitation [55]. This method is used in the current work for synthesizing gold nanorods of various aspect ratios, as described in detail in Chapter 5.

C. Hydrothermal/Solvothermal method

In the hydrothermal/solvothermal method, chemical synthesis is performed in sealed container under high temperature (often above critical point of solvent) and pressure. This is generally carried out in specialized vessels, known as autoclaves. A photograph of one of these autoclaves (25 ml in volume) and a schematic showing cross-section view of the sealed autoclave is shown in Fig. 2.6(a) and 2.6(b) respectively. The difference between the hydrothermal and the solvothermal method is in the kind of solvent used i.e. in hydrothermal method, water is used as solvent whereas in the solvothermal solution nonaqueous solution, mainly organic solutions are used as the solvent [56]. The shape, size distribution and crystallinity of final product can be manipulated by adjusting parameters such as reaction temperature, reaction time, solvent type, surfactant type and precursor type [51].

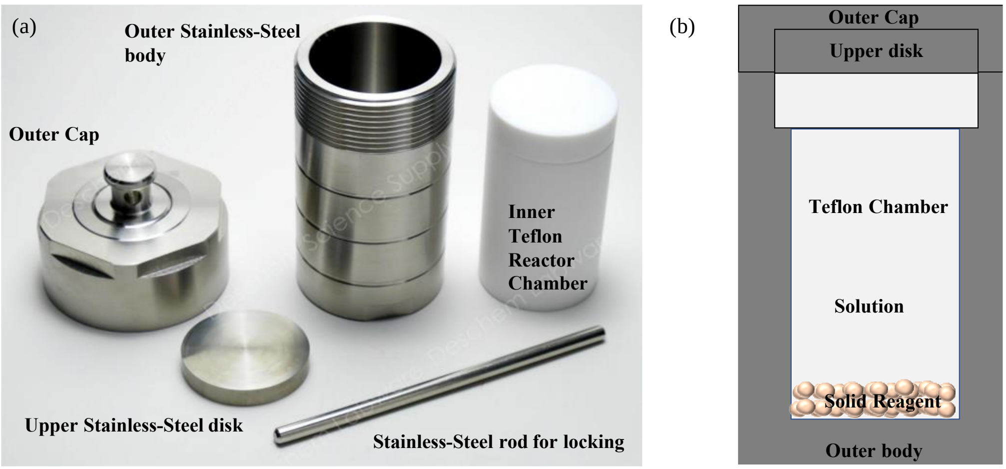

Figure 2. 6: (a) Typical 25 ml autoclave (source: internet). (b) Schematic showing cross-sectional view of sealed autoclave.

Wang *et al.* have reported synthesis of metals, semiconductors, fluorescent, magnetic and dielectric nanoparticles using the hydrothermal reaction [57]. A photograph of some of their synthesized nanoparticles stabilized in cyclohexane is shown in Fig. 2.7(a). In the same work, the authors proposed the phase transfer and separation mechanism occurring at the interfaces of the solid, liquid and solution (liquid–solid–solution (LSS)) as an underlying mechanism of nanoparticle synthesis. For example, for the preparation of the noble metal nanocrystal, 20 ml of aqueous solution containing a noble metal salt like ($AgNO_3$, $HAuCl_4$), 1.6 gm of sodium linoleate ($C_{18}H_{31}NaO_2$), 10 ml ethanol (C_2H_5OH) and 2 ml of linoleic acid ($C_{18}H_{32}O_2$) was added in 40 ml autoclave under agitation. This mixing give raise to formation of three phases: ethanol and linoleic acid (liquid phase), sodium linoleate (solid phase; as it is not soluble), water-ethanol containing noble metal ions (solution phase), as depicted through the schematic in Fig. 2.7(b). The noble metal ions spontaneously went through phase transformation by ion exchange across the interface of sodium linoleate (solid) and water-ethanol solution (solution) and form noble metal linoleate whereas free sodium ions enter into the aqueous phase (marked as 1 & 2 in Fig. 2.7(b)). Subsequently, at the designated temperature (which is different for different metals), the ethanol present in solution and liquid phases reduces the noble metal ions to noble metal at liquid-solid or solid-solution interfaces (marked as 3). Concurrently, the *in-situ* generated linoleic acid adsorbed on the surface of the noble metal nanoparticles with the alkyl chains on the outside, thus making the surface hydrophobic. These nanoparticles being incompatible in hydrophilic surroundings spontaneously settle at bottom of the container (marked as 4) from where they are collected, washed and re-suspended in suitable liquid to achieve stable colloidal solution.

In this work, for the synthesis of UCNPs a solvothermal process is used, as it is safer than hydrothermal process. This is described in detail in Chapter 3.

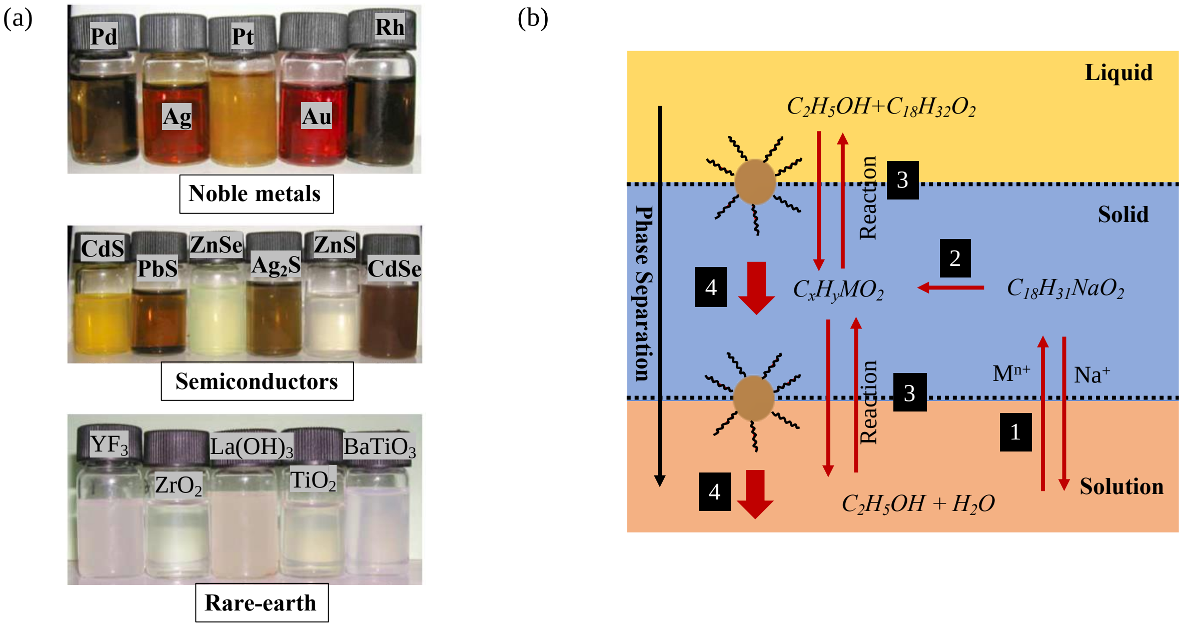

Figure 2. 7: (a) Colloidal solution (2% concentration in cyclohexane solution) of various nanoparticles obtained by hydrothermal process. (b) Schematic showing liquid-solid-solution synthesis strategy achieved by hydrothermal process. Both figures are from reference [57].

2.2.3 Characterization techniques

The characterization techniques for nanoparticles can be broadly classified into two types: imaging and analysing. Table 2.1 gives brief summary of frequently used both types of characterisation techniques.

Table 2. 1: Some important characterization techniques for nanomaterials.

Characterization Techniques	Obtained Features	Comments	Reference
Near field scanning optical microscope (NSOM)	• Size & Shape • Topography	• Resolution: ~ 50 nm	[58,59]
Confocal microscopy	• Size & Shape • Topography • 3D imaging	• Lateral Resolution: 100-200 nm • Vertical resolution: 400-500 nm	[60]
Transmission Electron Microscope (TEM)	• Size • Composition • Crystal structure	• Uses transmitted electrons • Operating voltage: 100kV-3MV • Sample thickness: 50-100 nm • With high resolution TEM (HR-TEM) resolution = 0.02 nm	[61,62]
Scanning Electron Microscope (SEM)	• Size • Microstructure • Composition • Topography • Grain orientation	• Uses secondary and backscattered electrons • Operating voltage: 1kV-3 kV • Thin coating of conducting layer is needed to avoid charging if material is not conducting.	[63,64]

Scanning Transmission Electron Microscope (STEM)	• Surface and interfacial segregation • Chemical composition	• Resolution: At atomic level	[65]
Scanning Tunneling Microscope (STM)	• Image • Chemical composition • Atom movement	• Based on Quantum tunnelling • Atomic level resolution • Used for characterizing conducting surfaces • Common mode of operation: Constant-current mode & Constant-height mode	[66]
Atomic Force Microscopy (AFM)	• Topography • Surface mapping • Mechanical properties	• Variation of STM • Used for characterizing both conduction and non-conducting surfaces • Common mode of operation: Contact mode & Non-contact mode	[67]
Energy Dispersive Spectroscopy (EDS)	• Chemical composition	• Usually associated with SEM, TEM and STEM • Detection limit: 0.1 wt% (bulk materials) • Inner shell's electron is knock out by incident electron beam and relaxation of electrons from outer shell to inner shell produces X-ray.	[68]

Electron Energy Loss Spectroscopy (EELS)	• Chemical composition • Chemical bonding	• Usually associated with TEM and STEM not SEM • Measure energy loss of inelastic scattered electrons	[69]
Infrared (IR) Spectroscopy	• Chemical composition • Chemical bonding	• Fourier transformed infrared (FT-IR) spectroscopy is another variation of this type	[70,71]
Raman Spectroscopy	• Size • Chemical bonding	• Use laser source normally in UV spectrum • Complementary to IR spectroscopy	[72]
X-ray Diffraction (XRD)	• Size • Crystal orientation • Strain	• Use X-ray for measurement, as its wavelength (~ 0.1 nm) is same as atomic spacing of solids. • Based on Bragg's law of diffraction	[73]
Dynamic Light Scattering (DLS)	• Size • Surface potentials	• Measure temporal fluctuations of the light scattering intensity caused by hydrodynamic motions in solution. • Mostly used for colloidal solution	[74]

2.3 Upconverting nanoparticles

2.3.1 Introduction

Photon upconversion, as introduced in the previous section, is a non-linear phenomenon whereby two or more low energy photons are absorbed sequentially by metastable, long lived energy states [75,76]. Nicolaas Bloembergen, a Dutch-American physicist conceived this idea in 1959, during his work on developing an infrared photon detector [77]. He thought of counting infrared photons absorbed sequentially by rare-earth or transition metal ions doped in a crystalline material. Unfortunately, due to lack of coherent pumping source he could not realize this idea at that time, but he shared Noble Prize in Physics in 1981 for his pioneering work in the field of non-linear optics. The first experimental demonstration of upconversion was reported by Francois Auzel in 1966 by using Yb^{3+} ions to sensitize Er^{3+} and Tm^{3+} [78].

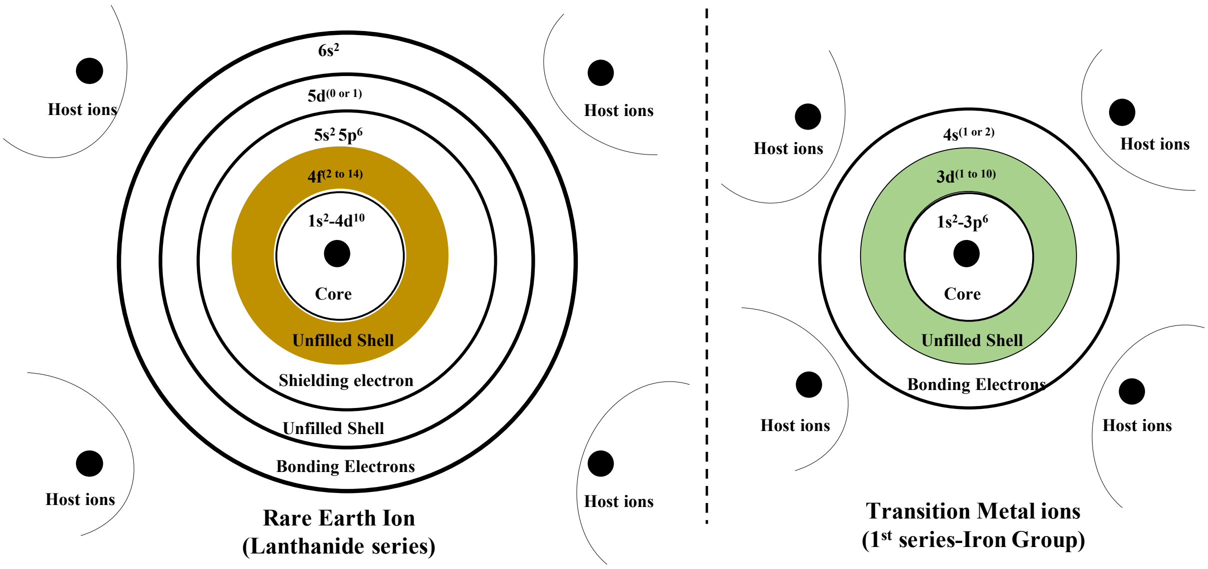

Figure 2. 8: Atomic structure of (Left) Rare-earth ions and (Right) Transition metal ions [79].

The efficient upconversion is achieved using rare-earth elements comprising La, Ce, Pr, Nd, Pm, Sm, Eu, Gd, Tb, Dy, Ho, Er, Tm, Yb and Lu because of a ‘ladder-like’ arrangement of the energy-levels having similar spacing and long-life time of the excited states. These elements are called rare-earth because of the difficulty in extracting them from the earth and their low availability in nature (10^6 times less abundant than silicon) [79]. Some of transition metal ions, such as Ti^{2+}, Ni^{2+}, Mo^{3+} have also shown upconversion, if they are doped in suitable host matrix. However, as shown in Fig. 2.8, in case of lanthanide ions, the optically active electrons present in the 4f shell are partially shielded from influence of external crystal field by its outer shells (5s, 5p, 5d and 6s) electrons. This screening from the external crystal field gives raise to sharp and well-defined spectral features similar to free ion spectra, whereas in contrast, in the case of transition metal ions, the electrons in the unfilled 3d shell are weakly shielded by only a single 4s outer shell. Therefore, optical transitions in this case are strongly coupled to the lattice and susceptible to vibrational motions of the host lattice ions (electron-phonon coupling), thus resulting in broad and undefined spectral features (except in few cases like the R1 and R2 lines of Cr: Al2O3 sharp line is observed) [79].

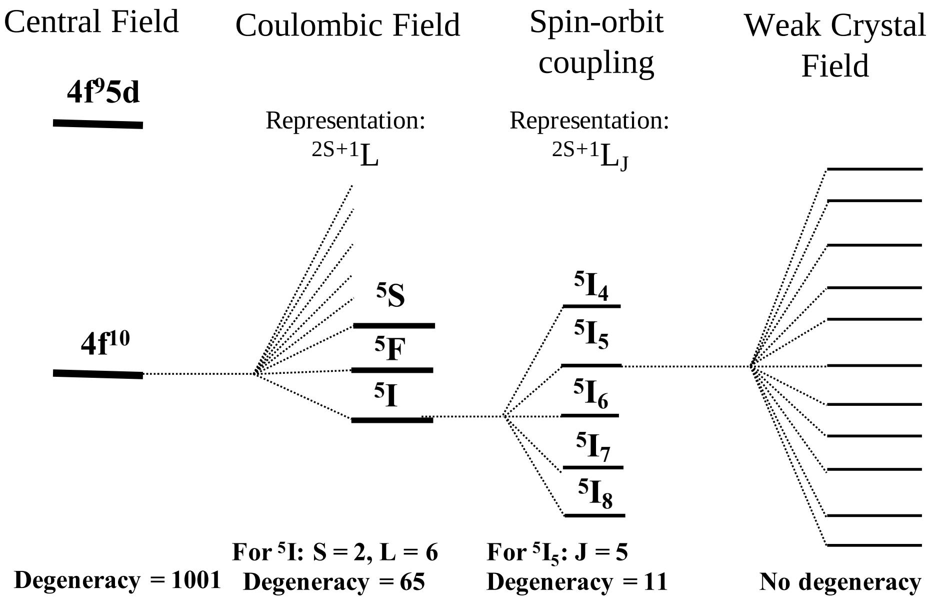

Figure 2. 9: Energy level diagrams showing lifting of degeneracy of trivalent Ln^{3+} ions due to various effects. The energy levels are represented by $^{2S+1}L_J$ where S, L and J represents total spin, orbital momentum and angular momentum quantum number respectively [79].

The ladder shaped levels in $4f^n$ electronic configuration of trivalent lanthanide ions occur due to strong electronic repulsion, spin-orbital coupling and the crystal field. For example, in the case of $4f^{10}$, as shown in Fig. 2.9, the total degeneracy in central field approximation is 1001. However, due to the mutual repulsion of electrons (Coulombic interaction), the degeneracy in the total spin (S) and the orbital angular momentum (L) is removed. The split energy levels are represented by ^{2S+1}L and the degeneracy at each energy level is given by $(2S+1) \times (2L+1)$. The degeneracy at this level, i.e. the degeneracy in the total angular momentum (J) is further removed by interaction between S and L (spin-orbital coupling). The energy level at this stage is represented by $^{(2S+1)}L_J$ and the available degeneracy (2J+1) is finally removed by the weak crystal field. Therefore, in the free atom each level is reduced to (2J+1) degeneracy but only when lanthanide ions are doped in a host crystal, this degeneracy is removed. This highlights the importance of host matrix in upconversion process which will be discussed in the next subsection.

2.3.2 Choice of host lattice

The choice of host lattice is important as the structure of the host lattice determines the distance between the dopant ions, their relative spatial positions, their co-ordination number and types of surrounding anions [76]. In the literature, several oxides, fluoride, molybdate, vanadate, etc. based lattices have been reported. A few of these examples are given Table 2.2. Among the reported lattices, fluoride-based lattices have generally shown high upconversion efficiencies due to their low phonon energies. The low phonon energy supresses the non-radiative losses as a greater number of phonons is needed simultaneously to make the transition, thus increasing the lifetime of the excited states [80].

Table 2. 2: Host lattices used for doping lanthanide ions for upconversion process.

Host Matrix	**Examples**	**References**
Oxide	Y_2O_3, Lu_2O_3, LaO_3, Gd_2O_3	[81–86]
Oxysulfide	Y_2O_2S, Gd_2O_2S, La_2O_2S	[87,88]
Oxyhalide	GdOF, YOF	[89,90]
Phosphate	$LaPO_4$, $LuPO_4$, $YbPO_4$	[91,92]
Molybdate	$La_2(MoO_4)_3$	[93,94]
Tungstate	$NaY(WO_4)_2$	[95,96]
Gallate	$Gd_3Ga_5O_{12}$	[97]
Vanadate	YVO_4	[98]
Fluoride	LaF_3, YF_3, LuF_3, $NaYF_4$, $LiYF_4$, $NaGdF_4$, KY_3F_{10}, KGd_2F_7, $BaYF_5$	[99–106]

Similarly, the cation site with low symmetry yields higher upconversion efficiency because the low site symmetries exert uneven crystal-field around the dopant ion, which not only favours removing the degeneracy of the free-ion states but also increases the 4f-4f transition probabilities [107]. For example, anisotropic hexagonal phased Na(RE)F_4 (RE = Yb^{3+} or Er^{3+} or Y^{3+}) exhibit one order of magnitude enhancement in upconversion in comparison to cubic phased Na(RE)F_4 [108]. It can be seen from their schematic representations, given in Fig. 2.10(a) that in the cubic phase equal number of F^- cubes contain cations and vacancies whereas in the hexagonal phase, an ordered array of F^- ions offers two type cation sites: one occupied by Na^+ and other randomly occupied by Na^+ and RE^{3+} [108]. The transition from the cubic to the hexagonal phase can be controlled by controlling the set of experimental variables such as temperature, nature of solvent, reaction time, concentration of metal precursors and size. For example, a higher temperature and large reaction time favours formation of hexagonal phase whereas smaller size favours cubic phase due to high surface tension. The TEM images of cubic and hexagonal phased $NaYF_4$ co-doped with Yb^{3+} and Er^{3+} are given in Fig. 2.10(b).

Wang *et al.* in the same reference, reported that the phase transition of $NaYF_4$ crystal from cubic to hexagonal can be achieved at much lower temperature and quicker by substituting Y^{3+} (r = 1.159 $\dot{A}$) with larger sized lanthanide ions such as Gd^{3+} (r = 1.193 $\dot{A}$) [108]. They varied the concentration of Gd^{3+} and found that for ion concentration more than 30 mol%, pure hexagonal phased $NaYF_4$ was obtained. However, the maximum upconversion intensity was at 15 mol%, as shown in Fig. 2.10(c). The decrease in intensity with increasing Gd^{3+} doping might be due to severe lattice distortion, defect development and electronic influence of the Gd^{3+} ions.

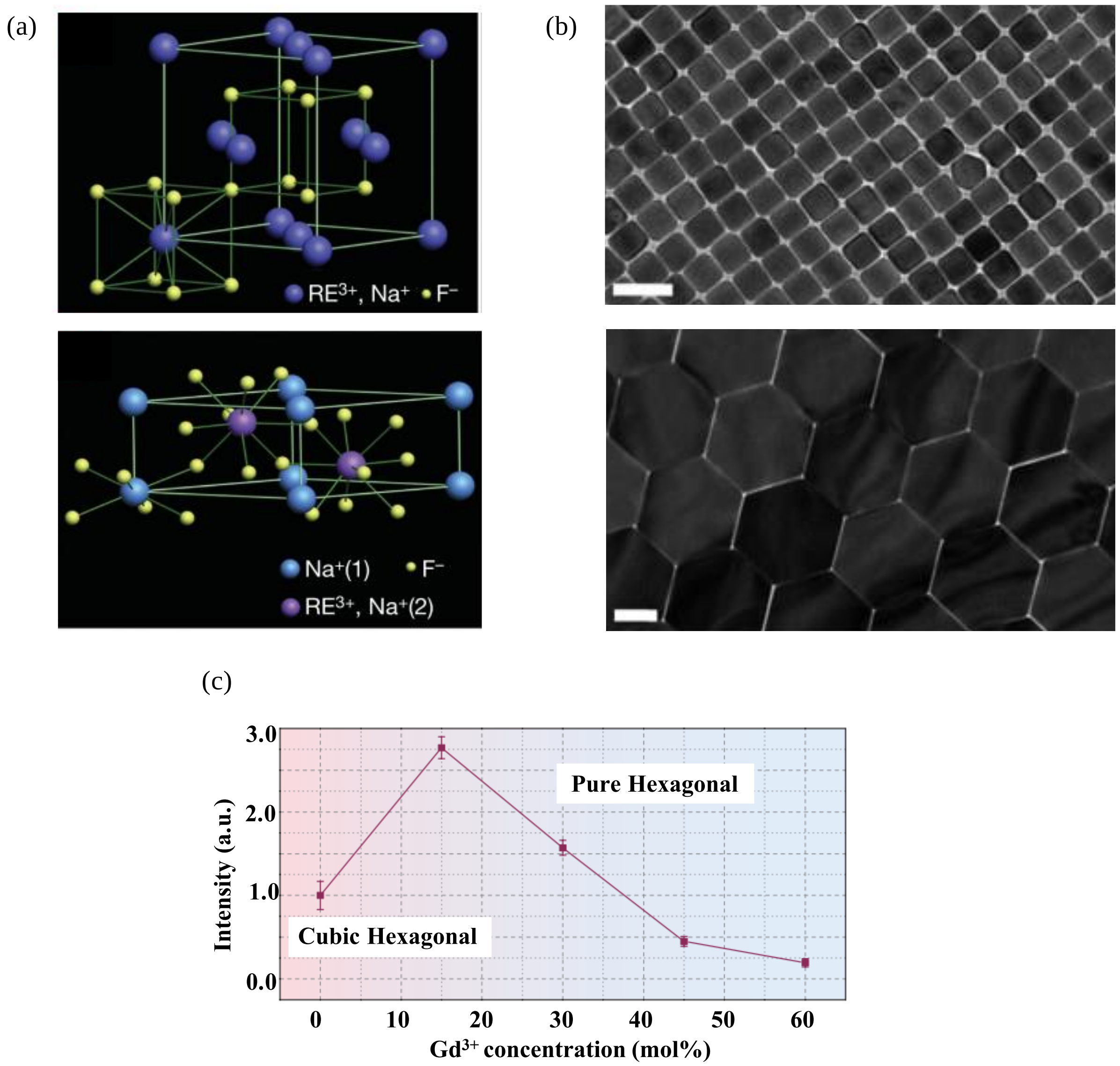

Figure 2. 10: (a) Schematic representation of cubic (top) and hexagonal (bottom) NaREF$_4$ *structure* [108]. *(b) TEM image of cubic and hexagonal phased NaYF*$_4$*:Yb/Er (20/2 mol%). The scale bar represents 100 nm* [109]. *(c) The variation of upconversion intensity, obtained by integrating spectral intensity of emission spectra over wavelength in the range of 400-700 nm with Gd*$^{3+}$ *concentration* [108] .

2.3.3 Choice of dopant

The dopant ions where luminescence takes place, are known as the activator. As shown through simple three levels energy diagrams in Fig. 2.11(a), the electron in the ground state (depicted by $|1\rangle$) of the activator ions absorbs an incoming photon and is raised to the intermediate energy level $|2\rangle$. This process is known as Ground State Absorption (GSA). The intermediate energy level $|2\rangle$, being a metastable state has a longer lifetime and thus the excited electron has an opportunity to absorb another incoming photon (may or may not be of same wavelength) and after its absorption it goes to final energy level $|3\rangle$. This is known as Excited State Absorption (ESA). The radiative transition of electron from level $|3\rangle$ to ground $|1\rangle$ emits the light, having a photon energy almost twice as that of the incoming radiation. In case of Tm^{3+}, it absorbs 4 such NIR incident photons and emits blue fluorescence [13].

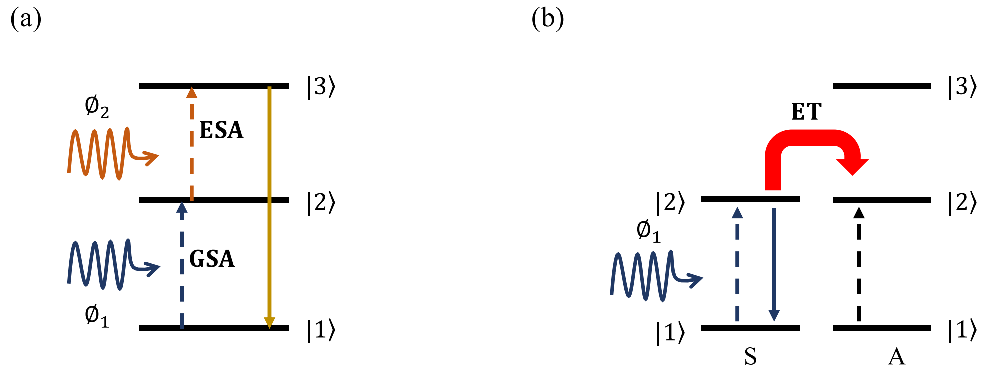

Figure 2. 11: Energy level diagram showing (a) Excited State Absorption (ESA) and (b) Energy Transfer (ET) between Sensitizer (S) and Activator (A) ions. Taken from [110].

The quantum efficiency of ESA is very low due to the Laporte-forbidden intra 4f transition. Therefore, in most of the reported UCNPs, the NIR absorption efficiency of the UCNPs is further increased by co-doping the host-matrix with another set of rare-earth ions known as a sensitizer. The sensitizer ions (e.g. Yb^{3+}) having higher absorption cross-section in NIR regime, absorb the incident wave and undergoes excitation from the ground state to the higher state. These excited electrons while de-exciting back to ground state, transfer the energy to the nearest activator ions, as shown through schematic diagram in Fig. 2.11(b). This transfer of energy from sensitizer to activator is known Energy Transfer (ET). There are several factors which determines the success of ET and according to Dexter's theory [111], the energy transfer probability ($W_{S\text{-}A}$), assuming dipole-dipole interaction is given by Eq. 2.1

$$W_{S-A} = \frac{3h^4c^4}{64\pi^5 n^4 \tau_S} \times \frac{Q_{abs}}{r_{S-A}^6} \times \int \frac{f_{em}^S(E) f_{abs}^A(E)}{E^4}, \tag{2.1}$$

where h, c, n, τ_S and r_{S-A} are Plank's constant, the speed of light, the refractive index, the intrinsic lifetime of the sensitizer and the distance between the sensitizer and activator respectively. Q_{abs} is the integrated absorption cross-section of the activator and the last integration term gives the overlapping area between normalized emission line-shaped function of the sensitizer ($f_{em}^S(E)$) and the normalized absorption line-shaped function of the activator ($f_{abs}^A(E)$) ions. From Eq. 2.1 it can be seen that two critical parameters which determines the energy transfer probability between the sensitizer and the activator ions are r_{S-A} and the spectral overlap between the sensitizer emission and the activator absorption, as shown through the schematic diagram seen in Fig. 2.12(a).

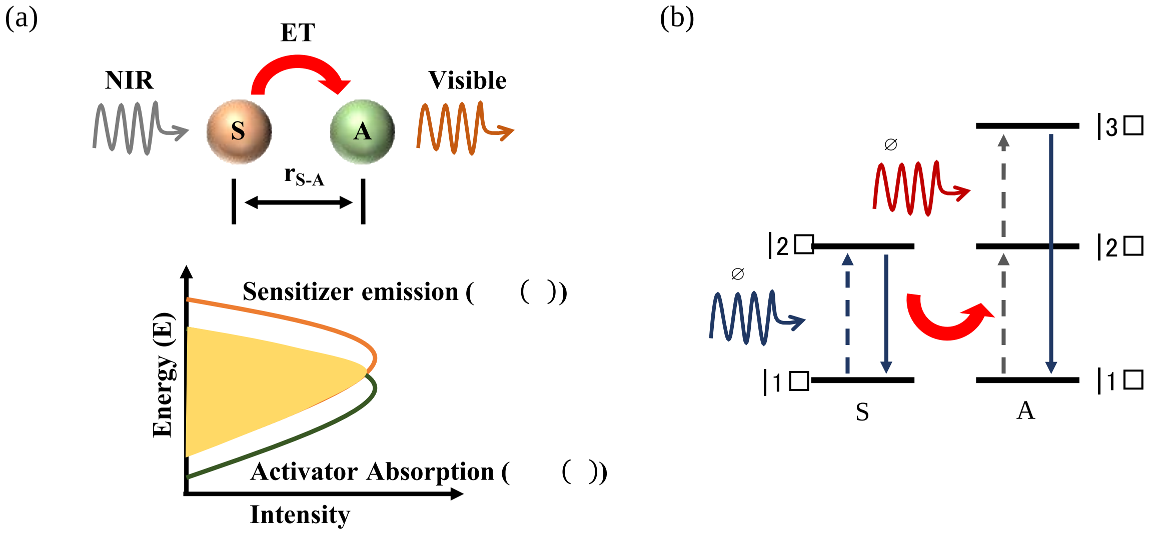

Figure 2. 12: Schematic showing (a) two critical parameters for effective energy transfer, i.e. distance between sensitizer-activator atom and spectral overlap between sensitizer emission ($f_{em}^S(E)$) and activator absorption ($f_{abs}^A(E)$) [112]*. (b) ET followed by ESA* [110] .

There are several variations of ET reported in the literature, these variation depending on the current state of activator ions [110]. For example, if ET is used to excite the electrons already present in intermediate excited state to the final state, then this is known as Excited State Upconversion (ETU). By contrast, in some cases, ET is used to excite the electrons present in ground state of the activator and these excited electrons absorb incoming photons for their successive excitation, as shown schematically in Fig. 2.12(b). In Successive Energy Transfer (SET), sensitizer ions only absorb the incoming photons, and the activator ion is promoted from the ground state to the intermediate state and from the intermediate state to the final state via two consecutive ETs, as shown in Fig. 2.13(a). If the sensitizer and activator ions are identical and both absorb incoming photons as GSA. However, subsequently the activator ion goes to a higher state by ET and the sensitizer goes back to its ground (or lower) energy state after transferring its energy. This is known as Cross-relaxation (CR) and is depicted schematically in Fig. 2.13(b). In Cooperative Sensitization (CS), as shown in Fig. 2.13(c), two sensitizer ions are involved and both transfer the energy simultaneously to a single activator ion, thus promoting it to higher excited state. There is no need for an intermediate metastable state in this case. In cooperative luminescence (CR), the two sensitizers transfer their energy to virtual emitting level which emits upconverted photon on de-excitation, as shown in Fig. 2.13(d).

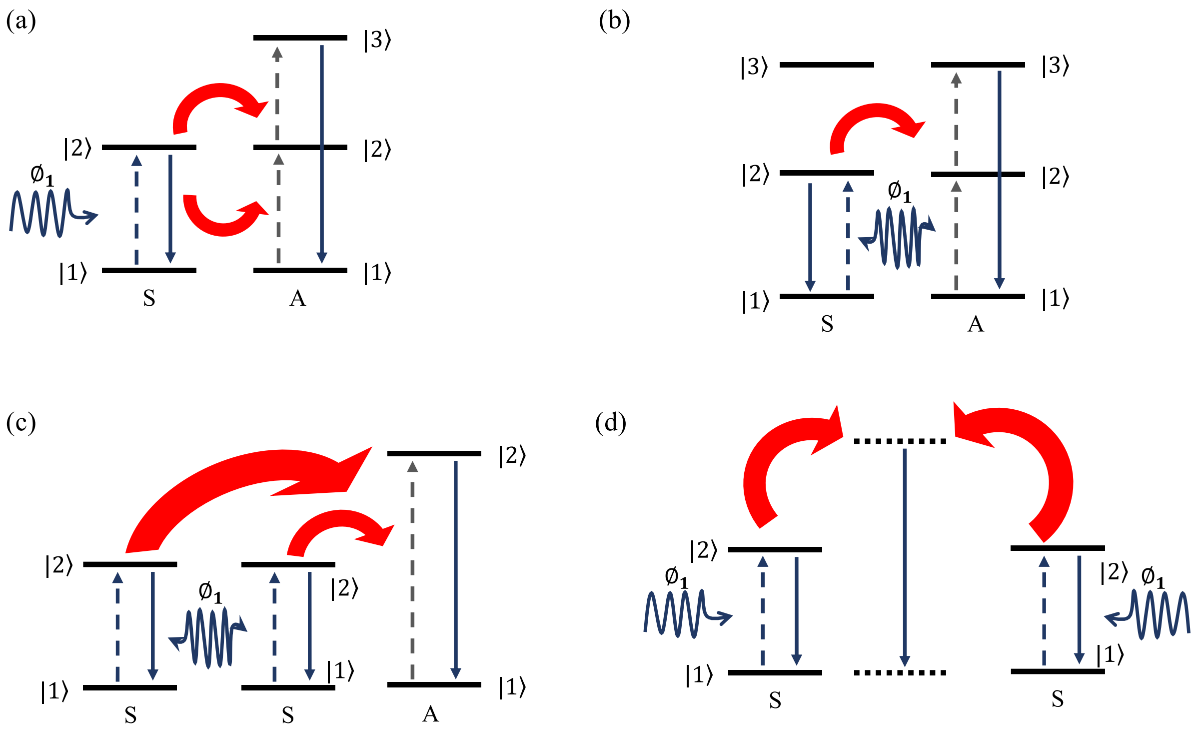

Figure 2. 13: Energy transfer mechanism: (a) Successive Energy Transfer (SET) (b) Cross-relaxation (CR) (c) Cooperative Sensitization (CS) (d) Cooperative Luminescence (CL) [110].

In Photon Avalanche (PA), the sensitizer ion excites to higher state, through GSA and ESA. However instead of de-exciting directly to the ground state, the electron goes back to its intermediate state and transfers the released energy to its neighbouring (identical ion), thus exciting it to intermediate state, as shown in the Fig. 2.14 [113]. These two ions in the intermediate state (say |2⟩) will again cause excitation to the higher state (say |3⟩) by absorbing incoming photons and again de-excite to an intermediate state and in turn this excites two more neighbouring ions to the intermediate states. At this state, there will be four ions in intermediate state and again they will undergo excitation and de-excitation to produce eight ions in the intermediate state. After the end of these several steps, there will be huge reservoir of ions in the intermediate state. This process was first reported by Chivian *et al.* [114] in 1979.

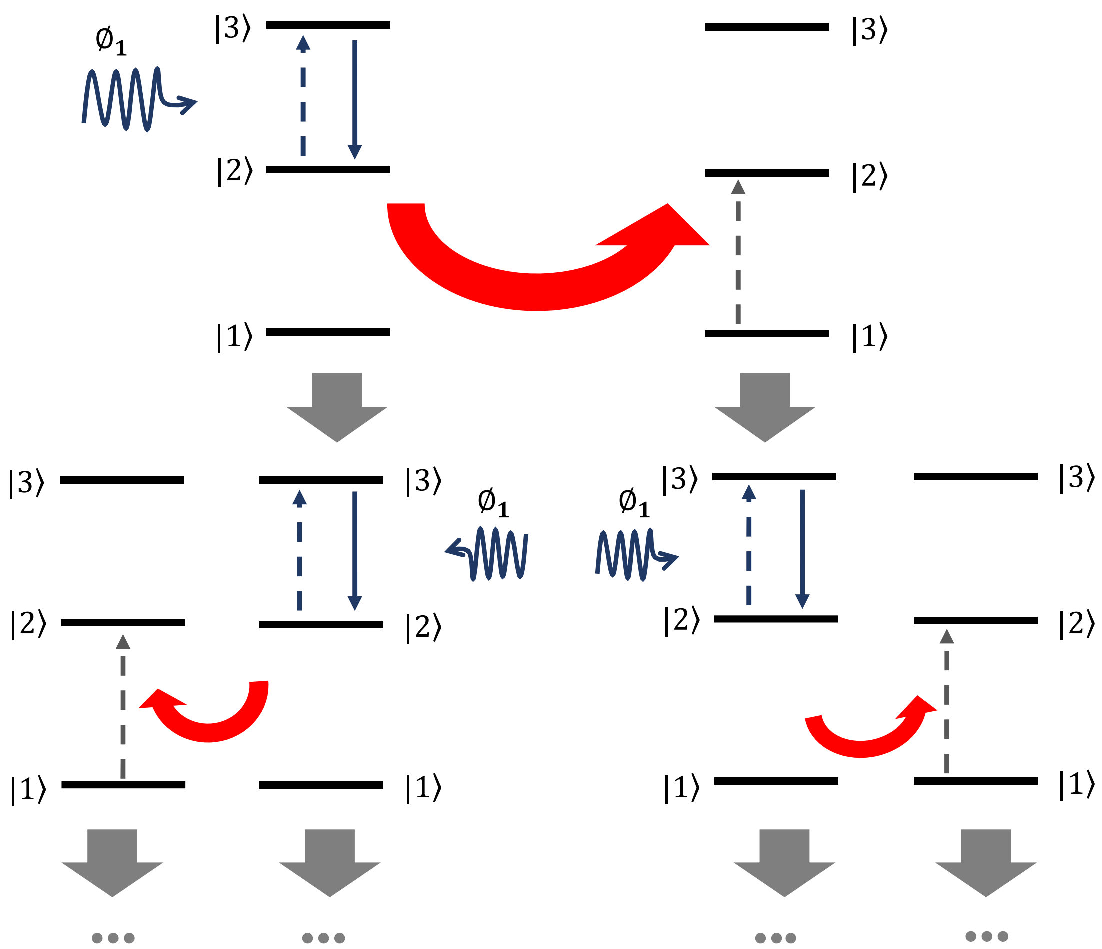

Figure 2. 14: Schematic three levels energy diagram showing Photon Avalanche (PA) mechanism [110].

Out of the upconversion processes mentioned, the SET strongly dominates other processes and Yb^{3+} is often used as sensitizer due to its simple energy level configuration [13]. Furthermore, the concentration of activators in a given UNCP has to be optimum, as on increasing the concentration beyond that, there will be a decrease in the quantum efficiency. This decrease in quantum efficiency is observed because the excitation energy of the interior ions migrates through the CR process and eventually decays non-radiatively at the inner or surface defects. Typically, the concentration of Er^{3+} and Tm^{3+} ions are kept less than 3 mol% and 0.5 mol%

respectively whereas for the sensitizer (usually Yb^{3+}), it is doped in a high concentration (18-20 mol%) [13,48].

As mentioned above, the non-radiative transition between the energy levels plays an important role in determining the population density at the intermediate and emitting levels and consequently, the quantum yield of UCNPs. It can be seen from the multi-phonon, non-radiative relaxation rate constant k_{nr}, given in Eq. 2.2, that the non-radiative rate not only depends on the choice of the host lattice but also on the energy gap between levels [115].

$$k_{nr} \propto exp\left(-\beta \frac{\Delta E}{\hbar\omega_{max}}\right) \tag{2.2}$$

where β is empirical constant of the host, ΔE is the energy difference between populated level and next lower energy level and $\hbar\omega_{max}$ is the highest energy vibrational mode of the host lattice. Therefore, for the given host lattice, the activator ions having larger energy difference are less likely to undergo a non-radiative transition. Moreover, non-radiative decay plays an important role in the surface quenching effect where the energy from the inner ions propagates to the surface ions and get lost non-radiatively [116]. The incomplete coordination environments, the weak crystal field and exposure to high oscillators arising from the surface impurities, ligands or solvent make the surface ions act an energy sink [117]. Due to the surface quenching effect, the upconversion efficiency of nanoparticles (having large surface-volume ratio), is less than seen in their bulk counterpart.

The Jablonski diagram illustrating important radiative and non-radiative energy transition responsible for upconversion of Tm^{3+} and Er^{3+} ions when they are co-doped with Yb^{3+} is shown in Fig. 2.15(a). Here Yb^{3+} is acting as sensitizer, has only one excited $4f$ level of $^2F_{5/2}$ and it transfers the energy to the nearest Tm^{3+} or Er^{3+} ions through SET. In the visible band, Tm^{3+} shows three prominent peaks corresponding to three transitions, whereas Er^{3+} shows four peaks, as shown in Fig. 2.15(b) and Fig. 2.15(c) respectively.

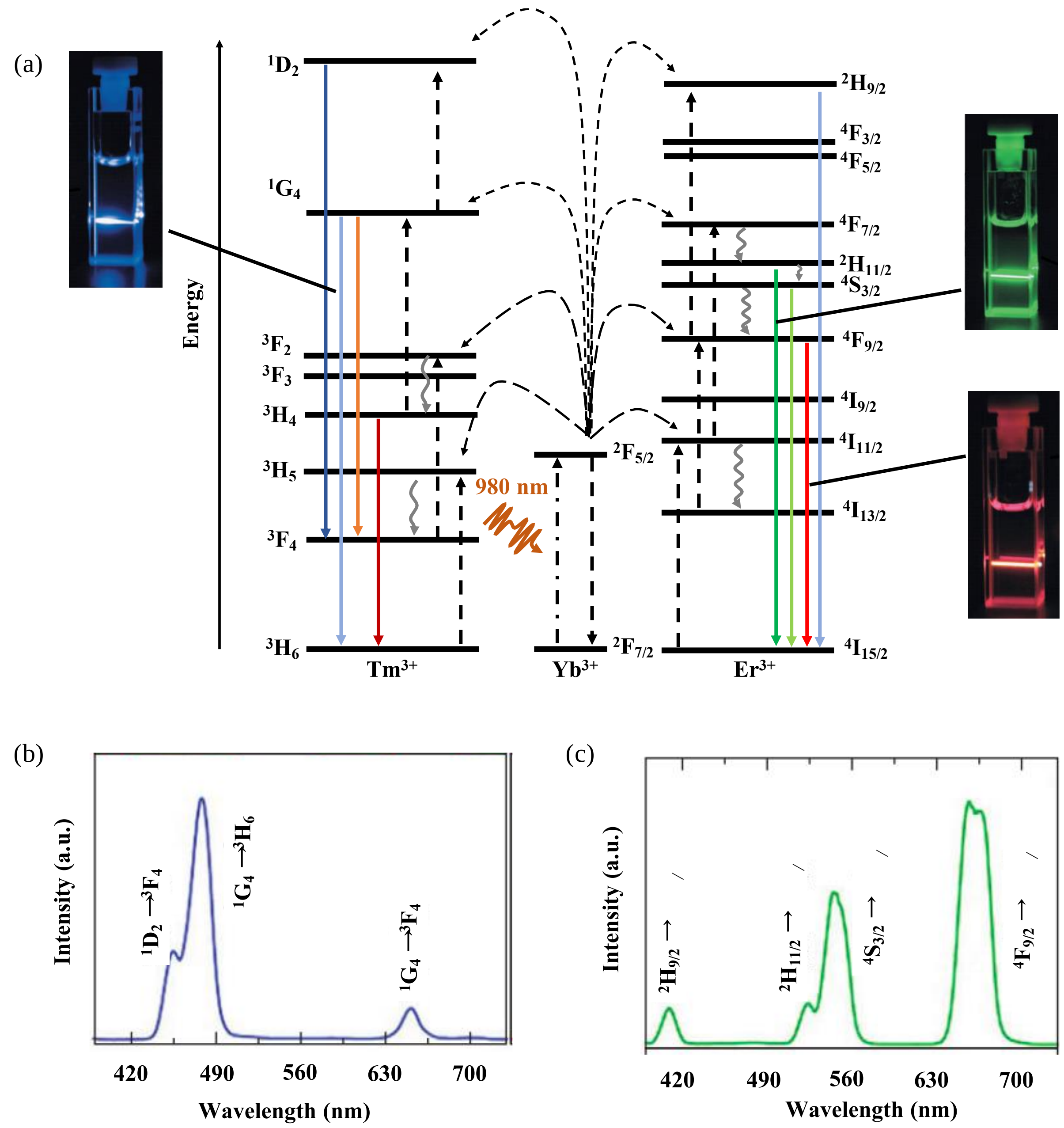

Figure 2. 15: (a) Partial energy levels diagram showing upconversion phenomenon of Tm^{3+} and Er^{3+} ions when Yb^{3+} act as a sensitizer. The dash-dotted, dashed, wavy and solid line represent the NIR photon excitation, energy transfer, multi-phonon relaxation and emission processes respectively [48]. *(b) A typical upconversion spectrum of Tm^{3+} in visible region (c) Typical upconversion spectrum of Er^{3+} in visible region. (b) and (c) are taken from* [118].

Table 2.3 shows major emission wavelength and corresponding energy level transitions of few activator ions. Among them, Ho^{3+}, Tm^{3+} and Er^{3+} are widely used as activator and interestingly for all these three activators, Yb^{3+} acts well as sensitizer [119]. Even though, these three ions have multiple emission peaks (ref. Table 2.3), it is possible to supress all the peaks except one. In 2011, Wang *et al.* reported that doping Ho^{3+}, Tm^{3+} and Er^{3+} in $KMnF_3$ crystal results in single band upconversion. They observed the lowest energy peak in all three cases i.e. peak centred around at 650 nm in Ho^{3+} and Er^{3+} and 800 nm for Tm^{3+}. The reason for suppression of the higher energy peaks is efficient non-radiative energy transfer from the higher levels to Mn^{2+} and then back to the activator at a lower level [120] . One year later, Tian *et al.* showed the same effect in $NaYF_4$: Yb^{3+}, Er^{3+} (18/2 mol %) by replacing the concentration of Y^{3+} used with 30 mol% Mn^{2+} ions [121]. This single band upconversion was independent of the external temperature, the excitation laser power and the amount of the dopant Yb^{3+} (0-28 mol%).

Table 2. 3: The major emission wavelengths and corresponding energy transition level of some of typical activator ions [122].

Activators	**Major Emission wavelength (nm)**	**Corresponding Energy transitions**	**References**
Pr^{3+}	489, 526, 548, 618, 652, 670, 732, 860	$^3P_0\rightarrow{}^3H_4$, $^1I_6\rightarrow{}^3H_4$, $^3P_0\rightarrow{}^3H_6$, $^3P_0\rightarrow{}^3F_2$, $^3P_1\rightarrow{}^3F_3$, $^3P_0\rightarrow{}^3F_4$, $^1I_6\rightarrow{}^1G_4$	[123–127]
Sm^{3+}	555, 590	$^4G_{5/2}\rightarrow{}^6H_{5/2}$, $^5G_{5/2}\rightarrow{}^6H_{7/2}$	[128,129]
Eu^{3+}	590, 615, 690	$^5D_0\rightarrow{}^7F_1$, $^5D_0\rightarrow{}^7F_2$, $^5D_0\rightarrow{}^7F_4$	[128,129]
Tb^{3+}	490, 540, 580, 615	$^5D_4\rightarrow{}^7F_6$, $^5D_4\rightarrow{}^7F_5$, $^5D_4\rightarrow{}^7F_4$, $^5D_4\rightarrow{}^7F_3$	[128,129]
Dy^{3+}	570	$^4F_{9/2}\rightarrow{}^6H_{13/2}$	[128,129]
Ho^{3+}	542, 645, 658	$^5S_2\rightarrow{}^5I_8$, $^5F_5\rightarrow{}^5I_8$	[130–132]
Er^{3+}	411, 523, 542, 656	$^2H_{9/2}\rightarrow{}^4I_{15/2}$, $^2H_{11/2}\rightarrow{}^4I_{15/2}$, $^4S_{3/2}\rightarrow{}^4I_{15/2}$, $^4F_{9/2}\rightarrow{}^4I_{15/2}$	[91,130,133,134]
Tm^{3+}	294, 345, 368, 450, 475, 650, 700, 800	$^1I_6\rightarrow{}^3H_6$, $^1I_6\rightarrow{}^3F_4$, $^1D_2\rightarrow{}^3H_6$, $^1D_2\rightarrow{}^3F_4$, $^1G_4\rightarrow{}^3H_6$, $^1G_4\rightarrow{}^3F_4$, $^3F_3\rightarrow{}^3H_6$, $^3H_4\rightarrow{}^3H_6$	[135,136]

2.3.4 Improvement of upconversion efficiency

The one of key drawback of UCNPs is its low upconversion efficiency (maximum reported to date is still 5% for irradiation below 100 W/cm^2) [137,138]. In the literature, several methods have been proposed to increase the upconversion efficiency such as the core-shell method [13], super high-power or broad-band excitation [139,140] , plasmonic enhancement [140], manipulating the local crystal field around activator ions by locally distorting the crystal lattice [120,141], energy clustering at the sub-lattice and the use of synthetic infrared dyes to amplify the sensitization process [142–144]. Among the these, the following three techniques are elaborated details in due to their frequent use in the literature their underlying novelty.

A. Core-shell technique

One way to prevent losses by surface quenching effect is to passivate the surface of UCNPs by a growing few nanometers of epitaxial shell layer, as shown by the schematic in Fig 2.16(a). This technique was first reported by Yi and Chow in 2007, where they grew a 1.5 nm inert shell of $NaYF_4$ on 7.7 nm hexagonal phased $NaYF_4$: Yb, Er (or YB, Tm) core. After passivation, the upconversion was enhanced by a factor of 7.4 and 29.6 for Er^{3+} and Tm^{3+} respectively [145]. They further coated core-shell structures with 25% octylamine and 40% isopropylamine modified poly(acrylic acid) (PAA) to make it water soluble. After the success of this homogenous shell growth, researchers have not only demonstrated an upconversion efficiency improvement with the heterogenous shell i.e. a shell having a different chemical composition than the core but also a doped shell with other rare-earth ions to achieve several unique properties. For example, Liang *et al.* reported 1.7 times enhancement of upconversion on coating a single layer of $NaGdF_4$ on $NaYF_4$: Yb, Er, as shown in Fig. 2.16(b) [146]. Similarly, Li *et al.*, coated 16 monolayers (~ 8 nm) over the core through one pot successive layer-by-layer synthesis [147]. Capobianco and co-worker showed that doping $NaGdF_4$ shell with Yb^{3+} further increases the NIR absorption and thus the overall upconversion efficiency in comparison to the inert shell [148]. A few research groups have coated silica shell on core or core-shell UCNPs in to make them water soluble/stable and thus enabling them suitable for biofunctionalization [13,146,149].

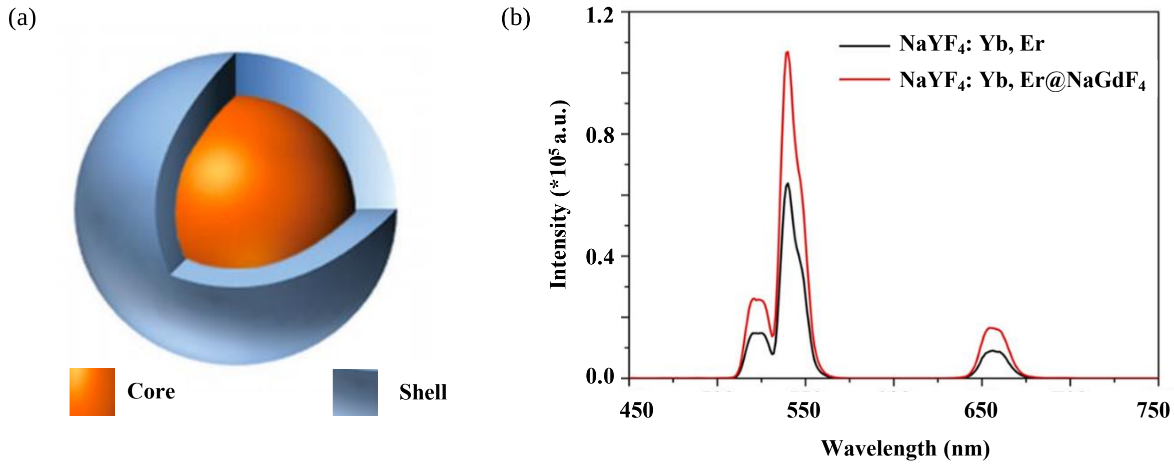

Figure 2. 16: (a) Schematic showing single inert epitaxial layer grown over core (b) The 1.7 fold enhancement in upconversion after coating the 29 nm core (NaYF4: Yb, Er) with 2 nm NaGdF4 layer [146].

B. Plasmonic enhancement

Plasmonic resonance involves large collective oscillation of free electrons in response to the external electromagnetic (EM) waves when the frequency of the incident EM waves matches the plasma frequency of the used plasmonic structure. At plasmon resonance, the incident EM field gets locally concentrated, and this concentration of electric and magnetic fields can be used to enhance absorption and the emitter's radiative decay rate. However, the same process also enhances the non-radiative decay rate and if structures are not properly designed, instead of enhancement, quenching is observed. Therefore, for enhancement, the spectral overlap between the plasmon resonance and absorption and/or emission frequencies of the UCNPs, polarization, field overlap (relative distance between plasmonic structures and UCNPs), plasmonic structure materials and incident pump power have to be carefully considered [150]. For example, Lu *et al.* reported a 38.8× enhancement with an incident power density of 2 kW/cm^2, but the enhancement reduced to 4.4×, on increasing the pump power above 40 kW/cm^2 [151]. Similarly, a 5 nm increase or decrease of the distance between UCNPs and metallic nanospheres film from its optimum distance of 10 nm, reduces the enhancement from 45× to 5× [152].

Plasmonic structures made of noble metals such as gold and silver are mostly used for upconversion enhancement [150]. Amongst these, even though silver has low losses at plasmonic resonance, in several cases gold showed better enhancement. For example, Deng *et al.* showed that with silver nanoparticles the enhancement in green and red emission were ~

4.4 and ~ 3.5 respectively whereas with a Au nanoshell the observed enhancement was ~ 9.1 (for green) and 6.7 (for red) [153]. These results show that several other factors including spectral overlap or field overlap play prominent effect in the upconversion enhancement.

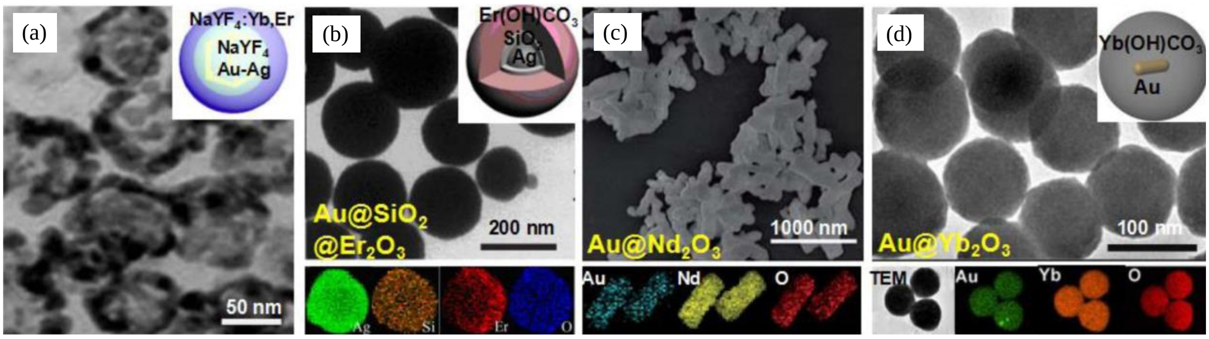

Figure 2. 17: Upconverter encapsulated metals [154].

In the literature, several variations of localized plasmonic structures such as rods, core-shell [155], core-spacer-shell [153,156], prism [157], spheres [158] as well as extended structures including waveguides [159], arrays of holes [160] or pillars [161] have been reported. Among the reported localized structures, two prominent variations are where the metal is core and the UCNPs are deposited on top of it (upconverter encapsulated) or the UCNP is a core and metal is deposited on the top (metal encapsulated). Some of the reported upconverter encapsulated structures are seen in Fig. 2.17.

C. *Energy clustering at subatomic level*

As discussed previously, an increase in the doping concentration of the sensitizer or activator leads to quenching of the upconversion which can be attributed to migration of the excitation energy to the lattice or surface defects. This propagation of energy is more likely in the case of highly symmetric structures such as cubic phased $NaYF_4$ and CaF_2, where energy can travel isotopically in all three directions, as shown in the schematic in Fig. 2.18(a; type 1). In contrast to that, for structures like $NaEuTiO_4$, the propagation of energy between Eu^{3+}-Eu^{3+} ions is more restricted in a plane due to the relative distance between the planes, as shown in Fig. 2.18 (a; type 2). This transfer of energy can further be restricted to 1D chain crystal lattices (shown in Fig. 2.18 a; type 3) and it is often observed between Eu^{3+}-Eu^{3+} in $EuMgB_5O_{10}$. Based on these findings, Liu and his co-workers realized that the migration of energy depends essentially on position of dopants than their doping concentration and went on localizing the energy exchange within arrays of discrete Yb^{3+} tetrad clusters as shown in Fig. 2.18(a; type 4) [162]. Thus, minimizing the long-distance energy migration losses, they demonstrated for the first time four-photon upconversion (violet emission) from Er^{3+} ions by synthesizing orthorhombic $KYb_2F_7:Er^{3+}$ (2 mol%; 98 mol% sensitizer ions) nanoparticles. The TEM image of nanoparticles as shown in Fig. 2.18(b). The simplified partial energy showing underlying energy transfer mechanism for four-photon upconversion is given in Fig. 2.18(c).

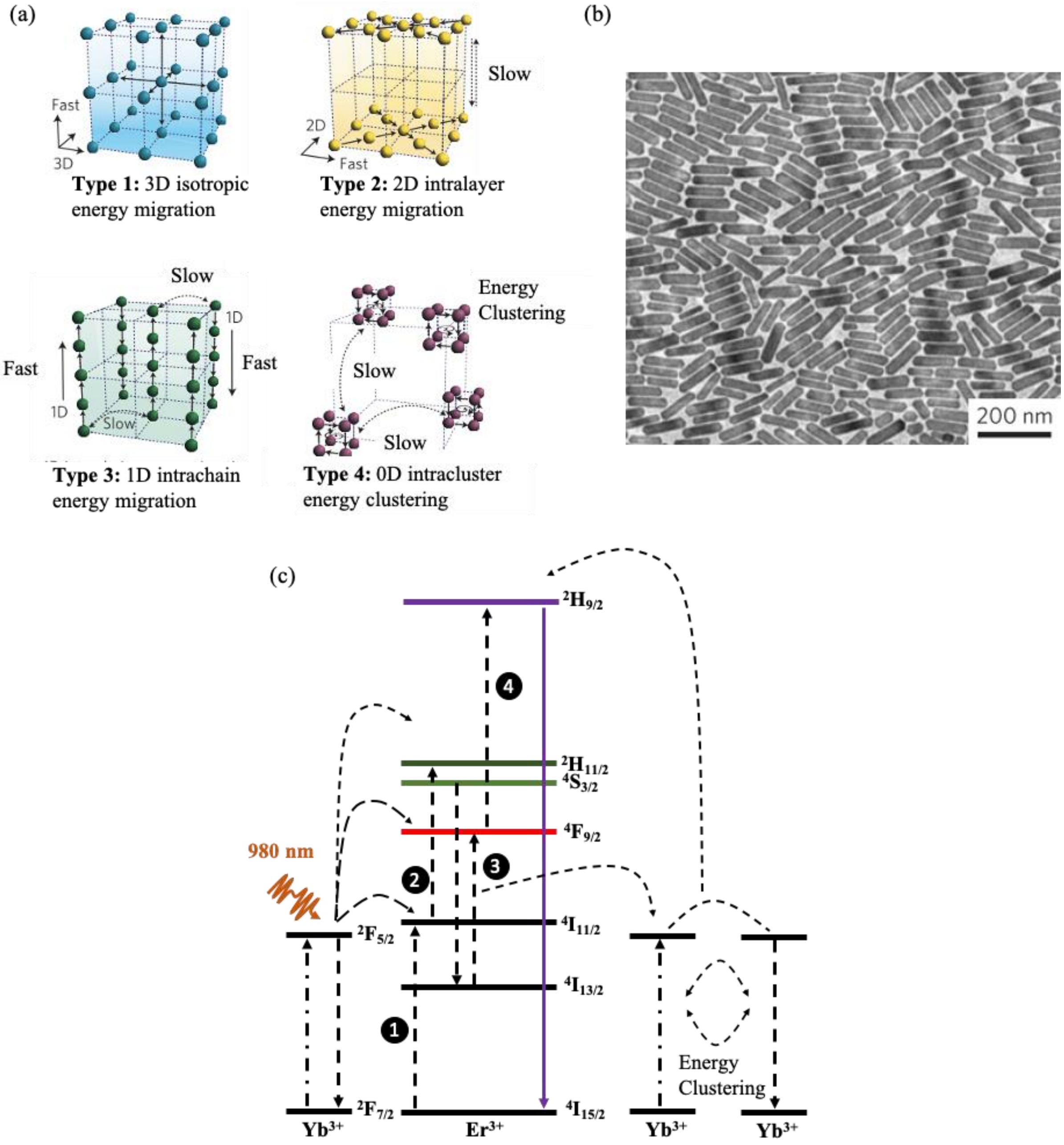

Figure 2. 18: (a) Schematic representation of energy migration in case of various sublattices (b) TEM micrograph of $KYb_2F_7:Er^{3+}$ (2 mol%) (c) Simplified partial energy showing underlying energy transfer mechanism for four-photon upconversion. Taken from [162].

2.3.5 Applications of upconverting nanoparticles

A. Biological Imaging

The usage of UCNPs for biological imaging over other down-converting conventional fluorophores such as organic dyes and QDs offers advantages in term of narrow and well-separated (from excitation) emissions, immunity towards photo-bleaching and photo-blinking (often reported in organic dyes) and low cytotoxicity (unlike QDs) [163]. Furthermore, the NIR radiation in comparison to UV has better penetration in human tissues, high signal to noise ratio (due to lack of background autofluorescence) and less photo-damage.

In the literature, authors have reported the usage of UCNPs for several imaging applications such as in in-vitro cell and tissue imaging, in vivo organism and animal imaging, fluorescence diffuse optical tomography and multimodal imaging [163–167]. Often, UNCPs are made selective to a certain target by a coating antibody. For example, Wang *et al.* linked rabbit anti-CEA8 antibody to silica-coated amino-modified UCNPs to make it selective to HeLa cells [168]. On incubating antibody modified UCNPs with HeLa cells in physiological conditions for 1 hour, the carcinoembryonic antigens (CEA) present on HeLa cell membrane react with the attached antibody, thus resulting in labelling of HeLa cells with UCNPs, as shown in Fig. 2.19(a). The bright and fluorescent images shown in Fig. 2.19 (b-d), prove high selectivity with this kind of immunolabeling. Similarly, Jiang *et al.* used anti-Her2 antibody and folic acid conjugated $NaYF_4$: Yb, Er UCNPs for labelling and fluorescent imaging of SK-BR-3 cells and HT-29 cells, respectively [169].

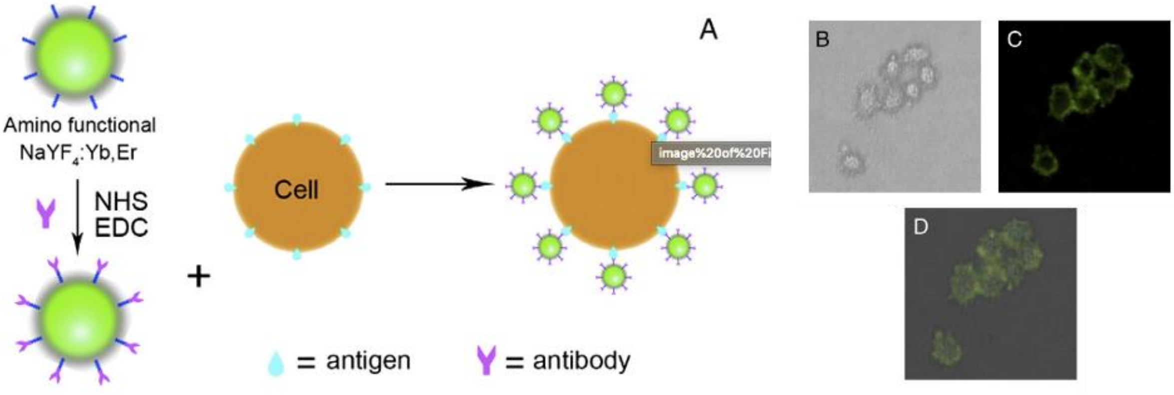

Figure 2. 19: (a) Schematic showing immunolabeling of HeLa cell. HeLa cell after incubated with rabbit anti-CEA8 Ab-conjugated UCNPs (b) bright field (c) dark field and (d) superimposed image. Taken from [168].

B. Cancer therapy

The nanoparticle-based Cancer therapies proposed have advantages over traditional cancer therapies like chemotherapy and radiotherapy in terms of better selectivity and localized treatment. Through nanoparticles, the cell apoptosis (death) is caused by two popular two popular methods i.e. by localized thermal ablation (known as Photo-thermal therapy (PTT)) and/or by creating oxygen/water deficiency inside cells with the help of a photosensitizer (known as Photo-dynamic therapy (PDT)). The photosensitizer is a special chemical compound which generates radical oxygen at a particular optical wavelength. The generated radical oxygens react with available oxygen or water present inside the cell thus causing their deficiency. In PDT, normally nanoparticles act as a carrier.

The common steps involved in PDT or PTT are shown through schematics in Fig. 2.20. In short, the nanoparticles are injected in blood and having size in nanometres, they travel unhindered across the body with the help of blood circulation. After 24-72 hours (depending on the nanoparticles involved) these nanoparticles get accumulated in tumor cells which is favoured by the enhanced permeation and retention (EPR) property of cancer cells. Due to EPR, the cancer cells (in order to multiply fast) extract more nutrients from the blood and retain them for longer time. Sometimes antibodies may be coated on nanoparticles to increase cell selectivity. Once nanoparticles are accumulated inside cells, cells apoptosis can be carried out by shining a suitable radiation on the cells. The unused nanoparticles are ejected out of body though urine and the same technique is also used for localized drug and gene delivery.

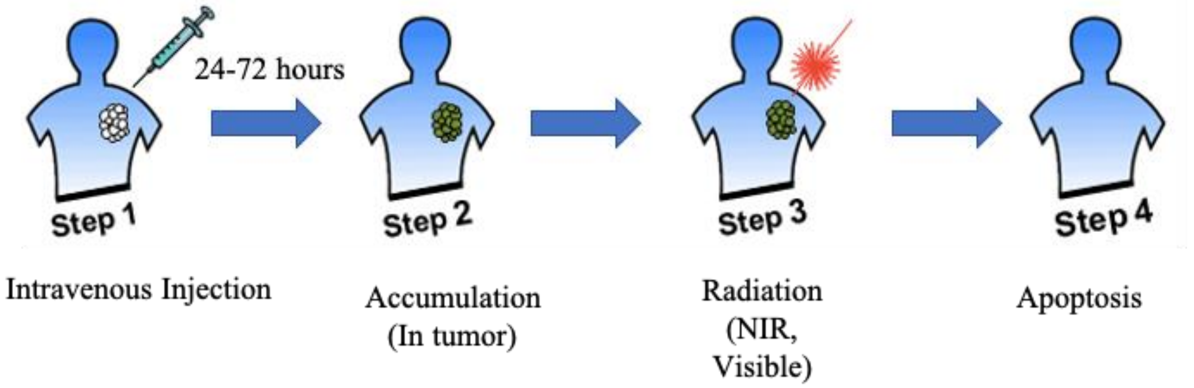

Figure 2. 20: Schematic showing steps involved in PTT and PDT.

In the literature, several groups have reported *in-vivo* and *in-vitro* usage of UCNPs for PDT, PTT and drug delivery [170–172]. However, since UCNPs cannot generate a heating effect unlike GNPs, they have to conjugate with some other NIR absorbing dye to perform PTT. For example, Chen *et al.* coated UCNPs ($NaGdF_4$:Yb:Er) with bovine serum albumin (BSA) for better stability in physiological environments and further conjugated them with Rose Bengal (RB) and IR825 dye for PDT and PTT respectively [173]. The RB absorbs the upconverted green light emitted from UNCPs to induce photodynamic cell killing, but, the absorbance of IR825 does not overlap with upconversion excitation and emission wavelengths, thus enabling nanoparticles to experience photothermal ablation under were 808-nm laser irradiation. The main challenge with this method still lies in treating a tumour buried deep inside the tissue.

C. Energy conversion

In the solar spectrum, the percentage of NIR light is ∼ 55 % in comparison to visible and UV radiation which are at ∼43% and ∼5%, respectively. Therefore, the ability of UCNPs to convert light in NIR spectral region to visible and UV radiation is a particular benefit for the field of energy conversion, especially for applications such as solar cells or the use of the TiO_2 based photocatalytic reaction [174–176]. Li *et al.* used $NaYF_4$:Yb^{3+}/Er^{3+}/Gd^{3+} nanorods with Au nanoparticles or shells and spin coated on hydrogenated amorphous silicon (a-Si:H) to obtain 16 to 72-fold enhancement in a short circuit current [177]. In this work, narrow-band 980 nm, 1100 mW laser light source was used for excitation. The performance of the UCNPs can be further increased, if their narrow-band excitation is engineered to allow broadband excitation. One of such schematics was proposed by Hummelen and his team, where they used the broad-band absorption of organic dyes to sensitize the upconversion process through Forster resonant transfer process, as shown in Fig. 2.21(a) [143]. As a proof of concept, the authors used a carboxylic acid-functionalized derivative of commercially available cyanine dye to excite β-phased $NaYF_4$: Yb, Er with light from 800 nm, 2 mW continuous wave laser and reported ∼ 3300 enhancement in the overall upconversion emission. The possibility of tailoring the absorption of organic dyes to the entire NIR range makes this method really a versatile and useful.

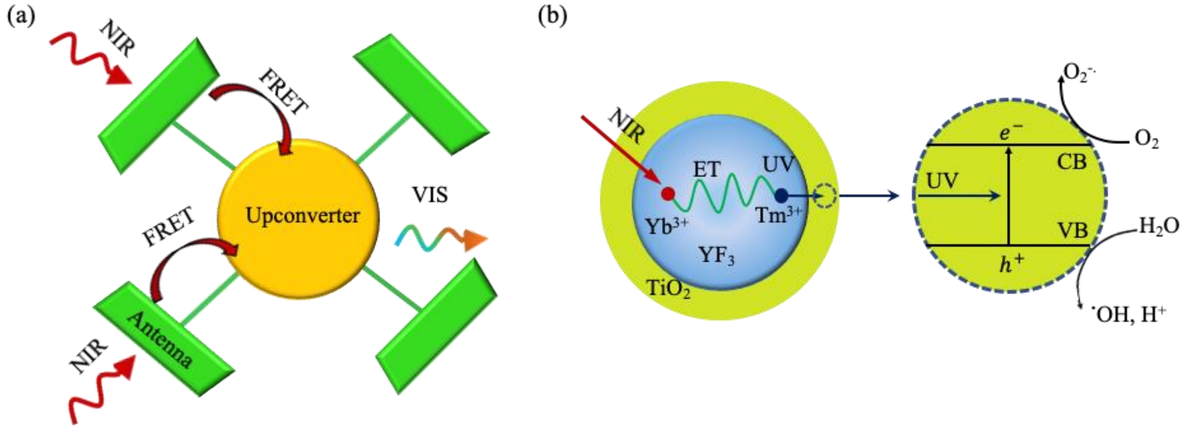

Figure 2. 21: Schematic showing: (a) organic dye (acting as antenna) sensitized upconversion process [143] *(b) photocatalytic reaction process using TiO_2-upconverting core-shell nanoparticles* [178].

In contrast to solar cells, the photocatalytic reactions using TiO_2 as a photocatalyst, needs UV light for initiation as the band gap of TiO_2 is around 3.2 eV [179]. Among the semiconductor based photocatalysts, TiO_2 is preferred because of several associated advantages such as stability, high photoactivity, low-cost, and being non-hazardous to humans and the environment [180]. As with only 5% of solar spectrum in the UV (on earth), using solar light as a photocatalyst is a highly non-efficient process. Therefore, in 2010, Qin *et al.* developed $YF_3:Yb^{3+}$, Tm^{3+}/ TiO_2 core/shell nanoparticles to utilize the NIR region of the solar spectrum where they upconverted the incident NIR to UV with the help of Tm^{3+} ions, as shown in the schematic in Fig. 2.21(b). Similarly, Obregon *et al.*, doped TiO_2 with Er^{3+} and showed an improvement in the photocatalytic efficiency for both the UV and NIR spectrum [181]. The reason for the increased efficiency in the UV was attributed to an enhanced electronic charge separation process in the presence of Er^{3+} ions and an increase in NIR absorption due to upconversion process. A review paper dedicated to upconversion based semiconductor photocatalysts has been recently published [179].

The reported work, showing ‘proof of concept’ research, highlights the rich potential of UCNPs in the field of energy conversion. However, actual devices designed specifically for ‘out-of-laboratory’ usage are still far away, as most of works reported used NIR laser or simulated sunlight irradiation. The use of actual sunlight irradiation and subsequent optimization of the device configuration needs to be performed before any commercial devices could realistically be made available on the market.

D. Securities

UCNPs are good candidates for security applications including barcodes, fingerprint detections, security printing with upconversion ink, and multiplexed encoding [112,182–185] for example. Illustrating Wang *et al.* coated $NaYF_4$:20%Yb, 2%Er with lysozyme binding aptamer to detect fingerprints on the problematic surfaces, i.e. those surfaces which show strong fluorescence on UV excitation like household marble, as shown in Fig. 2.22(a) [182] . It can be seen from the figure that the obtained fingerprint in case of using quantum dots is masked by the strong background fluorescence of the marble (top) whereas in the case of NIR excitation, the high signal to noise ratio and consequently a clear image (bottom). Similarly, Xu and his team produced upconverting nanoparticle-based inkjet ink to print high resolution and high throughput anti-counterfeit patterns [183] .One of such printed patterns is shown in Fig. 2.22(b).

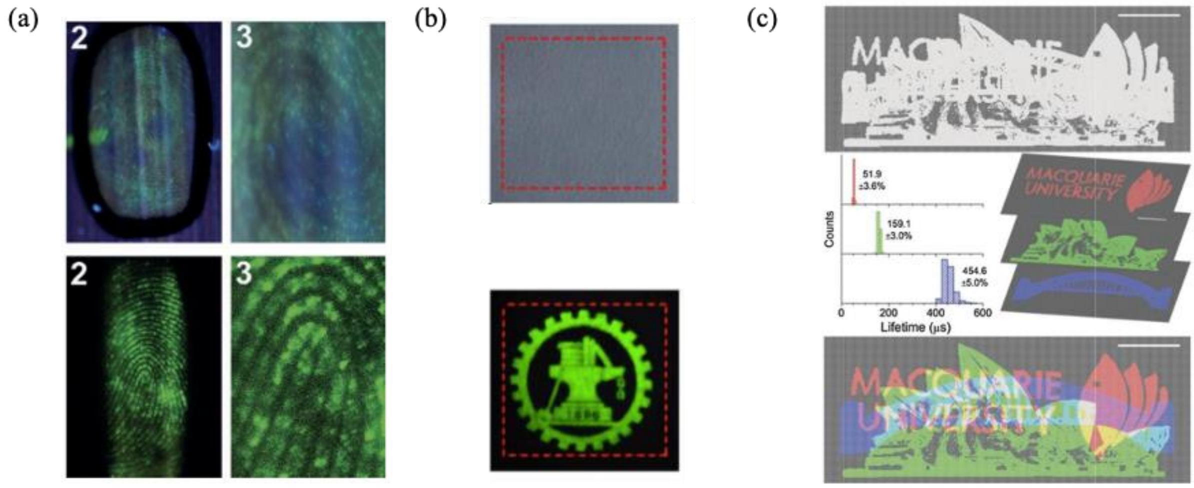

Figure 2. 22: (a) Actual sized and magnified fluorescence image in the case of quantum dots (top) and UCNPs (bottom) [182]. *(b) The printed paper with the upconversion ink in visible light (top) and in 980 nm light (bottom)* [183]. *(c) Overlapped images printed with three different* $\tau - dots$ *(top), having distinct lifetime of 52, 159 and 455 µs (middle) and pseudo colour is used to indicate the luminescence lifetime of each pixel (bottom)* [184].

The conventional fluorescence colour coding schemes suffer from drawbacks like spectral overlap and background interference, thus increasing the complexity of the setup needed. In 2014, Lu *et al.* demonstrated new luminescence lifetime decay (temporal) multiplexing by precisely tuning the decay lifetime of Tm^{3+} ions, co-doped with Yb^{3+} in $NaYF_4$ nanocrystals (called '$\tau - dots$') [184]. The authors varied the decay lifetime (in the blue bands) of $\tau - dots$ from 25.6 μs to 662.4 μs by changing the relative distance between the Tm^{3+} and Yb^{3+} ions, achieved simply by manipulating their doping concentrations. Figure 2.22(c) shows one of the applications of $\tau - dots$ in security, where three $\tau - dots$ with a distinct lifetime of 52, 159 and 455 μs was used to print three overlapping images. The top image shows the unresolved image with intensity-based luminescence technique which can be resolved with time-resolved scanning.

E. Optical storage

In 2010, Yan and his co-workers designed a rewritable optical storage approach with a non-destructive readout mechanism by depositing a monolayer of β $-$NaYF$_4$: Yb, Er using bottom-up assembly method and subsequently coating organic photochromic diarylethene derivatives on it [186]. The used organic dye shows photoisomerization on shining UV light ($\lambda = 325\ nm$) and thus reduced photoluminence (PL) around 540 nm (represents state “0”) and on shining visible light (around 550 nm) reverse photoisomerization happens PL was restored to its original value (represents state “1”). Therefore, authors used visible light and UV light for writing and erasing the data respectively. Since, the absorption of dye matches with Er^{3+} upconversion emission, the change in intensity of PL on NIR exposure can be used to read the stored data. The usage of NIR wavelength for readout reduces the chance of destructive readout because NIR photons do not have enough energy to trigger any molecular transition in the dye.

F. Sensors

UCNPs have been used to realise sensors in several fields to detect (but not be limited to) fields such as biomolecules, chemical ions, gases, pH, mechanical force and temperature [14,187–192]. Since, the luminescence of UNCPs is quite stable and is affected by the external environment, for sensing in most of the cases, they are used as nano-lamps, i.e. to photoexcite some other suitable chemical dyes or materials, whose absorption or emission is dependent on the substance being sensed. For example, to detect O$_2$, the UCNPs (NaYF$_4$: Yb, Tm) was incorporated with a cyclometalated iridium(III) coumarin complex [Ir(CS)$_2$ (acac)] in a thin layer of ethyl cellulose [193]. The absorption peak of [Ir(CS)$_2$ (acac)] at 468 nm overlaps with the 455 nm and 475 nm emission peaks of Tm^{3+} ions and its O$_2$ sensitive emission peak present at 568 nm is then used for detection. The same group (led Wolfbeis), demonstrated sensing of pH and consequently acidic gases like CO$_2$ and NH$_3$ using the same principle [187,188,194]. The change in spectrum of NaYF$_4$: Yb, Er due to the variation of CO$_2$ and NH$_3$ is given in Fig. 2.23. The dyes used for sensing CO$_2$ and NH$_3$ were bromothymol blue and phenol red respectively.

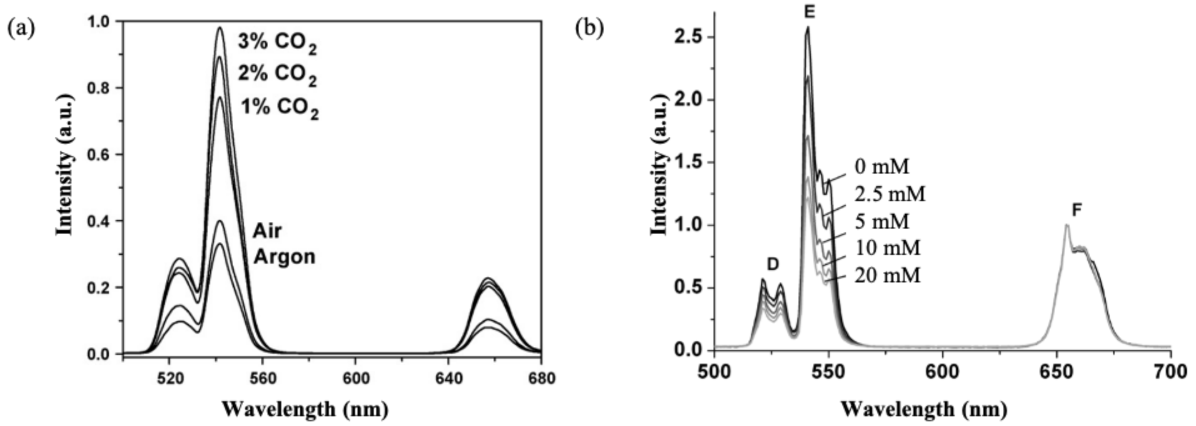

Figure 2. 23: The upconversion emission spectra of (a) CO_2 sensor [188] *(b)NH_3 sensor. The spectra are normalized to a peak at 655 nm* [187].

For temperature sensing, the ratiometric emission from the thermally coupled radiative energy levels (TCL), i.e. influenced by the population of these levels are related through Boltzmann's constant is normally used [15,195,196] . For TCL, the energy difference between the adjacent radiative level should be between 200 cm^{-1} and 2000 cm^{-1}, as for energy levels having an energy difference above 2000 cm^{-1} are not thermally coupled and for energy difference below 200 cm^{-1}, the radiations from these two levels are hard to differentiate [197]. Some of the TCLs used are Er^{3+}: $^4S_{3/2}/^2H_{11/2}$; Tm^{3+}: $^3F_{2,3}/^3H_4$; Nd^{3+}: $^4F_{7/2}/^4F_{3/2}$, $^4F_{7/2}/^4F_{5/2}$, $^4F_{5/2}/^4F_{3/2}$; Ho^{3+}: $^5G_6/^3K_8$ [197]. The presence of the natural inbuilt 'reference' reduces the influence of the external condition on the sensor performance. The UNCPs are used to measure the temperature inside biological cells as well as the lanthanide ions which are doped in glasses to developed temperature sensors [195,198]. The combination of UCNPS and polymers has not been explored in the literature for temperature sensing application and a study of work in that field form the basis of the research of this thesis, which will be discussed in more details in the next chapter.

Table 2.4 summarises few important diverse applications of upconverting nanoparticles reported between 2010-2020.

Table 2. 4: Summary of few important applications of upconverting nanoparticles (used in diverse fields) reported between 2010-2020.

Applications	**UCNPs**	**Associated modifications**	**Excitation Wavelength**	**Comments**	**Reference**
Sensing					
CO_2	$NaYF_4$: Yb, Er	bromothymol blue (BTB)	980 nm	Green band emission of UNCPs overlaps with the absorption of BTB.	[188]
NH_3	$NaYF_4$: Yb, Er	phenol red	980 nm	The absorption of phenol red overlaps with green band emission of UNCPs.	[187]
O_2	$NaYF_4$: Yb,Tm	cyclometalated iridium (III) coumarin complex [Ir(CS$_2$ (acac)]	980 nm	UCNPs and iridium (II) complex is incorporated in a thin layer of ethyl cellulose.	[193]
Hg^{2+} ions	$NaYF_4$: Yb (20 mol%), Er (1.6 mol%), Tm (0.4 mol%)	ruthenium complex (N719)	980 nm	Emission of Er^{3+} around (541 nm) overlaps with absorption of N719 which is sensitive to Hg^{2+} ions. Emission from Tm^{3+} (around 801 nm) is used for reference.	[192]

Temperature	$NaYF_4$: Yb, Er	Embedded in PDMS	980 nm	Linear response is observed between 295 K – 495 K.	[199]
Nano to Micro-newton forces	$\alpha, \beta - NaYF_4$: 18% Yb, 2% Er	Mn^{2+}	UC excitation = 980 nm PL excitation= 488 nm	The crystal field changed by applying mechanical force. The reported force is per particle.	[200]
Cancer Therapy					
Drug delivery	$NaYF_4$: Yb,Tm @ $NaYF_4$ core-shell + mesoporous silica cell	antitumor drug doxorubicin (Dox)	980 nm	Dox could be selectively released through the photocleavage of the o - nitrobenzyl (NB) caged linker by the converted UV emission from UCNPs.	[170]
Energy Harvesting					
Photocatalytic activity	$\beta - NaYF_4$: Yb, Tm	TiO_2	980 nm	The emission of Tm^{3+} ions matches with absorption of TiO_2 (in UV).	[175,176,178]

Solar Cells	Yb^{3+} -doped ZrO_2 (28 mol%)	-	980 nm	Energy transfer to host lattice through multiphonon relaxation cause thermal radiation.	[201]
	β- phased $NaYF_4$: Yb, Er	Derivative of cyanine dye, IR-780 (called as IR-806 in paper)	800 nm	Broad-band emission of IR-806 is absorbed by Er^{3+} ions.	[143]
Security					
Fluorescence life-time multiplexing	$NaYF_4$:Yb^{3+}, Tm^{3+}	Variation in relative distance between Tm^{3+} and Yb^{3+}	• Excitation time = 200 μs • Detection time = upto 3.8 ms	Lifetime changes is observed by changing relative distance between Yb^{3+} (sensitizer) and Tm^{3+} (activator) which was obtained by varying the doping concentration.	[184]
Upconverting Inkjet printer Ink	• For green fluorescence $NaYF_4$:Yb^{3+}, Er^{3+} • For blue fluorescence:	• *Hydrophobic ink* : 90:10 to 70:30 v:v cyclohexane: glycerol trioleate • *Hydrophilic ink* : 85:15 to 65:35 v:v ethanol-water solution	980 nm	Minimum resolution: 200 μm Printing speed: 12 pages per minute	[183]

	$NaYF_4:Yb^{3+}$, Tm^{3+}	(1:9 v:v ethanol:water):glycerol + Sodium Dodecyl Sulfonate to control surface tension			
Fingerprint detection	$NaYF_4$: 20% Yb^{3+}, 2% Er^{3+}	lysozyme binding aptamer	980 nm	Using cocaine binding aptamer, cocaine detection is possible	[182]
Lasing					
Microlaser	$NaY_{0.99}Tm_{0.01}F_4$ $@NaY_{0.8}Gd_{0.2}F_4$	Coated on ~5 μm polystyrene beads	• Excitation: 1064 nm • Lasing: 800 nm	Based on whispering gallery mode.	[202]
Miscellaneous					
Optical storage	$\beta-NaYF_4$: Yb^{3+}, Er^{3+}	diarylethene derivatives	• Read: 980 nm • Write: visible band • Erase:325 nm	The used organic dye shows an absorption band centred around 550 nm (represents state "0") on shining visible light and, disappears (represents state "1") on exposing it to UV.	[186]

Super microscopy	$NaYF_4$:Yb^{3+}, Tm^{3+}	High concentration of Tm^{3+} ions (8 mol%)	• Excitation = 980 nm (Gaussian) • Depletion = 808 nm (doughnut shape)	Based on Stimulated Emission Depletion (STED) techniques. Resolution obtained = 28 nm	[203]
RGB Temporal colour tuning	$NaYF_4$ doped with Yb^{3+}, Nd^{3+}, Tm^{3+}, Ho^{3+} and Ce^{3+}	Core-shell Nanocrystal	• 808 CW (for Blue emission) • 980 short pulse (for Green emission) • 980 nm long pulse (for Red emission)	Nd^{3+} and Yb^{3+} was used as sensitizer for 808 nm and 980 nm excitation respectively. Ce^{3+} was co-doped with Ho^{3+} in the same shell layer to facilitate the red emission of Ho^{3+}.	[204]
Electrogenerated chemiluminescence (ECL)	$NaYF_4$: Yb (20 mol%), Er (2%)	Graphene. $Na_2S_2O_8$ was used as co-reactant.	-4 V to 0 V	An improvement of 4.96-fold in ECL was observed on using Graphene. NaYF4/Yb,Er was excited by the oxidation-reduction excitation pathway.	[205]

2.4 Gold nanoparticles

2.4.1 Introduction

Among the reported metallic nanoparticles, nanoparticles realised from gold are of great importance because of their inertness, biocompatibility, well understood synthesis methods and surface modification processes and the possibility of synthesizing them in various sizes and shapes such as rods, spheres, shells, cubes, cages, as shown in Fig. 2.24. Moreover, due to longer circulation in the blood, gold nanoparticles are widely used for biomedical purposes. Specifically, nano-shells and nano cages are preferred for drug delivery and the use of a nano stars are preferred where large surface areas are needed.

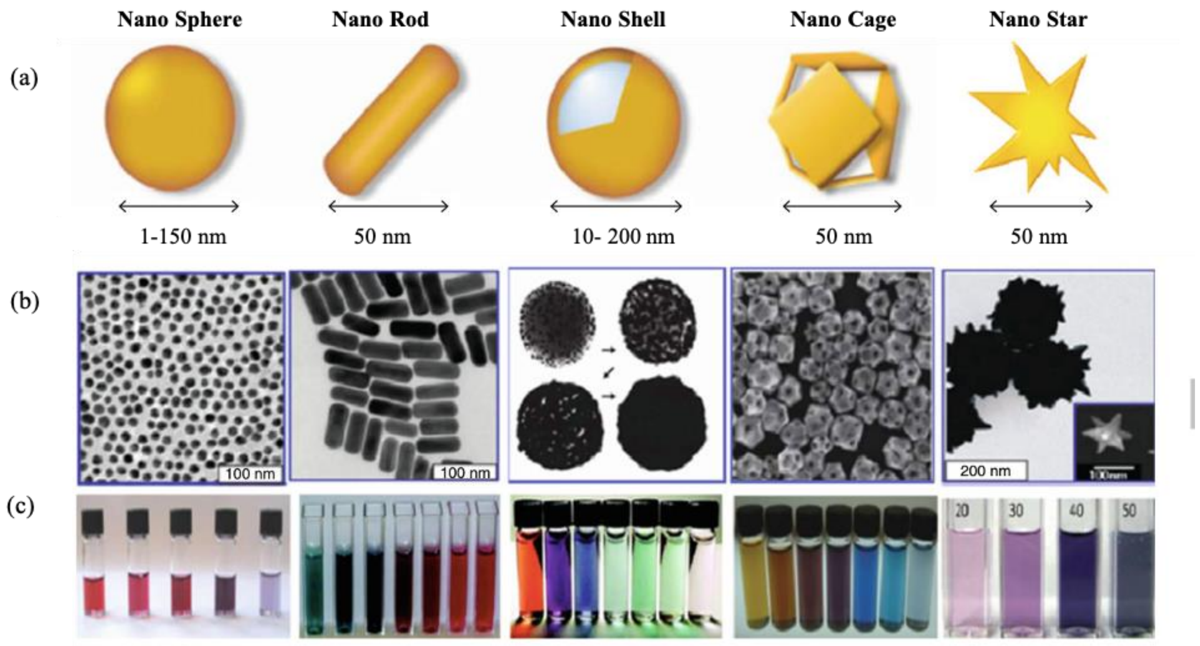

Figure 2. 24: Five different structures of nanoparticles realised using Gold (a) Schematic representations (b) TEM images (c) Colloidal solutions showing tuneable optical properties obtained by changing shapes of nanoparticles during synthesis [206].

Even though, the evidences show the usage of GNPs for centuries, even since the Roman Empire, it was in 1857 that Michael Faraday first synthesised of colloidal solution of GNPs in scientific ways and studied its optical properties [3]. Turkevitch, in 1951, reported a simple method of realising a stable colloidal solution of ~20 nm (average diameter) GNPs. These nanoparticles were reduced from their ionic state and stabilized with citrate ions [207]. This synthesis process, known as the Turkevitch method, is still one of the most widely used methods because of its simplicity. In 1994, Brust *et al*., introduced straightforward ways to obtain thiol-capped, highly stable GNPs [208]. Similarly, the simple and convenient approach of seeded growth synthesis of asymmetric GNRs was reported in 2001 [209], which then opened the door for a number of GNRs based applications.

Like other metallic nanoparticles, the majority of the applications are based on the LSPR effect observed in the visible wavelength region, as is discussed in the next subsection.

2.4.2 Localized surface plasmon resonance

The plasmonic resonance is defined as in-phase oscillation of free electrons of metals in response to the oscillating electric field component of incident EM wave, as shown schematically in Fig. 2.25(a). In case of symmetric structures like gold nanospheres or nano-cages, nano shells only a single resonant peak is observed as shown in Fig. 2.25(b). Mie in 1908, developed the theory explaining the LSPR effect in the spherical nanoparticles of arbitrary size [210]. However, now with the advancement of computers and computational software, mostly simulations are used to design and study the effect of LSPR, especially in the case complicated structures.

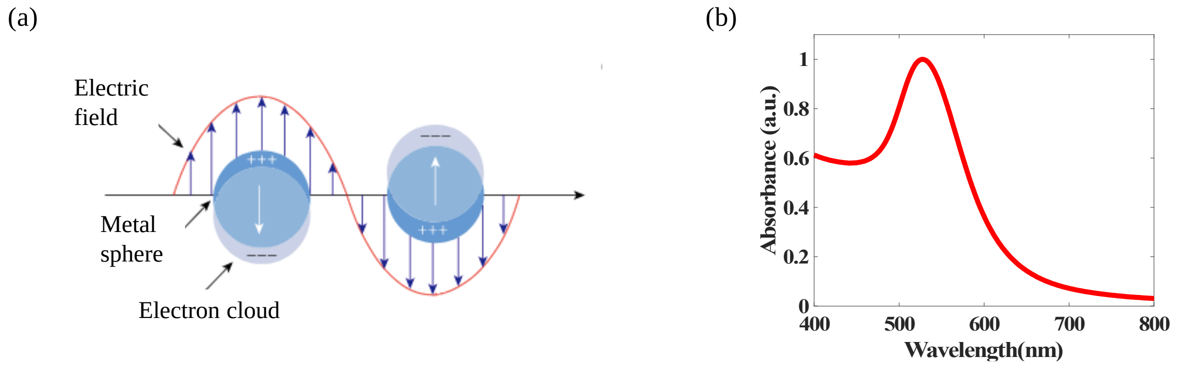

Figure 2. 25: (a) Schematic illustration of LSPR excitation for symmetric GNSs (b) Typical UV-Vis spectrum of GNSs showing single plasmonic resonance peak.

In case of asymmetric structures, such as GNRs, electrons can oscillate in two different directions. If the oscillation of the electrons is along the longer dimensions, it is known as Longitudinal LSPR (L-LSPR), whereas, if the oscillation of electrons is in the shorter dimension, it is known as Transverse LSPR (T-LSPR), as shown through the schematic in Fig. 2.26(a). These two different SPR resonances give raise to two distinct peaks in UV-Vis spectrum at shown in Fig. 2.26(b). The larger peak, corresponding to L-LSPR is highly sensitive to the external refractive index (surrounding the GNRs) and can be tuned from the visible to the NIR region by simply changing the aspect ratio of GNRs, (ref. Fig. 5.1(a)).

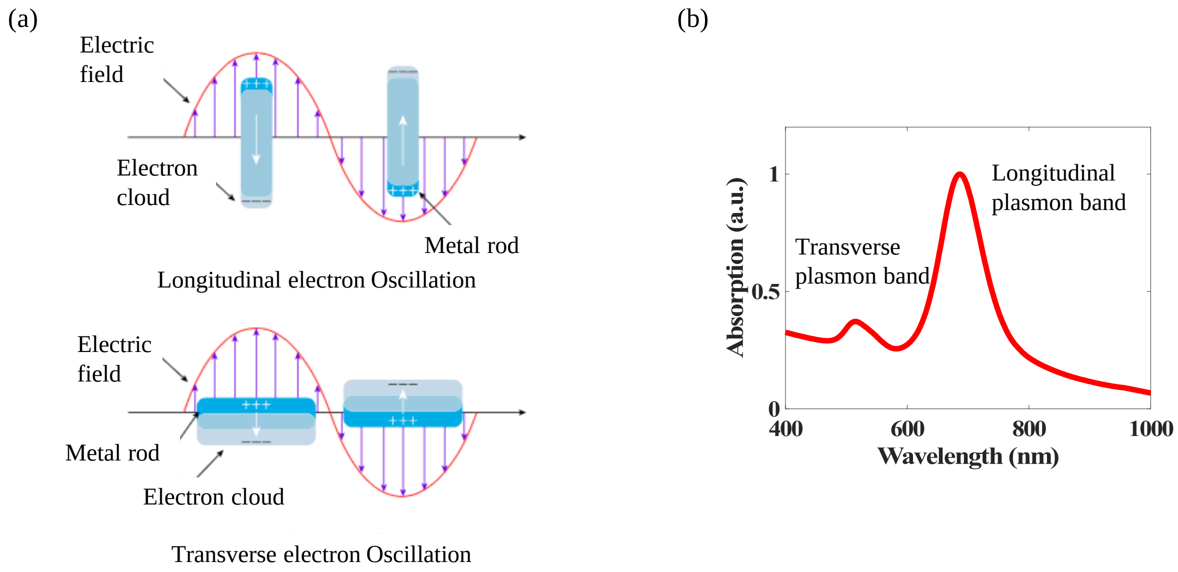

Figure 2. 26: (a) Schematic illustration of LSPR excitation for asymmetric GNRs (b) Typical UV-Vis spectrum of GNRs showing two resonance peaks.

The model describing the response of GNRs has been developed by Gans in 2005 [211]. This model will be dealt in more details in Chapter 5 of this thesis, where it is a pivotal in development of an algorithm to determine the distribution of aspect-ratio of GNRs in a colloidal solution.

2.5 Summary

In this chapter, a comprehensive review of the underpinning work on nanoparticles with the main focus on Upconverting and Gold nanoparticles has been presented. In the beginning, several important nanoparticles relevant from the point of view of sensing, emphasizing their synthesis and characterization techniques have been introduced. Thereafter, the underlying physics of upconverting nanoparticles and their applications have been discussed in detail. This Chapter ends with brief discussion of gold nanoparticles and the related LSPR effect.

The review shows that research into upconverting nanoparticles is still in a nascent stage. Even though, a number of promising applications have been demonstrated in the past two decades, although commercial products based on the work outlined are still far away, mostly due to low quantum efficiency and bulky characterization system. The latter problem has thus been tackled in the work of this thesis and addressed, to an important extent, by using a portable optical fibre-based characterization system, as shown through the current work and which will be explained in detail in the subsequent Chapters.

Chapter 3

Optical fibre thermometry using ratiometric green emission from an upconverting nanoparticles-polydimethylsiloxane composite

3.1 Introduction

The importance of temperature measurement to industry can be judged from the fact that approximately 75-80% of the sensors available on the market are temperature sensors [212]. Among the available range of temperature sensors, fluorescence-based temperature detection is distinctive over conventional electrically-based detection for a number of reasons, including intrinsic safety and immunity to stray electromagnetic radiation, for example [213,214]. Optical fibre-based temperature sensing devices using fluorescence from a well-chosen, appropriate material respond well to the demand for reliable and low-cost sensors needed for rugged environments, such as monitoring of transformers in a transmission grid and temperature monitoring in oil refineries, coal mines, electrical transport infrastructure and fire detection, where conventional measurement techniques may not be safe or subject to interference [15,195]. Optical fibre grating-based sensors can measure elevated temperatures, but often use expensive interrogation systems [215], whereas in comparison, fluorescence based detection can provide a lower-cost alternative solution due to relatively inexpensive excitation and detection techniques of the optical signals involved [216].

The most commonly used down-converting fluorescent materials, (i.e. those where $\lambda_{\text{excitation}} < \lambda_{\text{emission}}$) for temperature sensing are organic dyes and quantum dots [217,218]. However, organic dyes frequently suffer from a photo-bleaching effects, especially in the vapour phase and therefore cannot be used for extended periods [219]. Further, most quantum dot-based devices have problems with cytotoxicity and often use an excitation wavelength in the ultraviolet part of the spectrum, where prolonged exposure may cause photodecomposition of the samples [220]. These problems associated with down-converting materials can be overcome by using another class of fluorescent materials know as up-converting (UC) materials where, as the term “upconversion” suggests, the emission of the shorter wavelength results from absorption of two or more longer wavelength (and therefore less energetic) photons. By comparison with conventional nonlinear UC techniques such as simultaneous two-photon absorption and second-harmonic generation, UC is achieved by sequential absorption of two or more such photons. Rare-earth (RE) group elements (mainly Er^{3+}, Ho^{3+} and Tm^{3+}) are a natural choice for low pump-intensity UC because of their ladder-like metastable energy bands, naturally created in the $4f^n$ electronic configuration due to electronic repulsion and spin-orbit coupling [13,78,112]. This has been discussed in details in the previous chapter of this thesis. Furthermore, such RE^{3+} ions based on UC typically exhibit large anti-Stokes shifts [112], sharp emission lines [221] and temperature-dependent emissions, provided the two radiative energy levels have an energy difference of between 200 cm^{-1} and 2000 cm^{-1} [222–224]. The populations of these thermally coupled levels (TCL), related through the Boltzmann distribution, provide a natural ratiometric temperature detection approach, in that way reducing the influence of external conditions on the sensor performance and creating an inbuilt 'reference' channel [196,197,225,226].

As can be seen from the literature, Er^{3+} (or the combination of Er^{3+} and Yb^{3+}) has been widely used as a dopant in various types of glasses, such as tellurite [227–229], fluorotellurite [230], oxyfluoride [231,232], fluoroindate [233,234], chalcogenide [235] and fluorophosphate [236] glasses, serving as the basis of various fluorescence-based temperature sensors. A detailed review of various upconversion-based temperature sensor schemes has been produced by Zhao *et al.* in recently published review paper [237]. Since the doping of RE^{3+} ions in glass is generally performed in the molten phase, a high temperature environment for the synthesis is needed (with temperatures usually rising to more than 900 K). Furthermore, the experimental arrangements needed for the operation of several of the sensors reported are relatively complex (requiring lenses, collimators, a bulky spectrometer etc.) and thus are expensive and susceptible to environmental effects [227,230,232,235,236], making them less well suited to be used outside the laboratory. To avoid the problems that are experienced when a high temperature environment is used during synthesis, in this work an UCNPs-polydimethylsiloxane (PDMS) composite has been explored as the basis of the sensor system itself – one that is created at much lower temperatures (583 K) than glasses.

The characterization of these potential sensor materials (prior to their incorporation in the sensor probe itself) is done using where a sample of this UCNPs-PDMS composite was dip coated on a multimode, larger diameter, optical fibre (chosen to allow the maximum excitation light to be delivered to the sensor head and light collected from it), with an inexpensive portable

USB-based spectrometer being used to record fluorescence. The use of optical fibre also provides the advantage of high signal-to-noise ratio, potentially long distances being possible between the point where the sensing is occurring (particularly valuable in applications such as mining) and offering reliability of performance in corrosive & harsh environments [238]. Since, it was not possible to dope RE^{3+} ions directly into the PDMS, a hexagonal-phased UCNP ($NaYF_4$: (18%) Yb^{3+}; (2%) Er^{3+}) composite was used as the basis of the sensor material. This approach was preferred over the use of other UC nanoparticle materials because of their high UC efficiency [239]. Similarly, PDMS was chosen over other polymers because of its good chemical stability, resistance to water, low cost and good optical properties in the visible-near infra-red (NIR) region (such as high transparency and low autofluorescence [240]). Moreover, PDMS shows good adhesion to glass, which further simplifies the coating process onto optical fibres and thus increases the durability of the sensor created.

In this work, UCNPs have been chemically synthesized using a solvothermal method and its fluorescence emission has been explored and recorded, in three different media i.e. in a non-polar solvent (cyclohexane), in powder and in PDMS. Following that, the UC powder itself and the UCNPs-PDMS composite materials created have been coated onto multi-mode optical fibre, to form the basis of the temperature sensors designed, ready for evaluation. The optical fibre thermometer schemes thus developed has been characterized and a ‘figure of merit’ for the sensors obtained. This has been designed to make a cross-comparison of key parameters more easy: the figure of merit has been determined from the data captured on the temperature-related change in the ratios of the integrated emission intensities of the two green emission bands, from the Er^{3+} ions.

3.2 Experimental section

3.2.1 Chemicals and reagents

For the chemical synthesis of the UCNPs, the following chemicals were used: Yttrium(III) chloride hexahydrate ($YCl_3 \cdot 6H_2O$; 99.99%; Acros Organics), Ytterbium(III) chloride hexahydrate ($YbCl_3 \cdot 6H_2O$; 99.90%; Acros Organics), Erbium(III) chloride hexahydrate ($ErCl_3 \cdot 6H_2O$; 99.90%; Sigma Aldrich), Ammonium fluoride (NH_4F; ≥98.0%; Acros Organics), Sodium Hydroxide (NaOH, 97+%; Sigma Aldrich), Methanol (CH_3OH; Analytical Grade, Fisher Scientific), Ethanol (C_2H_5OH; HPLC grade; Fisher Scientific), Oleic acid ($C_{18}H_{34}O_2$; 90%; Sigma Aldrich), 1-Octadecene ($C_{18}H_{36}$; 90%; Sigma Aldrich), Cyclohexane (C_6H_{12}; >

95%; Acros Organics), and silver conductive paint (Electrolube). PDMS (SYLGARD 184) was purchased from Dowsil. All chemicals were used as received without any further purification.

3.2.2 Thermometer materials characterization – instrumentation used

The TEM imaging was done using a Model JEM-1010, operating at an accelerating voltage of 80kV. The hydrodynamic diameter of the UCNP was calculated using a Zetasizer Nano ZEN 3600 (Malvern Instruments). The attenuated total reflection Fourier-Transform InfraRed (ATR-FTIR) spectra were obtained using a Perkin Elmer Frontier Spectrometer.

3.2.3 Synthesis of UCNPs & UCNPs-PDMS composites

The hexagonal phase UCNPs used in this work were chemically synthesized using a solvothermal process, by slightly modifying the procedure described elsewhere [146]. In summary, 0.8 mmol of $YCl_3{\cdot}6H_2O$, 0.18 mmol of $YbCl_3{\cdot}6H_2O$ and 0.02 mmol of $ErCl_3{\cdot}6H_2O$, 15 ml of 1-octadecane (acting as solvent) and 6 ml of oleic acid (acting as surfactant) were added to a 50 ml three-necked round-bottom glass flask. As shown in Fig. (3.1), the first neck of three necked flask was used for pouring chemicals into the flask whereas second neck and third neck was connected to Schlenk line (for contolling Argon flow) and vacuum pump respectively. Heating was applied to the above mixture, taking it to a temperature of 433 K for 30 mins in an inert (argon) environment to dissolve the lanthanide salts while stirring at 350 rpm (throughout the synthesis process the solution was kept stirred at this speed). After cooling the solution to room temperature i.e. ~297 K, 2.5 mmol of NaOH and 3.9 mmol of NH_4F dissolved in 3 ml and 10 ml methanol solution respectively were added dropwise, using a 20 ml syringe. This is a crucial step because NaOH and NH_4F rapidly react to form a NaF precipitate which tends to stick to the walls of the beaker and the amount of NaF added to the solution determines the size and shape uniformity of the UCNPs thus created [241]. Therefore, to avoid the NaF sticking to the walls of the beaker, instead of mixing the NaOH and NH_4F methanol-based solutions in a beaker and then transferring the NaF precipitate to the syringe, these methanol-based solutions were mixed directly in the syringe itself for convenience. Afterwards, the resultant solution was kept stirred at 323 K for 30 minutes to complete the NaF nucleation process. In the next step, the methanol was completely removed from the solution by gradually heating it to 383 K (alternating between argon flow and vacuum pressure during the ramping process) and once the temperature reached 383 K, it was maintained there for 10 minutes under vacuum conditions. Thereafter, the solution was quickly ramped up to 583 K (at a rate of 10 K/min) and kept at that temperature for one hour under argon protection, before cooling down naturally. Once the solution was cooled down, it was transferred to a 50 ml centrifuge tube, mixed thoroughly with 5 ml of ethanol and the resultant solution was centrifuged at 3500g for 3 minutes. After discarding the supernatant, the white-colored precipitant was re-dispersed into cyclohexane and again precipitated by adding 8 ml of ethanol, following which centrifugation (3500g for 3 minutes) was carried out. The previous step was repeated once more by replacing 8 ml of ethanol by 4 ml of ethanol and 4 ml of methanol. Finally, the precipitant was re-dispersed in 4 ml of fresh cyclohexane to obtain a stable, transparent UCNPs colloidal solution (concentration: 0.05 mg/µl), as shown in the inset of Fig. (3.1).

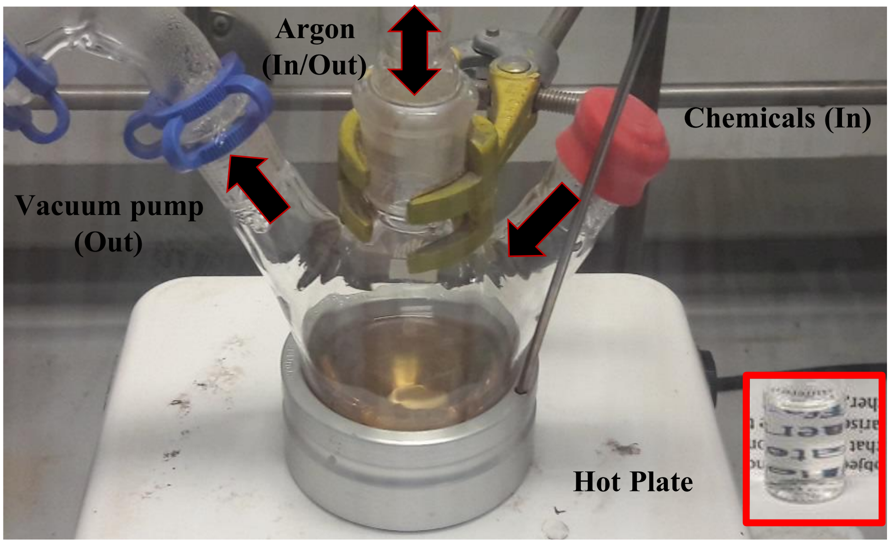

Figure 3. 1: Three necked glass flask used for synthesis of UCNPs. Inset shows photograph of UCNPs dispersed in cyclohexane (illustrating the clarity of the solution).

UCNPs-PDMS composite was obtained by using a technique involving modification of the steps used by Wang *et al.* [108]. As a first step, UCNPs' colloidal solution, PDMS base solution and the curing agent were placed (in a ratio 10:10:1 (by volume)) in a glass beaker and mixed thoroughly. The bubble trapped in the resultant solution, while mixing, was removed by degassing it in a vacuum chamber for half an hour. Afterwards, the solution was left overnight, at room temperate and pressure. The following morning, the partially cured solution was heated to 354 K (below the cyclohexane flash point) for an hour to ensure the complete removal of the cyclohexane, while at the same time completing the curing process.

3.2.4 Optical fibre thermometer design

A 5 cm long polymer clad silica multimode Optical Fibre (OF), having 1000 μm core diameter (FT1000UMT; Thorlabs) was used as the basis of the temperature probe itself. An OF with a 1000 μm core diameter was chosen because this larger diameter (than used for typical ‘communications-grade’ fibre) not only provides a much large surface area for coating, excitation and recollection of the UC fluorescence but also offers good mechanical strength to the probe. To increase the light coupling efficiency, both end facets were sequentially polished flat using 5 μm, 3 μm and 1 μm grit polishing sheet (LFG series, Thorlabs). Finally, 1 cm of polymer jacket was removed from one end of the fibre, which was glued to a SMA connector (11050A; Thorlabs) while from another end 1.5 cm of polymer jacket and 5 mm of cladding were removed. The bare facet was used for coating with the UC powder and UCNPs-PDMS composite to create the probes.

For the UC powder coating, first UCNPs were precipitated from a 500 μl of colloidal solution by adding 500 μl of ethanol followed by centrifugation (3500 g, 3 mins). After discarding the supernatant, the bare end of the OF was inserted into the precipitate to attach some UC powder to the fibre tip. Finally, the UC powder-coated OF was dried overnight and heated at 354 K for an hour (the following morning) to remove any residual traces of cyclohexane.

To coat the UCNPs-PDMS composite, the 3 mm of optical fibre was dipped in the UCNPs-PDMS composite solution, obtained by mixing UCNPs and PDMS and removing the trapped bubbles that were seen and which would deteriorate the optical quality of the probe material (as described above). It was then left for one minute and slowly taken out using a lab-jack. As in the case of the UC powder, the UCNPs-PDMS was left overnight at room temperature and pressure and the next morning heated to 354 K for an hour. Another 5 mm layer of PDMS was coated on the fibre, following the same procedure but with the exception of replacing the UCNPs-PDMS solution by PDMS. This PDMS coating passivates the Er^{3+} ions present on the surface of UCNPs-PDMS, thus nullifying the impact of the surrounding environment on the UC fluorescence. Since the OF probe was designed to operate in reflection-mode, silver paint was coated on the tip by dipping it into commercially-obtained silver paint, thus to enhance the reflection of UC fluorescence. The probe created in this way is shown in Fig. 3.2. In that figure, the inset shows the visible (green) UC fluorescence emitted by the UCNPs-PDMS-coated tip, upon excitation using light from a 500 mW, 980 nm wavelength (λ) laser source. Before evaluating the temperature sensing performance of the probe, it was annealed at 503 K for 3 hours to stabilize it.

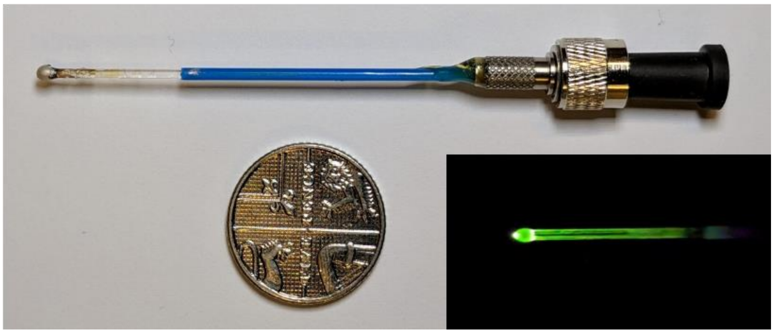

Figure 3. 2: Optical fibre temperature probe constructed after coating silver paint on the UCNP-PDMS tip. Inset shows green UC fluorescence emitted by UCNPs-PDMS composite coated tip (before the silver coating was applied) upon excitation with light from a 500 mW, 980 nm laser source.

3.2.5 Optical thermometer characterization setup

In all the experiments carried out to investigate the fluorescence-based performance of the sensor probe, light from a continuous-wave 980 nm diode laser (JDSU 2900 series) with a fibre pigtail and a maximum achievable power (of 500 mW) was used for excitation. The UC fluorescence emitted was acquired using a portable spectrometer (Maya-type 2000PRO; Ocean Optics). The UC spectrum of the colloidal solution was recorded using the setup created and shown in Fig. 3.3. As it can be seen in the figure, the laser source and the spectrometer were connected to 1 cm cuvette holder (CUV-ALL-UV; Ocean Optics), set at 90° to each other to minimize the amount of scattered source light reaching the spectrometer.

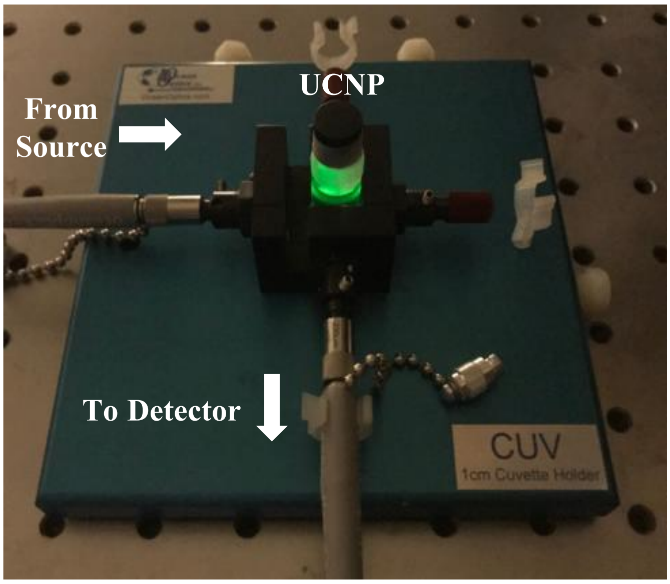

Figure 3. 3: Characterization setup for measuring fluorescence of UCNPs in colloidal solution. During measurement, external light was turned off.

The UC powder and the UCNPs-PDMS were coated onto the OF, following the steps described in the preceding subsection and characterized using the setup schematically shown in Fig. 3.4. As can be seen from the Fig. 3.4, the laser source and the spectrometer were connected to the two ends of 2x1 fibre bundle (ϕ = 230 µm; Ocean Optics), while the third was connected to the coated OF probe through an SMA connector (SMA905, L-com). A 2 mm thick NIR rejection filter (ϕ = 11.9 mm; BP550; MidOpt) was placed in the path of the spectrometer to avoid its saturation from the reflected source light. The actual photograph of the equipment, highlighting the portability of setup is shown in Fig 3.5. The NIR filter was mounted on a 1 cm cuvette holder (CUV-UV; Ocean Optics; shown in the exploded view of Fig 3.5) as it provides a natural alignment between the incoming and the outgoing fiber, thus making the setup both simple and readily portable when required. The UC spectrum was recorded over the wavelength range from 400 nm to 700 nm (at a resolution of 1 nm), with an integration time of 1 second, using the Spectra Suit software package (Ocean Optics).

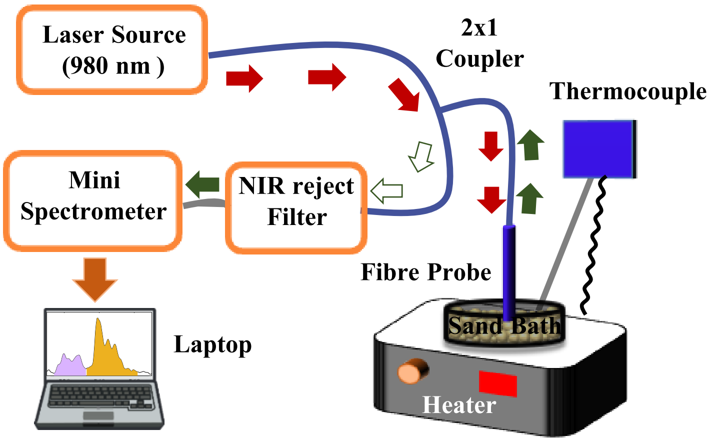

Figure 3. 4: Schematic of the setup used for thermal characterization of the probes.

In the experiments which were set up to investigate the temperature performance of the probe, a heater (RCT Basic; IKA) equipped with a thermocouple (ETS-DS; IKA; minimum resolution = 0.1 K) was used to regulate and control the temperate of a sand bath (SiO_2; 50-70 mesh particle size; Sigma Aldrich) or air bath, to provide a stable temperature zone for the calibration. The sand bath, due to its excellent thermal properties, was used to decrease the ramping-up time, minimize the temperature fluctuations and achieve a uniform temperature distribution, which facilitated the calibration of the probe. For each temperature, the mean value of six replicated readings, taken at intervals of 1 minute, was recorded.

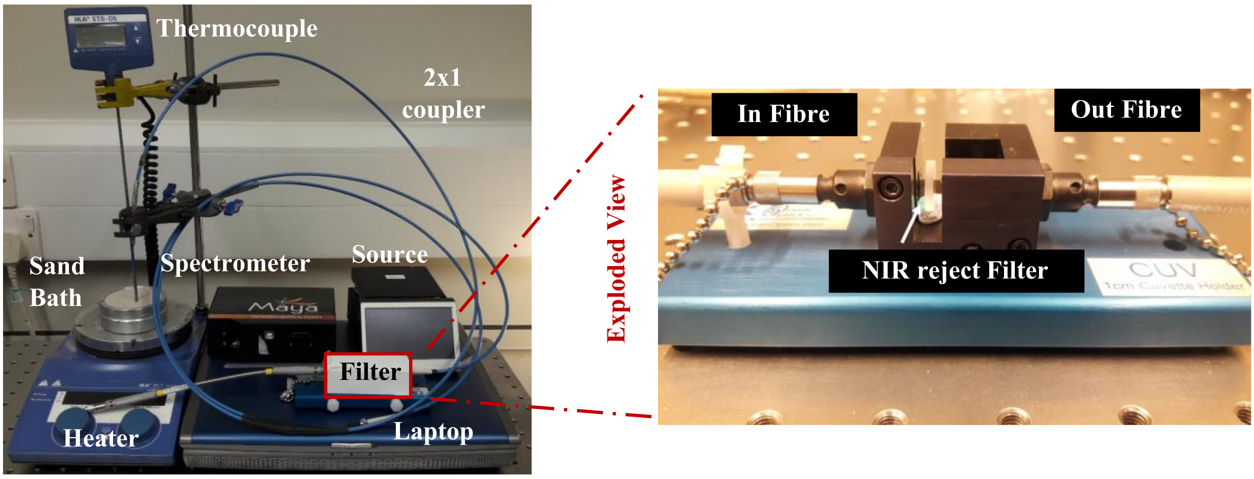

Figure 3. 5: Photograph of the equipment used in the thermal characterization of probes (left). The exploded view of the filter (right).

3.3 Results and discussion

3.3.1 Characterization of the thermometer materials

A TEM image of the synthesized UCNPs used is shown in the Fig. 3.6(a). It can be seen from the figure that the synthesized UCNPs are of uniform size and have a clear hexagonal shape, as desired. The mean hydrodynamic diameter of the UCNPs was found to be ~56 nm from the DLS measurement made. The inset of Fig. 3.6(a) shows the green visible UC fluorescence emitted by the synthesized colloidal solutions on excitation with light from a 500 mW, 980 nm diode laser. Figure 3.6(b) shows photographs of the PDMS (marked as 1) and the UCNPs-PDMS composite (marked as 2) and the UCNPs-PDMS when excited with light from a 980 nm diode laser (marked as 3). It can be seen from the same figure that the UCNPs-PDMS composite is less transparent than the pristine PDMS. This loss of transparency on adding the UCNPs to the PDMS results from the agglomeration of the UCNPs to form strong scattering centers, as observed and reported in the literature for other inorganic-organic nanocomposites [242,243]. The loss of transparency does not have significant impact on its usage as a temperature sensing material.

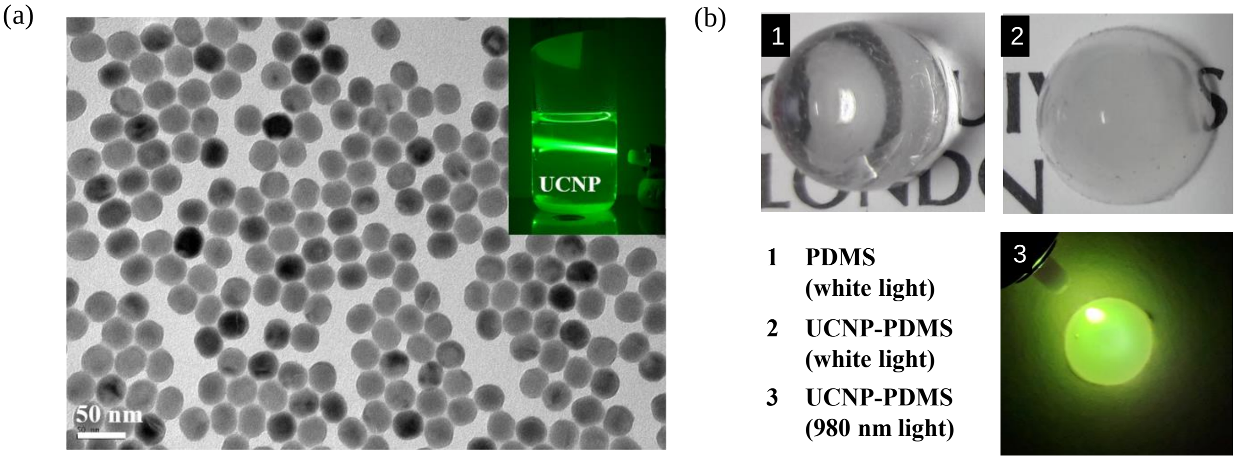

Figure 3. 6: (a) TEM image of synthesized hexagonal phased-UCNPs. Inset shows the green UC fluorescence from the UCNPs colloidal solution when excited using light from the 980 nm laser source. (b) Photographs of the PDMS (marked as 1) and the UCNPs-PDMS composite.

Figure 3.7(a) shows the UC emission spectra recorded using the spectrometer mentioned, for UCNPs in three different media: in cyclohexane, as powder and in PDMS. It can be seen that in all the three media the UC fluorescence shows three distinctive peaks (marked as 1, 2 and 3 on the figure) and these comprise two ‘green’ bands (λ_{peak} = 525 nm & 545 nm) and one ‘red’ band (λ_{peak} = 650 nm). The electronic transitions responsible for these peaks are shown in relation to the energy level diagram given in Fig. 3.7(b). As previously described in the literature [13,78,112], the energy level $^4I_{11/2}$ is populated through several routes but the energy transfer (ET) from Yb^{3+} ($^2F_{5/2}$ (Yb^{3+}) + $^4I_{15/2}$ (Er^{3+}) → $^2F_{7/2}$ (Yb^{3+}) + $^4I_{11/2}$ (Er^{3+})) and through ground state absorption (GSA; $^4I_{15/2}$ (Er^{3+}) + photon → $^4I_{11/2}$ (Er^{3+})) are dominant. Further, contrasting the ET and the GSA mentioned above, the probability of the occurrence of ET is greater than GSA, due to the higher absorption coefficient of the Yb^{3+} ions (when compared to that for Er^{3+} ions) at the input wavelength used [13,229]. For the green band emission, electrons excited from $^4I_{11/2}$ to $^4F_{7/2}$ through ET ($^2F_{5/2}$ (Yb^{3+}) + $^4I_{11/2}$ (Er^{3+}) → $^2F_{7/2}$ (Yb^{3+}) + $^4F_{7/2}$ (Er^{3+})) or excited state absorption (ESA; $^4I_{11/2}$ (Er^{3+}) + photon → $^4F_{7/2}$ (Er^{3+})), quickly settle into more stable states $^2H_{11/2}$, $^4S_{3/2}$, through non-radiative phononic relaxation. The emission bands around 523 nm and 545 nm arise due to the radiative transition of electrons from $^2H_{11/2}$ → $^4I_{15/2}$ and $^4S_{3/2}$ → $^4I_{15/2}$ respectively. For the red band transition ($^4F_{9/2}$ → $^4I_{15/2}$), the energy level $^4F_{9/2}$ is populated via two major routes. The first of these is through the de-excitation of electrons from $^4I_{11/2}$ to $^4I_{13/2}$ through phononic relaxation and then excitation from $^4I_{13/2}$ to $^4F_{9/2}$ through ET ($^2F_{5/2}$ (Yb^{3+}) + $^4I_{13/2}$ (Er^{3+}) → $^2F_{7/2}$ (Yb^{3+}) + $^4F_{9/2}$ (Er^{3+})) or ESA ($^4I_{13/2}$ (Er^{3+}) + photon → $^4F_{9/2}$ (Er^{3+})). In the second route, $^4F_{9/2}$ becomes populated through non-radiative relaxation from $^4S_{3/2}$.

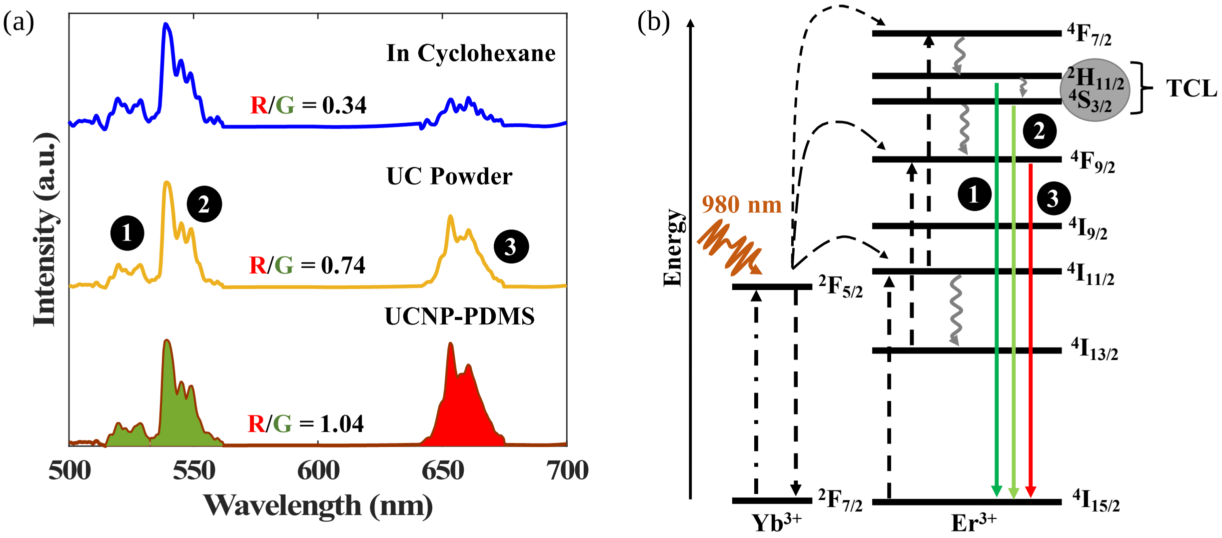

Figure 3. 7: (a) UC emission spectra when UCNPs are dispersed in cyclohexane, UC powder & UCNPs-PDMS. R/G represents the integrated intensities of the red and green bands, shown by red and green colored areas in the lower spectrum shown (b) Partial energy level diagram of Yb^{3+}/Er^{3+} showing the important radiative and non-radiative transitions involved in the UC mechanism. The dash-dotted, dashed, wavy and straight (solid) lines represent the NIR photon excitation, energy transfer, non-radiative relaxation and radiative emission processes respectively.

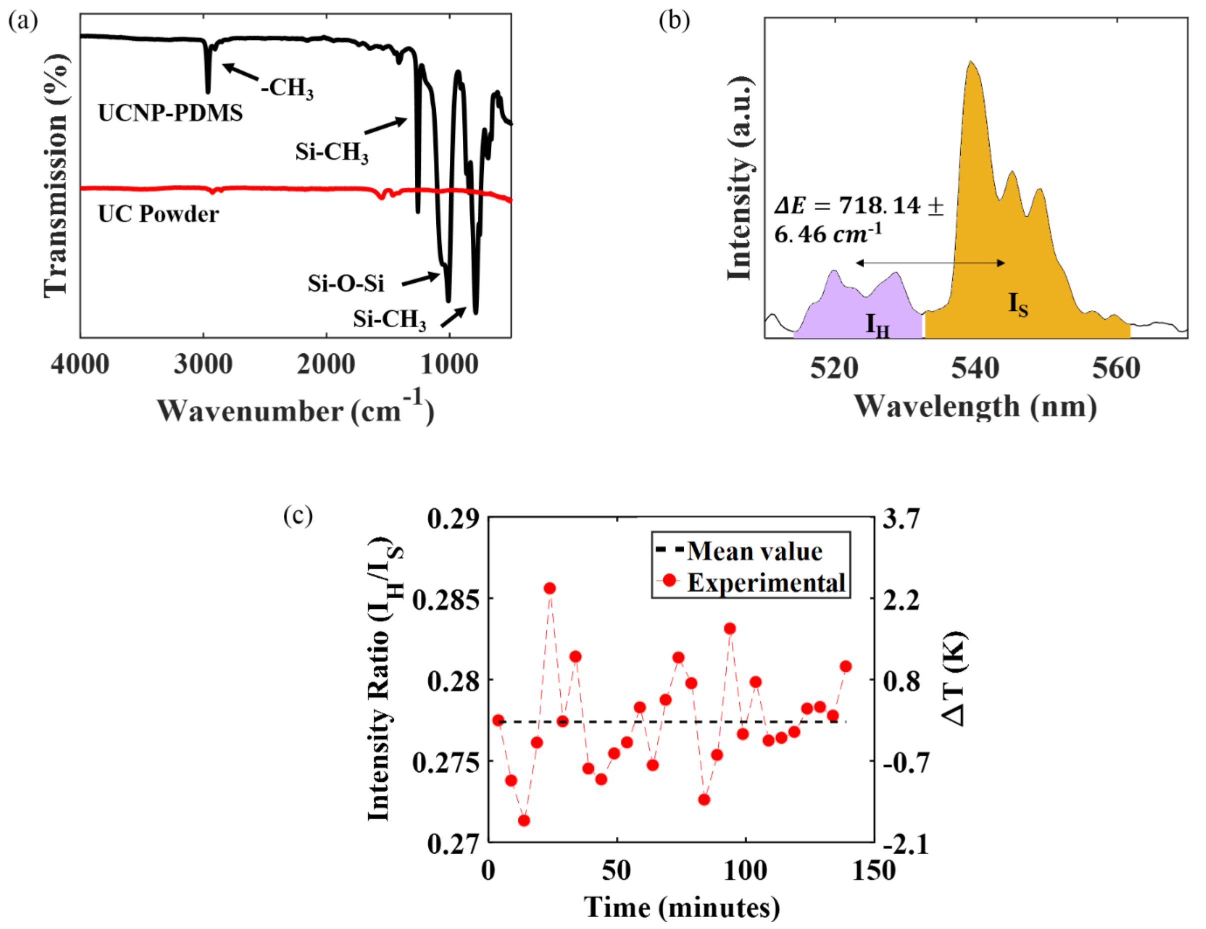

Figure 3. 8: (a) ATR-FTIR response of UC powder and UCNPs-PDMS composite (b) Green UC emission bands of Er^{3+} ions. I_H is the area under curve from 514 nm to 532.3 nm corresponding to the radiative transition $^2H_{11/2} \rightarrow {}^4I_{15/2}$ and I_S is the area under curve from 532.8 nm to 562 nm corresponding to the radiative transition $^4S_{3/2} \rightarrow {}^4I_{15/2}$ (c) Variation of Intensity ratio (I_H/I_S) with time due to laser source heating. The right axis shows the variation of temperature with respect to the mean value.

As discussed in the previous paragraph and is evident from the energy level diagram shown in Fig. 3.7(b), the intensities of the red and green emissions are related through the non-radiative transitions between $^4I_{11/2} \rightarrow {}^4I_{13/2}$ and $^4S_{3/2} \rightarrow {}^4F_{9/2}$, which in turn are strongly affected by the surface properties of the particles, such as surface defects, proximate impurities, surface states, attached ligands, etc. [244]. Therefore, it can be seen from Fig. 3.7(a) that the Red to Green ratio (R/G) is different for all three media. The increase in the R/G ratio in the powder form, in comparison to the colloidal solution UCNPs, has been observed previously and has been attributed to an increase in the cross-relaxation energy transfer between the Er^{3+}- Er^{3+} surface ions, due to the clustering of the Er^{3+} ions in the powder [245]. In the case of the UCNPs-PDMS composite, the observed R/G was highest among the three media considered. This could be due to the combined effect of cross-relaxation between the Er^{3+} - Er^{3+} ions at agglomerated sites and an increase in the non-radiative relaxation between the $^4S_{3/2}$ and $^4F_{9/2}$ levels, caused by the presence of the CH_3 lateral chain of the PDMS near the surface. As can be seen from the ATR-FTIR of the UCNPs-PDMS composite, shown in Fig. 3.8(a), the vibrational energy of the C-H stretching (2962 cm^{-1}) is closer to the energy gap of $^4S_{3/2}{\rightarrow}^4F_{9/2}$ (3200 cm^{-1}), thus increasing the probability of multiphoton relaxation on the transition $^4S_{3/2} \rightarrow {}^4F_{9/2}$.

3.3.2 Temperature response of UC powder-based thermometer

As mentioned above, the ratio of the integrated emission intensities of the green bands under quasi-thermal equilibrium follows Boltzmann's distribution, in accordance with Eq. (3.1).

$$R = \frac{I_H}{I_S} = \frac{g_H \omega_H A_H}{g_S \omega_S A_S} e^{\left(\frac{-\Delta E}{k_B T}\right)} = B e^{\left(\frac{-\Delta E}{k_B T}\right)}, \tag{3.1}$$

where I_H is the area under the emission intensity curve between wavelength the 514 nm and 532.3 nm, as shown by the purple area in Fig. 3.8(b) and I_S represents the area under the emission intensity curve over the wavelength range 532.8 nm to 562 nm (shown by yellow area in Fig. 3.8(b)) g, ω, and A are the degeneracy of the given energy level, the angular frequency of the radiative transitions from the same energy level to the ground level and the emission cross-section respectively, ΔE is the energy gap between the $^2H_{11/2}$ and $^4S_{3/2}$ levels, k_B is Boltzmann's constant and T is the temperature. The pre-exponential constant B is given by $(g_H \omega_H A_H / g_S \omega_S A_S)$. The area under the curve was calculated using Simpson's rule and ΔE was obtained by calculating the difference between the barycenter of I_H and I_S and the corresponding standard error, δE, is the error in that difference across temperature. The barycenter of the corresponding emission was calculated using Eq. (3.2) and the value obtained of ΔE = 718.14 ± 6.46 cm^{-1} is in good agreement with the previously reported values [232,246].

$$\overline{E} = 10^7 * \left(\frac{\sum_{\lambda_1}^{\lambda_2} \lambda I(\lambda)}{\sum_{\lambda_1}^{\lambda_2} I(\lambda)}\right)^{-1} \tag{3.2}$$

Before calibrating the response of the sensor to the external change in temperature, any self-heating due to the laser source that may be present was monitored, over a period of 2.5 hours. Fig. 3.8(c) shows the fluctuation of the intensity ratio (IR) over that period (left axis) and the corresponding temperature fluctuation on the right axis (the mean value of the fluctuation of the IR is considered as a reference). It can be seen from the figure that the temperature variation is within the temperature resolution of the sensor (± 2.7 K: calculation shown later). Moreover, the IR of the sensor remained the same even on reducing the laser source power by half, i.e.

250 mW. These results prove that it is a reasonable assumption that any heating due to the laser source is unimportant.

The variation in the intensity of the green fluorescence of the UC powder, recorded with an increase in temperature from 298 K to 398 K, is shown in Fig. 3.9(a). It can be seen from the main figure and the inset that I_H increases and I_S decreases with the increase in temperature. The ratio of I_H and I_S as function of temperature, as shown in Fig. 3.9(b), fits excellently (R^2 = 0.999) with the function shown in Eq. (3.1), thus indicating that the increase in I_H and the corresponding decrease in I_S are due to the thermal transfer of electrons from energy level $^4S_{3/2}$ to $^2H_{11/2}$. The value of ΔE = 777.15 cm^{-1}, obtained from the fitting, is in good agreement with the value obtained from a barycenter calculation (718.14 ± 6.46 cm^{-1}). The value obtained for the pre-exponential factor *B* also matches well with previously reported values in literature [227,247,248]. Since, the Eq. (3.1) does not take into account the temperature-dependent non-radiative transition rates from $^4S_{3/2}$ and $^2H_{11/2}$, the close fitting of the experimental data to Eq. (3.1) shows that the phonon-assisted non-radiative recombination rate is insignificant over the given temperature range, for the UC powder. Moreover, the intensity ratio variation, with temperature can also be approximated to a linear function over the given temperature range, with R^2 = 0.996, as shown in Fig. 3.10(a).

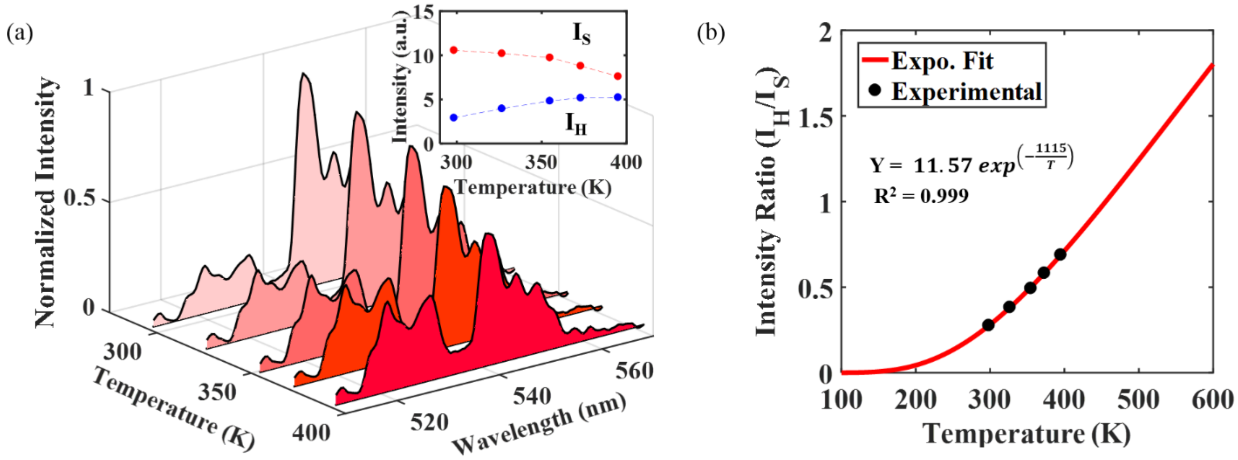

Figure 3. 9: UC powder: (a) Variation of green fluorescence with temperature. The figure has been normalized to the maximum value (obtained at 297 K). The inset shows variation of I_H and I_S with temperature. (b) Experimentally obtained ratio of I_H and I_S against temperature, juxtaposed with an exponential fitting using Eq. (3.1).

The absolute thermal sensitivity (S_A) and the relative thermal sensitivity (S_R) of the thermometer are given by Eq. (3.3) and Eq. (3.4) respectively. It can be seen from Fig. 3.10(b) that S_A increases with temperature and the maximum value obtained for S_A was (4.91 ± 0.02)

$\times 10^{-3}$ K^{-1} at 394.9 ± 0.5 K, whereas S_R monotonically decreases from (12.53 ± 0.03)$\times 10^{-3}$ K^{-1} to (7.15 ± 0.02)$\times 10^{-3}$ K^{-1} with the increase in temperature from 298.2 ± 0.1 K to 394.9 ± 0.5 K. The minimum resolution of the temperature (δT) that could be determined using Eq. (3.5) and Eq. (3.6), was ± 2.7 K. In Eq. (3.6), δI_H and δI_S are the standard errors (standard deviation divided with the square root of the number of repeated measurements made, i.e. 6 in the present case) in I_H and I_S respectively.

$$S_A = \frac{dR}{dT} = R\left(\frac{\Delta E}{k_B T^2}\right) \tag{3.3}$$

$$S_R = \frac{1}{R}\frac{dR}{dT} = \left(\frac{\Delta E}{k_B T^2}\right) \tag{3.4}$$

$$\delta T = \frac{\delta R}{S} \quad , where \tag{3.5}$$

$$\delta R = R\sqrt{\left(\frac{\delta I_H}{I_H}\right)^2 + \left(\frac{\delta I_S}{I_S}\right)^2} \tag{3.6}$$

Since the adhesion of the UC powder to the optical fibre was not strong in comparison to UCNPs-PDMS composite, the probe lifetime reduces considerably as the coating is lost from the fibre, with time, in normal use.

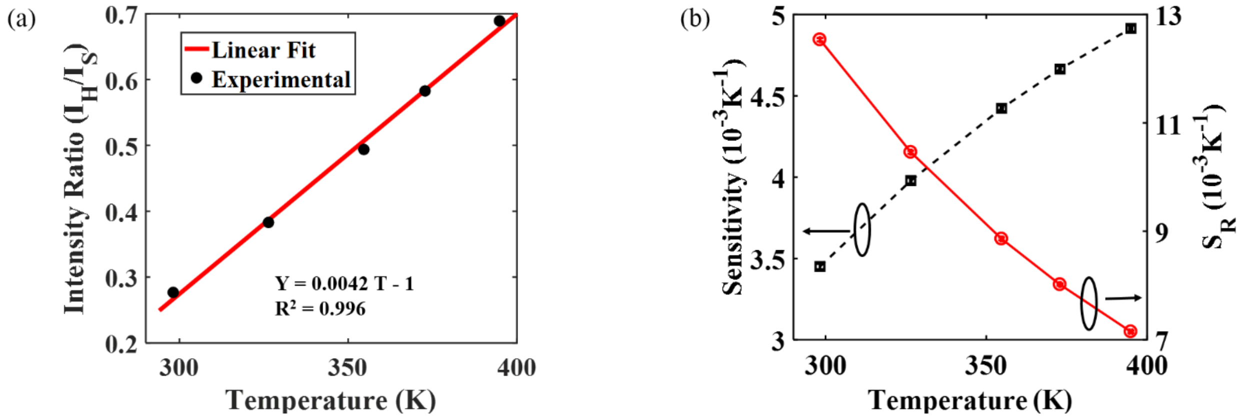

Figure 3. 10: (a) Linear fitting of the ratio obtained of I_H and I_S over the temperature range from 298 K to 395 K (b) Absolute (left) and relative (right) thermal sensitivities obtained for the UC powder.

3.3.3 Temperature response of UCNPs-PDMS composite based thermometer

The variation in the green fluorescence bands of the UCNPs-PDMS composite-coated probe is shown in Fig. 3.11(a). It can be seen from the main figure and the inset (showing the integrated intensity) that that rate of decrease of I_S with temperature is more than for the UC Powder, whereas in contrast to I_S, the rate of increase in I_H is smaller. Furthermore, the variation of the ratio of I_H/I_S with temperature, as shown in Fig. 3.11(b), shows an excellent linear fit ($R^2 = 0.99$), but unlike the UC powder, this does not fit as well ($R^2 = 0.89$) with Eq. (3.1), as shown in Fig. 3.12(a). In the above fitting, $\Delta E = 727.65\ cm^{-1}$ (calculated from Eq. (3.2)) was used. The low R-squared value illustrates that thermal transfer of electrons from $^4S_{3/2} \rightarrow {}^2H_{11/2}$ is not strictly governed by the Boltzmann distribution. The deviation of the thermal response of the UCNPs-PDMS composite from the Boltzmann distribution can be attributed to the increase in the temperature-dependent non-radiative transitions [249] due to presence of the PDMS chemical bonds, as revealed from the ATR-FTIR spectrum (ref. Fig. 3.8(a)), in the vicinity of the surface of Er^{3+} ions.

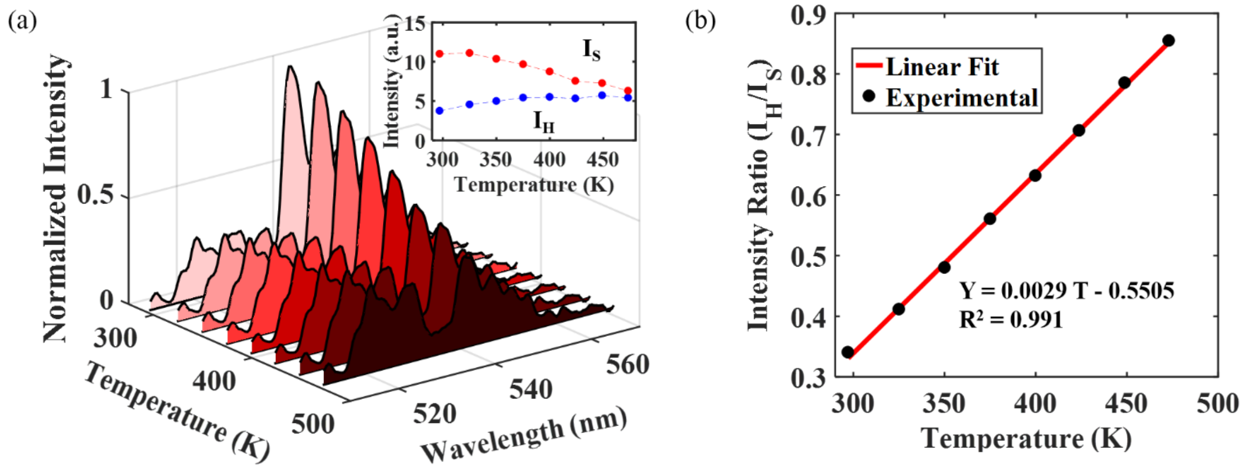

Figure 3. 11: UCNPs-PDMS composite coated probe: (a) Variation in green fluorescence bands with temperature. The inset shows integrated emission intensities (b) Linear fitting of the experimentally obtained ratio of (I_H/I_S), as function of temperature.

The performance of the sensor created using this material shows a linear temperature response and the same sensitivity of $(2.90 \pm 0.40) \times 10^{-3}\ K^{-1}$ across its working temperature range, a positive feature not usually shown by earlier Er^{3+}, Er^{3+}/Yb^{3+} doped glass-based temperature sensors. The reduction in the thermal sensitivity of the UCNPs-PDMS composite (with respect to the UC powder $(4.91 \pm 0.02) \times 10^{-3}\ K^{-1}$) is again due to the reduction in the energy transfer efficiency, owing to the high non-radiative losses. The same pattern was observed in the case of glass-based temperature sensors where glasses having high phonon energies (such silicate and oxide-based glasses) show a lower sensitivity in comparison to glasses having a low phonon energy, such as tellurite glass [229]. The cyclical response of the sensor and the smoothened curve obtained by calculating the mean from 20 neighbouring points is shown by both solid and dotted lines respectively, by varying the temperature from 296 K to 359 K (and

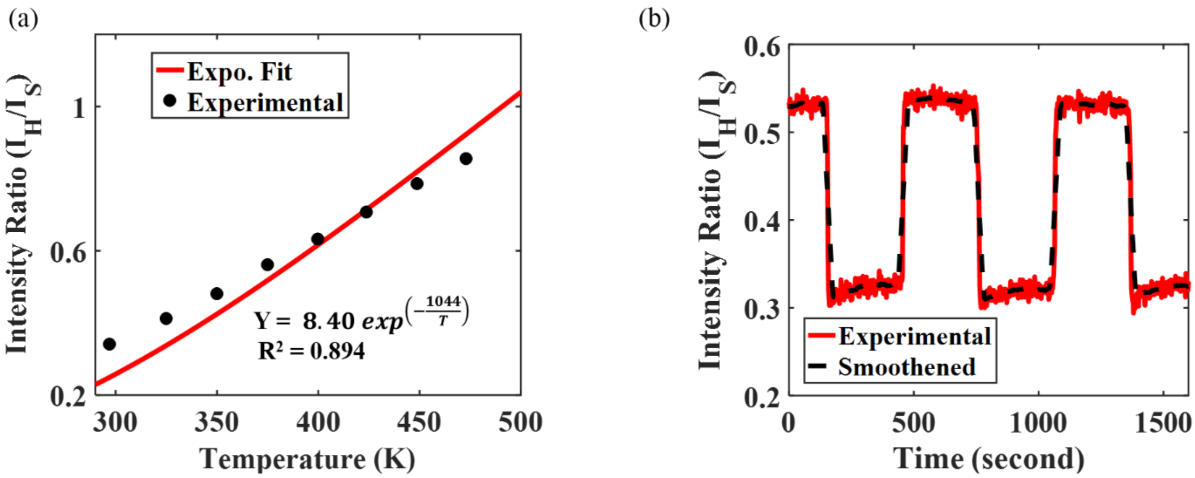

Figure 3. 12: (a) Exponential fitting of the experimentally obtained ratio of (I_H/I_S) as function of temperature, using Eq. (3.1) (b) Cyclic response obtained through repeatedly varying the temperature from 296 K to 359 K (and back). The smoothened curve (dotted) was obtained by calculating local mean from 20 neighboring points is shown as guidance for the eyes.

back) is shown in Fig. 3.12(b). The figure shows that sensor exhibits repeatable reading when exposed to periodically varying temperature. The response time of the sensor, (defined as the time seen on the rising curve between a 10% and 90% peak level i.e. (t_{90}-t_{10})) was found to be ~ 5 seconds, as shown on Fig. 3.13(a). The temperature resolution ± 2.7 K, calculated using Eq. (3.5) & Eq. (3.6), was the same as that for the UC powder. Also, although the silver coating on the tip of sensor is not essential, it increases the overall UC green fluorescence intensity by ~ 23%, as shown in Fig. 3.13(b) and corresponding area under the curve is given in Table 3.1.

Table 3. 1: Silver coating of the tip. Given data is for Fig. 3.13(b).

Area under blue curve (arbitrary units)	13.5
Area under red curve (arbitrary units, as above)	11.0
% increase in intensity	22

The UCNPs-PDMS composite probe shows a repeatable temperature response, measured over a period of several months, benefitting from the good adhesion between the PDMS and the optical fibre (OF) used.

3.3.4 Comparison of performance with previously reported sensors

In order to compare the performance of the probes developed and, in this work considered, their thermal responses were compared to those of a number of others using published information from the literature, collating published data on Er^{3+} or Er^{3+}/Yb^{3+} doped glass-based

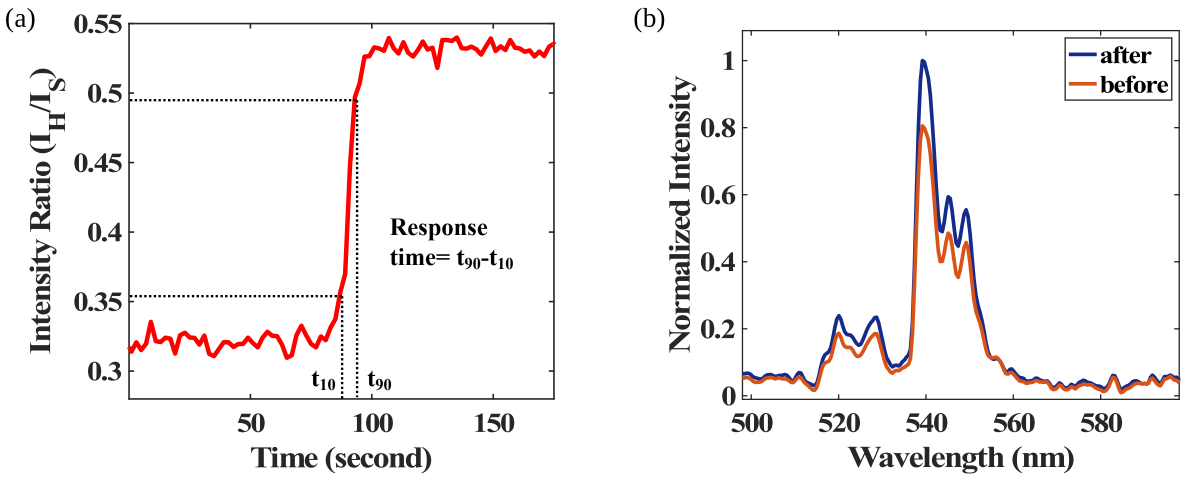

Figure 3. 13: (a) Ramp-up response of the sensor (b) Normalized green fluorescence before and after coating of commercial silver paint.

temperature sensor devices. The minimum sensitivity value of the sensors reported has been extracted from the sensitivity curve of the work of Rohatgi et al [250], using the webplot digitizer tool. As can be seen from Table 3.2, the UCNPs-PDMS-based temperature sensor developed shows a maximum sensitivity of 2.9×10^{-3} K^{-1} within the temperature range of 295-473. The sensitivity and temperature range (which is determined by substrate/host matrix used) of UCNP-PDMS based sensor is not much better than previously reported glass-based sensors, however, the real strength of this sensor lies in:

1) *Low temperature fabrication*. As depicted in Table 3.2 (column 2), UCNPs-PDMS needs around 400 K less temperature for fabrication in comparison to glass based sensors. This enables one to realise the sensor simply using hot plate rather than high temperature furnace. Furthermore, PDMS can be easily dip coated on the fibre. These two characteristics reduces the fabrication complexities, thus saving time, effort and overall cost needed to realise the sensor.
2) *Linear Response*. Unlike most of the sensors previously reported, the maximum sensitivity of this device remains constant across the full operating temperature range, emphasizing the value for applications where such a strongly linear response is desirable. As discussed earlier, this linear response is attributed to increase in non-radiative losses due to presence of the vibrational energy of the C-H stretching (2962 cm^{-1}) closer to the energy gap of $^4S_{3/2}\rightarrow^4F_{9/2}$ (3200 cm^{-1}), thus highlighting the importance of using PDMS.
3) *Longevity*: The use of PDMS increases the longevity of the sensor in comparison to one based on UNCPs powder because of better adhesion of PDMS to the optical fibre and

allowing better heat distribution thus preventing the burning of nanoparticles and increasing the operational temperature range.

Table 3. 2: Comparison of key parameters of the performance of probes developed in this work with those from Er^{3+}/Yb^{3+} doped glass temperature sensors, reported in the literature.

Doped material as the basis of the sensor	Maximum synthesis temperature needed (K)	S_{max} (Temp) 10^{-3} K^{-1} (K)	S_{min} (Temp) 10^{-3} K^{-1} (K)	Sensor Operational temperature Range (K)	Response	Literature Reference
UCNPs-PDMS composite	**583**	**2.9 (295)**	**2.9 (295)**	**295-473**	**Linear**	**This work**
UC Powder	**583**	**4.9 (395)**	**3.5 (295)**	**295-395**	**Exponential/ Linear**	**This work**
Er^{3+}/Yb^{3+}: tellurite glass	973	8.9 (473)	2.1 (278)	278-473	Piecewise Linear	[229]
Er^{3+}/Yb^{3+}: TeO_2–WO_3 glass	1023	2.8 (690)	2.1 (300)	300–690	Exponential	[227]
Er^{3+}/Yb^{3+}: fluorotellurite glasses	1073	5.4 (568)	3.6 (298)	298-568	Exponential	[251]
Er^{3+}/Yb^{3+}: germinate tellurite glass	1173	3.6 (493)	2.1 (293)	293-493	Linear	[228]
Er3+: $Bi_3Ti_{1.5}W_{0.5}O_9$ ceramic	1373	3.1 (423)	1.8 (83)	83-423	Exponential	[252]
Er^{3+}: PbO-Ga_2O_3-SiO_2 glass	1373	2.6 (592)	0.5 (298)	298–650	Exponential	[247]
Er^{3+}: oxyfluoride glass	1473	2.7 (450)	1.8 (250)	250–450	Exponential	[232]
Er^{3+}/Yb^{3+}: silicate glass	1723	3.3 (296)	1.8 (723)	296–723	Exponential	[253]
Er^{3+}: KYb_2F_7 nanocrystal in fluoride glass ceramics	1823	14 (300)	5.4 (480)	300–480	Exponential	[254]

Er^{3+}/Yb^{3+}: K_3LuF_6 nanocrystal in oxyflouride glass ceramic	1823	14 (300)	2.1 (773)	300-773	Exponential	[255]
Er^{3+}: Sr_2YbF_7glass ceramics	1823	6.1 (500)	3.8(300)	300-500	Exponential	[256]
Er^{3+}/Yb^{3+}: β-$NaGdF_4$ nanocrystals glass ceramic	1863	3.7 (563)	2.3 (303)	303-563	Exponential	[257]

3.4 Summary

In the work carried out using ratiometric green emission of an upconverting nanoparticle-polydimethylsiloxane composite, simple, yet practical designs for optical fibre-based thermometers using both UC powder and UCNPs-PDMS composite have been developed and their performance reported. The sensor materials have been synthesized and coated on a multimode optical fibre, to create useable sensor platforms – then and the best of these was selected and explored further. Even though the UC powder showed a higher thermal sensitivity than the UCNPs-PDMS composite ($S_{UC\ powder} = (4.91 \pm 0.02)\times10^{-3}\ K^{-1}$; $S_{UCNP\text{-}PDMS} = (2.90 \pm 0.40)\times10^{-3}\ K^{-1}$), the latter is preferable for many applications over the former due to the stable coating arising from the good adhesion between the PDMS and the optical fibre. The optimum UCNPs-PDMS coated thermometer thus created shows an excellent linear temperature response over the important range 298 K to 493 K, with a same order of sensitivity as had previously been reported for several Er^{3+}/Yb^{3+} doped glass-based sensors, but achieved more simply through a room temperature coating technique. The work has emphasized the advantages of the low temperature synthesis process: the ease of the coating technique, the simple and portable characterization setup used and the creation and optimization of a physically robust probe, all demonstrating the value of this low temperature approach to create a practical and inexpensive sensor system, which can be undertaken in a typical chemical synthesis laboratory.

Chapter 4

Optical fibre-based heavy metal detection using the gold nanoparticles

4.1 Introduction

Contamination of water by heavy metal ions (especially mercury, cadmium, and lead) can cause serious environmental problems and human and animal health problems because of their acute, chronic toxicity to biological organisms [258]. Therefore, sensors to detect heavy metal ions in an aqueous solution are particularly needed to protect the environment. In this regard, spectroscopic-based techniques such as atomic absorption spectroscopy and inductively coupled plasma spectroscopy are amongst the most commonly used methods [259,260]. However, the well-known drawbacks of spectroscopic techniques, such as portability of the equipment (and thus use outside the laboratory), the initial cost of a sensitive spectrometer and onerous sample preparation methods have seen the emergence of new techniques based on nanotechnology. A number of nanoparticle-based heavy metal techniques have been reported in the last two decades and among the varieties of nanoparticles available, GNPs offer unique advantages in terms of a high Refractive Index (RI)-sensitive LSPR peak, coupled to resistance to oxidation, ease of fabrication and well-understood surface chemistry [261,262]. Mishra *et al*. have, for example, incorporated poly-(n-vinyl-2-pyrrolidone) ($(C_6H_9NO)_n$) as a capping agent to create a LSPR-based mercury ion sensor [263]. Similarly, Youngjin Kim *et al.* have demonstrated a colorimetric sensor using the aggregation of 11-Mercaptoundecanoic acid (MUA; $HS(CH_2)_{10}CO_2H$) functionalized GNPs in presence of heavy metal ions [264].

Coating GNPs on an optical fibre (OF) to create a simple-to-fabricate, yet effective sensor probe offers several advantages, including ease of remote sensing capabilities, a potentially high signal-to-noise ratio and resistance to electromagnetic interference. As a result, several GNPs coated optical fibre LSPR-based metal ion sensor designs have been explored in the literature [265–271]. For instance, monoclonal antibodies on GNPs coated OFs have been shown to have an affinity towards the Pb^{2+}- Ethylenedinitrilotetraacetic acid (EDTA; $(HO_2CCH_2)_2NCH_2CH_2N(CH_2CO_2H)_2$) complex. Even though the sensor can detect at the parts per billion (ppb) level, the steps involved to prepare a reliable sensor and implement an effective detection system are quite complicated and thus usually time consuming for the operator.

The key novelty of the work in this Chapter comes from targeting ease of manufacture, creating a simple, portable and robust LSPR-based OF sensor, operating in reflection mode and designed to detect the heavy metals especially Pb^{2+} is reported. The focus in this research is to show proof of concept by detecting Pb^{2+} because it is one of the most harmful, yet common heavy metal found polluting water, often from industrial 'run-off', in the developing world. Thus, recognizing the need of portable sensor to detect heavy metal, in this work, OF coated with indigenously synthesised GNPs is developed and its capability for detecting "heavy metals" is tested by dipping in known concentrations of aqueous solutions of lead nitrate. However, on finding no change in its response, the developed probe is further coated with MUA to make it selective towards heavy metals ions. After functionalization of MUA, a change in amplitude as well as the resonance frequency is observed with change in concentration of the Pb^{2+} ions, arising from the binding of the Pb^{2+}-COOH (carboxyl) group, thus being indicative of the concentration of the Pb^{2+} in the solution.

4.2 Methodology

4.2.1 Chemicals and apparatus used

The following chemicals used were purchased from Sigma-Aldrich: Chloroauric acid ($HAuCl_4.3H_2O$), Sodium citrate tribasic dehydrate ($Na_3C_6H_5O_7.H_2O$), 3-aminopropyl trimethoxysilane (APTMS; $H_2N(CH_2)_3Si(OCH_3)_3$), 97%, Lead nitrate ($Pb(NO_3)_2$) and MUA. In addition, Methanol (CH_3OH; Analytical Reagent Grade), Hydrogen Peroxide (H_2O_2; 37%) solution and Sulphuric acid (H_2SO_4; 95% Laboratory Reagent Grade) were purchased from Fisher Scientific. Silver paint (Electrolube) was purchased from e-bay. The chemicals were used as received from the manufacturer. The multimode OF used, type FT1000UMT, was purchased from Thorlabs.

4.2.2 Characterization instruments

The UV-visible spectrum of the synthesized GNPs was obtained using a LAMBDA 35 UV/VIS spectrometer (Perkin Elmer Inc.), allowing monitoring over the wavelength range from 400 nm to 800 nm (in steps of 1 nm). TEM images were taken at an accelerating voltage of 80 kV and giving 400k magnification. Energy Dispersive X-Ray Analysis (EDAX) was done using a device sourced from Oxford Instruments. The DLS measurement was performed using a ZetaSizer Nano ZEN 3600 (Malvern Instrument).

A tungsten halogen light source, (type LS-1) and a Maya-type 2000PRO were used as the source and the detector respectively, to allow the response of the coated fibre to be acquired. Both components were purchased from Ocean Optics.

4.2.3 Synthesis of GNPs

The GNPs were synthesized by reducing the gold ions present in chloroauric acid with the help of citrate ions, following the steps described in previous work reported in the literature [272]. The approach used 20 mL of 1.0 mM $HAuCl_4.3H_2O$ which was placed in a 50 ml round bottom flask and heated until a rolling boil was achieved. While stirring at 900 rpm, 2 mL of the 1% solution of $Na_3C_6H_5O_7.H_2O$, acting as reducing agent was rapidly added. This solution was then stirred for a further 10 mins, before removing the external heating. At the end of this step, the color of the solution was cardinal red, as expected, due to the formation of the GNPs colloid, as illustrated in Fig. 4.1(a).

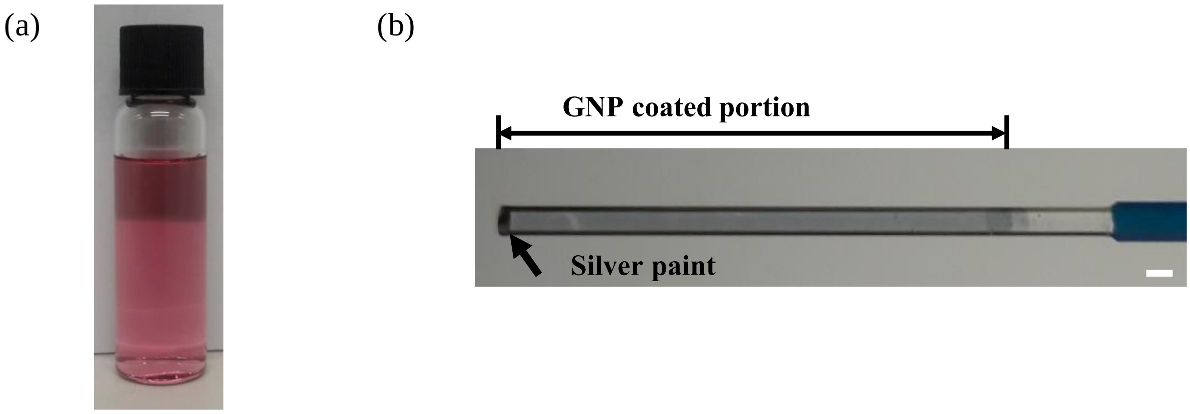

Figure 4. 1: (a) Colloidal Solution (b) Image of the GNPs coated fibre, where the coating area is clearly visible. The white bar at the bottom right represents the reference scale (1 mm).

4.2.4 Sensor preparation process

The synthesized GNPs were then coated on the optical fibre sample discussed, where a diameter of ~1000 µm was used (as this large diameter provides a greater coating surface area), in that way to create the sensor probe used in this work. Before the coating was carried out, both ends of the fibre were carefully polished, as described in Chapter 3 (ref. section 3.2.4), and at one end 2 cm of polymer jacket and the cladding was carefully removed. After removal of the cladding, the GNPs were coated on the cleaned fibre, using the steps described in literature [238]. This process can be summarized as follows: the fibre was washed and hydroxylized with Piranha solution, following which it was cleaned several times in running distilled water and then sonicated in distilled water to ensure complete removal of the last traces of the piranha solution. After drying the fibre in an oven for 1 hour at 393 K, the unclad fibre section was functionalized with APTMS solution in methanol (5% v/v) for 4 hours. This step was followed by washing the functionalized area with methanol and in the end by distilled water. The fibre was placed in an oven at 373 K, overnight, to dry it completely. The next day the functionalized part of the fibre was dipped in synthesized GNPs solution for 6 hours to create a stable and uniform coating, which was visible from the naked eyes, as illustrated in Fig. 4.1(b).

The GNPs immobilized area is made selective to the Pb^{2+} ions by using MUA as a cross-linker. MUA has two terminal functional groups, one being the thiol group and another being the carboxyl group. The thiol group (one of the two terminal functional groups) in the MUA becomes attached to the GNPs via a strong Au-S covalent bond, whereas its other terminal group stays unattached (‘dangling’). This dangling carboxyl group, chemically bound with heavy metals ions, thus makes the fibre selective to the heavy metal ions present in the solution. The MUA is coated on the fibre following the steps described in the literature [273]. In summary, the sensor probe was incubated in 0.3 mM aqueous solution of MUA containing an equivalent amount of sodium hydroxide for 1 hour in at 323 K, where a water bath was used to maintain the constant temperature. After the unbound MUA had been removed in ethanol, the fibre was thoroughly rinsed with distilled water and dried using hot air from a heat gun.

The functionalization of the heavy metal on the MUA-GNPs-coated fibre was performed by dipping the optical fibre in a given heavy metal solution for 1 hour. After this, the fibre was taken out of the solution and dried using the air from the heat gun. The schematic of the steps described are shown in Fig. 4.2.

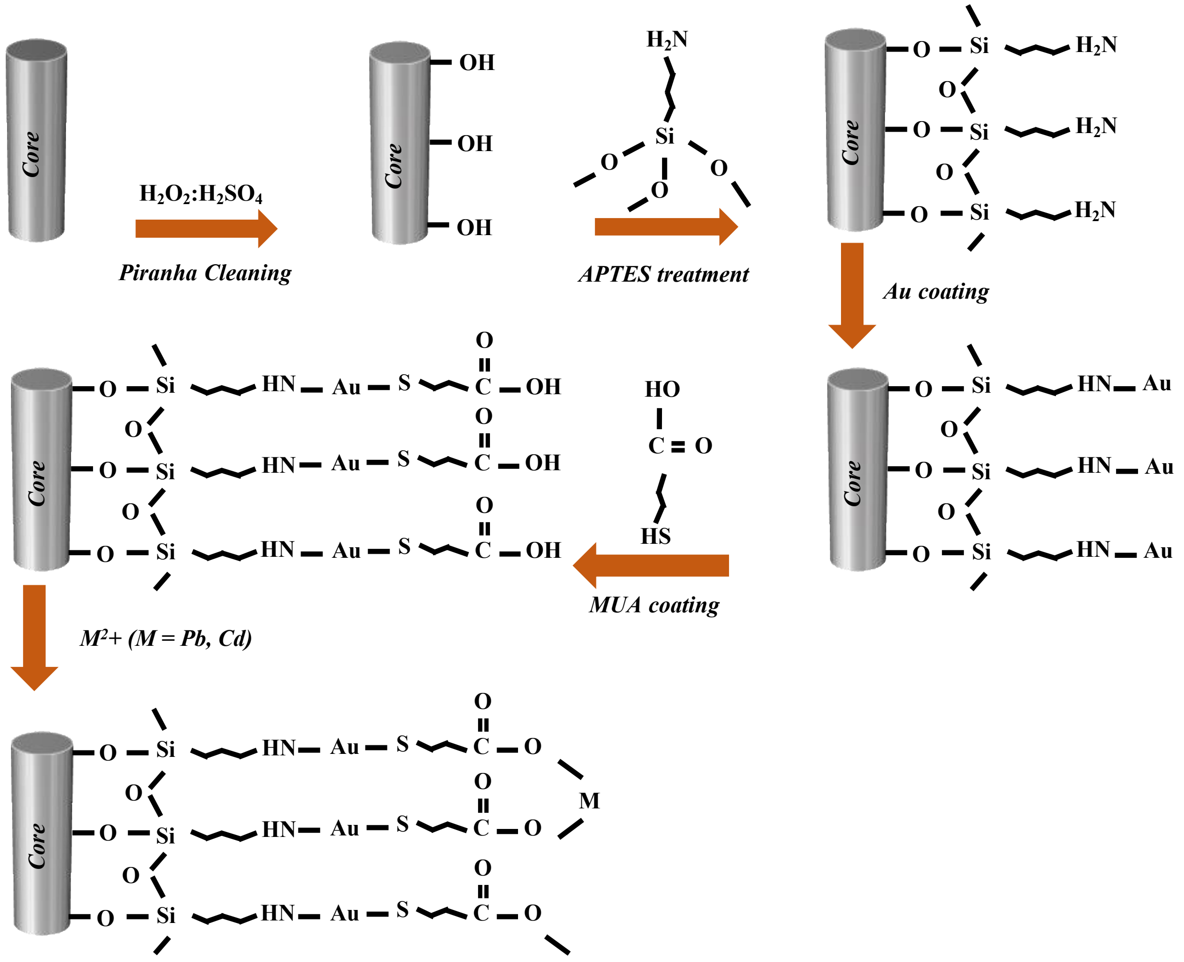

Figure 4. 2: Schematic of the processes involved in the sensor preparation.

After the functionalization was completed, the fibre was coated with silver paint at the distal end to create a sensor to be used in reflection mode, in that way allowing the light to interact twice over the length of the immobilized area effectively, thus increasing the interaction time with the attached heavy metal ions.

4.2.5 Characterization setup for solution refractive index and heavy metal detection

A schematic of the experimental setup developed is shown in Fig. 4.3(a). The broadband tungsten light source used was connected to one end of 1x2 fibre coupler (Ocean Optics, dia. ~ 600 µm). The other two ends of the fibre coupler were connected to the spectrometer and the GNPs-coated fibre, where due to the presence of the silver coating at the tip of the GNPs-coated fibre, the spectrometer was able to collect the reflected light. The real time absorbance spectrum observed over the wavelength range from 400 to 900 nm (and taken with step sizes of 1 nm) was monitored and recorded on the laptop used. The spectrum of the bare (not GNPs-coated) 1000 µm fibre was used as the basis of creating the background signal.

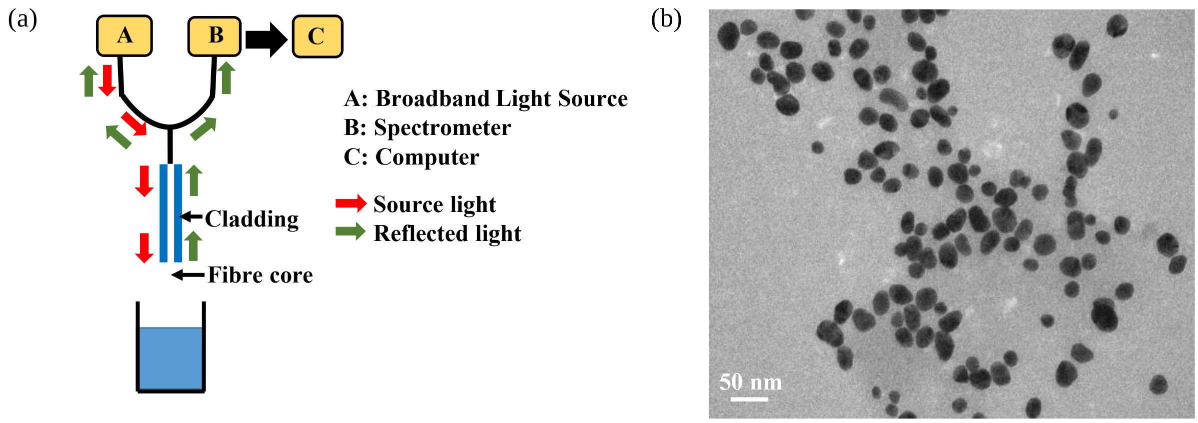

Figure 4. 3: (a) Schematic of the experimental setup used for the characterization of the GNPs coated fibre. (b) TEM image of GNPs.

4.2.6 Modelling technique

The Mie scattering matrix elements, assuming uniform spherical GNPs, were calculated for the wavelength varying from 400 nm to 800 nm at step size of 1 nm using home-made code written in MATLAB. The code was developed and benchmarked following the techniques and results given by Bohren & Huffman in Appendix A [274]. In this work, the refractive index (RI) of gold used was calculated by interpolating the data given by Johnson & Cristy [275]. The RI of medium surrounding the GNPs was taken as 1.33 (i.e. of distil water). The developed code is given in the Appendix 1 of this thesis.

4.3 Results and discussion

4.3.1 Characterization of GNPs

The TEM image of synthesized GNPs is shown in the inset of Fig. 4.3(b). It can be seen for the image that particles are approximately spherical. The size distribution of the GNPs in the colloidal solution, obtained by DLS measurement is shown in Fig. 4.4(a). As seen from the figure, the maximum and average diameter of the synthesized GNPs are 33.34 nm and 22.95 nm respectively with the standard deviation of 12.77 nm. The presence of symmetrical nanoparticles was further corroborated by measuring the UV-VIS spectrum of the colloidal solution, which shows only one LSPR peak at a wavelength of 524 nm, as illustrated in Fig. 4.4(b). For radius = 44 nm, the modelled spectrum of GNPs matches well with the experimentally obtained UV-vis spectrum, as shown in the same figure. The slight mismatch between the experimental and the modelled spectrum, especially at lower wavelength is due to the assumption of uniform spherical GNPs of radius = 44 nm in the modelling. Due to the same assumption, the radius of GNPs obtained from the modelling is different from the average value obtained from the DLS measurement.

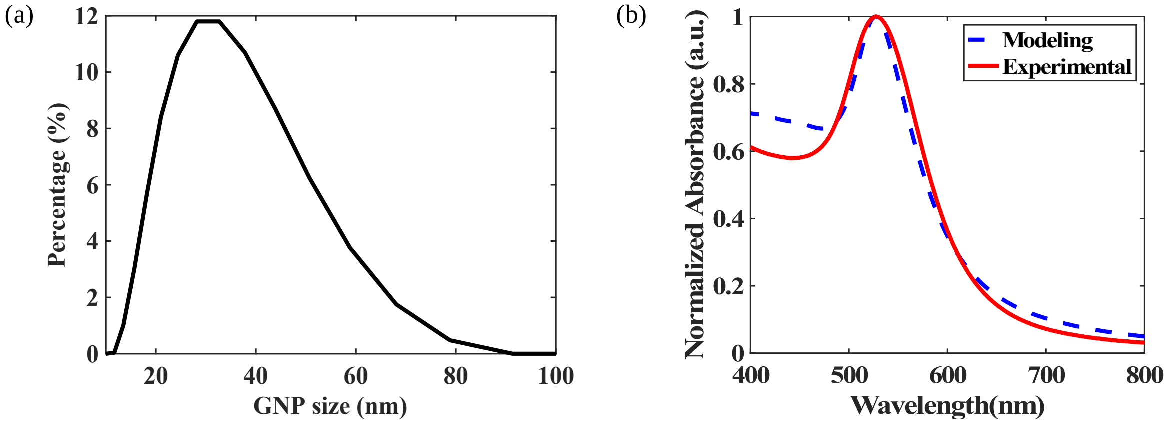

Figure 4. 4: (a) DLS measurement of the GNPs (b) Experimental UV-VIS spectrum obtained, with superimposed results of a model based on Mie scattering.

4.3.2 Refractive index response of GNPs-coated fibre probe

The success in creating the coating of GNPs layer was ensured by measuring its response to solutions of known and varying RI. As seen in the Fig. 4.5(a), with varying RI from 1.33 to 1.42, the absorbance increases with simultaneous red wavelength shift of LSPR peak (peak around 524 nm). The LSPR peak shows a linear variation (R^2 = 0.92) with respect to RI, as shown in Fig. 4.5(b). The sensitivity of the probe, (calculated from fitting) is ≈ 240 nm/RIU.

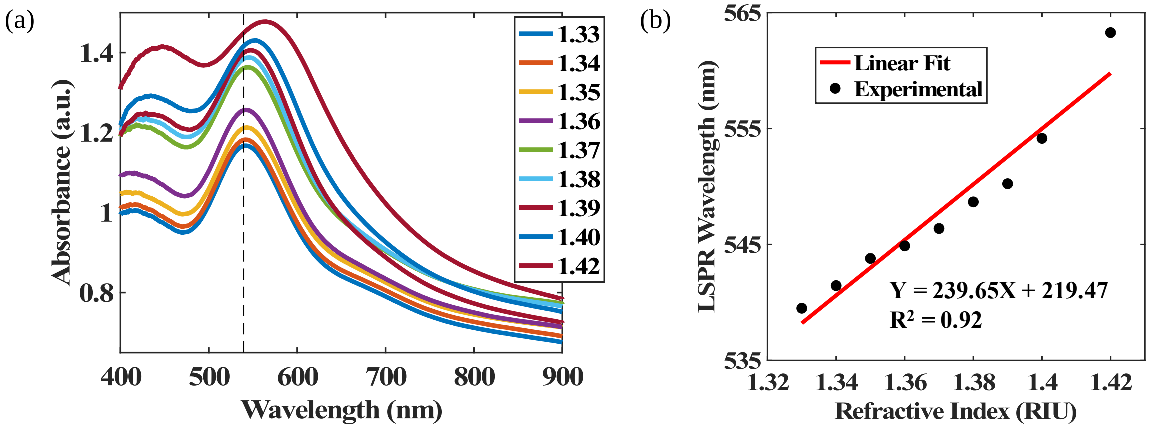

Figure 4. 5: (a) Response of GNPs-coated fibre to increase in absorbance with increase in RI. The vertical dotted line at 545 nm is given as guidance for eyes. (b) Shift in LSPR wavelength in different refractive index media.

4.3.3 Heavy metal ion detection ability of GNPs-coated fibre

The heavy metal detection ability of the GNPs-only coated fibre was evaluated by measuring its response in aqueous Lead Nitrate (LN) solutions of different concentrations (ranging from 0.67 mM to 30 mM). In a way similar to the MUA-GNPs coated fibre (as discussed in next subsection), the GNPs-coated probe was inserted into the solution and left undisturbed for 1 hour. After that hour was completed, the probe was taken out and dried using the air from the hot air gun. Figure 4.6(a) shows the response of the fibre when it was in the solution. It can be seen from the figure that the absorbance of probe has increased in comparison with the response in air (green dotted line), however, there is no change in response on varying LN solutions, which exactly matches the absorption spectrum obtained in Deionized (DI) water (i.e. where there is no lead nitrate). As GNPs coated fibre is sensitive to external RI (discussed in preceding subsection), the lack of response towards varying LN concentration shows that there is no change in the reflective index of solution on varying LN concentration. This conclusion was further corroborated by measuring the RIs of various concentrations of LN solution using an Abbe refractometer. As expected, within the experimental error, all LN solutions showed the RI of 1.33.

A similar result was observed when the fibre was dried, after taking it out from the LN solution. As shown in Fig. 4.6(b), on drying the probe in air, its spectrum moves towards that of air and finally overlaps with the response of air. No change in the absorption spectrum, even after drying the fibre in air, shows that Pb^{2+} ions cannot be immobilized on the GNPs coated fibre, thus highlighting the need of a linker to attach the “heavy metal” ions to the probe. Therefore, the GNPs coated fibre was further functionalized with MUA and its responses are discussed in the next subsection.

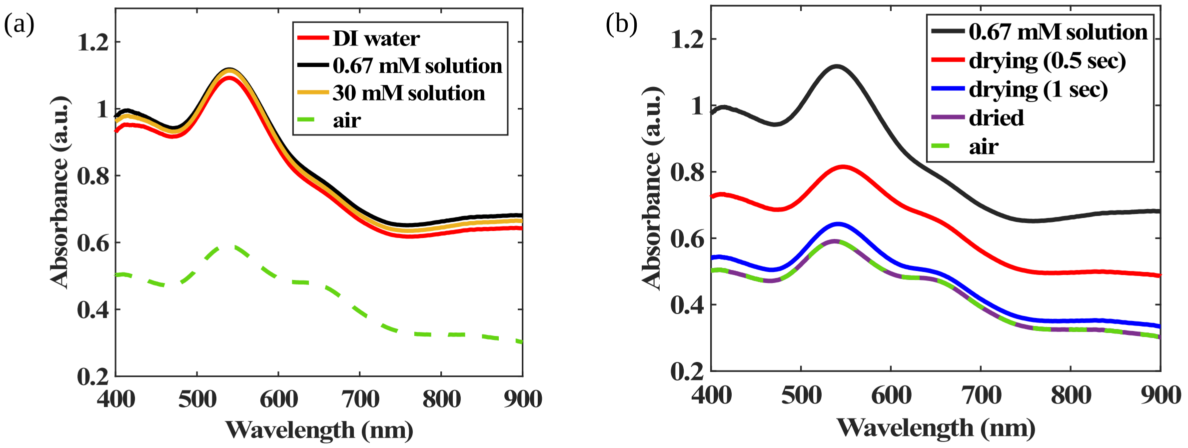

Figure 4. 6: Response of GNPs-coated fibre in (a) the Lead Nitrate (LN) solution (b) After removed from LN solution, dried and monitored in air.

4.3.4 Lead ion detection using MUA-incorporated GNPs coated fibre

The comparison of the absorbance spectra of the MUA-GNPs-coated fibre with (only) the GNPs-coated fibre is shown in Fig. 4.7(a). In the case of the MUA-GNPs fibre, there is a red shift in the spectrum. This red shift in the spectrum indicates the successful immobilization of the MUA on the fibre. The broadening of the absorbance spectrum after coating of MUA (can be seen in the same figure), may be due to the presence of covalent bonding between the carboxyl group of the MUA and the gold particles, where the carboxyl group acts as the ‘anchor’ for the immobilization of a heavy metal ions (such as Pb^{2+}), on the GNP surface. The direct evident of the attachment of MUA to gold surface is obtained from the EDAX analysis. The presence of high percentage of carbon and oxygen in the EDAX measurement carried out on the portion (highlighted in Fig. 4.7(b)) of the GNPs-MUA coated fibre further confirms successful coating of MUA.

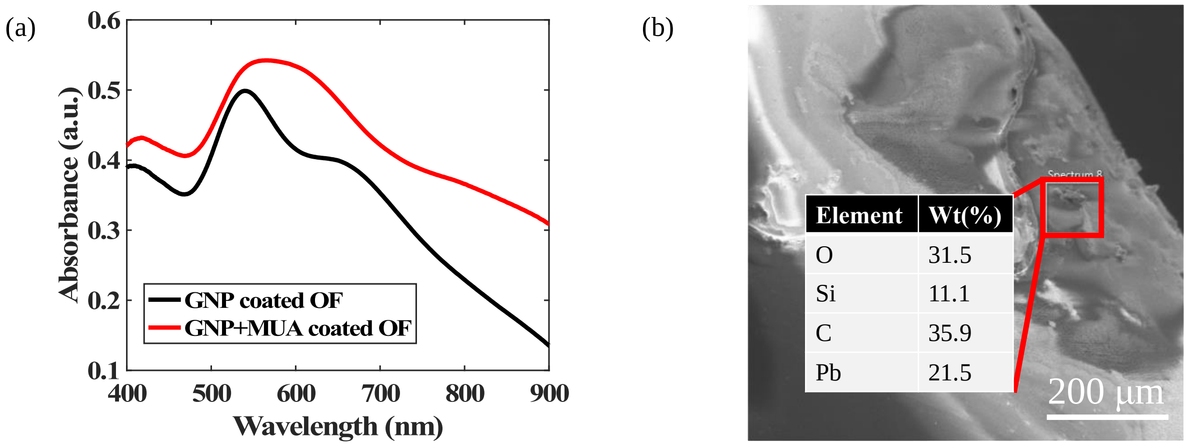

Element	Wt(%)
O	31.5
Si	11.1
C	35.9
Pb	21.5

Figure 4. 7: (a) Absorbance spectrum of Au NP-coated fibre before and after coating with MUA. (b) SEM image of GNPs-MUA-coated fibre after immobilization in Lead Nitrate (LN) solution. The table shows the EDAX analysis of the highlighted section.

Figure 4.8(a) and 4.8(b) respectively shows the absorbance spectra of the MUA-GNPs-coated fibre in different concentration of LN solution when probe is inside the solution and when it is taken out of solution, afterward dried completely. It can be seen from the Fig. 4.8(a) that the LSPR absorbance peak remains almost unchanged during the incubation of the LSPR probe, while it remains in a LN solution of different concentration. However, the change in position of LSPR peak is quite evident when the probe is removed from the solution and afterwards dried and monitored in air, as shown in Fig. 4.8(b). As can be seen from the results shown in Fig. 4.8(c), an increase in the Pb^{2+} ion concentration (to 100 mM) results in the LSPR wavelength being red shifted from 551.7 nm to 578.9 nm. The slope of the linear fitting of LSPR red shift gives the Pb^{2+} ion sensitivity 0.28 nm/mM.

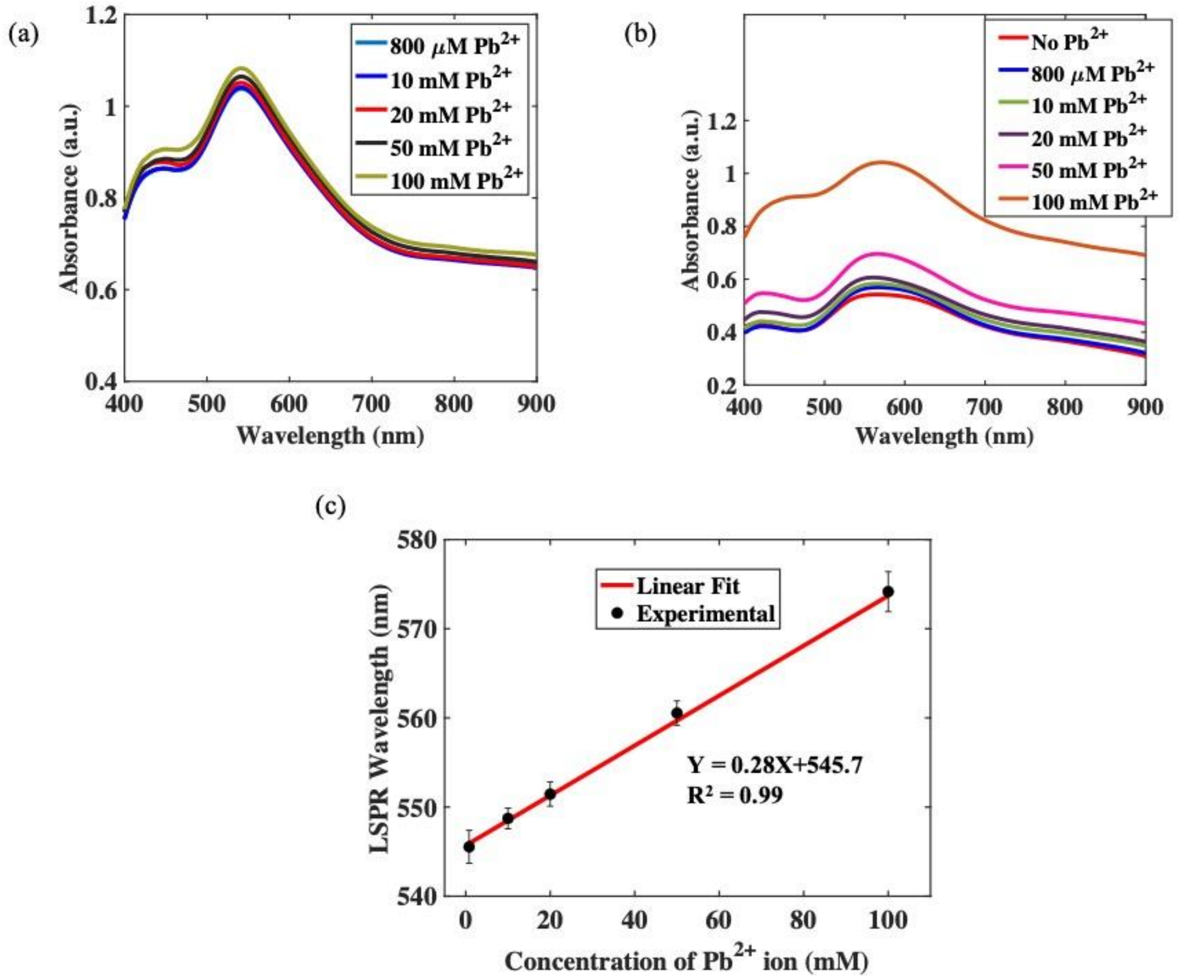

Figure 4. 8: Response of MUA-coated fibre in (a) the Lead Nitrate (LN) solution (b) After removed from LN solution, dried and monitored in air (c) Pb^{2+} concentration versus LSPR wavelength.

Previously it had been noted that the RI variation of the LN solution, due to the change in its concentration, was relatively insignificant (the refractive index of the Pb^{2+} solution was noted to vary slightly – by less than 0.006, creating a range from 1.330 to ~1.336 – due to the change of the concentration from 0.67mM to 150mM). Such a refractive index change was within the measurement error of the GNPs based sensor probe. Therefore, the recorded spectra from the GNPs-MUA probe were similar, whether the LN solution or DI water were used. When the GNPs-MUA coated probes were removed from the LN solution, it was very clear that some Pb^{2+} ions had been immobilized by use of the MUA carboxyl group. Subsequently, when the Pb^{2+} ion-immobilized probes were dried in air, an RI change due to Pb^{2+} contact was observed. Therefore, the red wavelength shift seen from the LSPR spectra in air is a consequence of the Pb^{2+} ion detection ability of the sensor, through the GNPs-MUA-incorporated LSPR optical fibre probe developed.

In comparison to MUA, the EDTA has more affinity towards heavy metal ions [264]. Therefore, the lead ions bonded to MUA can be partially removed by dipping the optical fibre probe into EDTA solution and after thoroughly washing with distil water, it can be reused. However, as previously reported in literature [264,276], the response of chemical sensors generally deteriorate after every round of reusage because it is not possible to remove all bonded Pb^{2+} ions.

4.3.5 Performance comparison with prior work

In this work, a sensitivity 0.28 nm/mM and limit of detection of 800 µM (65 ppm) of Pb^{2+} ions were obtained. In comparison to earlier reported limit of detection values of heavy metal ions, such as 0.36 µM for Pb^{2+} [262], 0.1µM for Hg^{2+} [263], 25µM Hg^{2+} + 79µM Cu^{2+} [270], this reported value is slightly higher. However, the real strength of this sensor lies in its reusability, portability, mechanical robustness, ease of fabrication and low-cost setup because it does not need expensive and bulky source, detector, collimator, lenses, fusion splicer, etc.

4.4 Summary

In this collaborative proof of concept work, the design and application of a GNPs coated optical fibre LSPR sensor has been demonstrated for detecting heavy metal ions present in aqueous solution. This was achieved by functionalizing GNPs-coated OF with MUA to immobilize the lead ions. In calibrations carried out, the Pb^{2+} ion sensitivity recorded was 0.28 nm/mM. This study establishes the principle of creating a heavy metal sensor of this type by using such a coated optical fibre design.

Further work is to increase the sensitivity from the millimole range, through optimizing parameters such as the gold nanoparticle size, the MUA drying temperature and the MUA concentration.

Chapter 5

Determination of aspect-ratio distribution of gold nanorods in a colloidal solution using UV-visible absorption spectroscopy

5.1 Introduction

Gold Nano Rods (GNRs), due to their asymmetric structure and unlike other symmetrical gold nanoparticles such as spheres, shells, cages and cubes exhibit two plasmonic resonances, as has been discussed in Chapter 2. As discussed previously in subsection 2.4.2, the plasmonic resonance corresponding to the shorter wavelength (around 520 nm), known as the T-LSPR, arises due to the collective oscillation of free electrons in the presence of an external electromagnetic field along the transverse dimension of the GNRs whereas, the resonance at the longer wavelength, known as L-LSPR, is due to the oscillation of free electrons along the longitudinal dimension. Due to the dependence of the position of the L-LSPR on their Aspect Ratio (the length (L) divided by the width (W) and designated here by AR) and the external refractive index, supported by well understood surface chemistry [277–280], GNRs have found applications in a wide variety of fields which are as diverse as biomedical sciences [281–284], sensor development [285–288], imaging [289,290] and electronics-based applications such as solar cells [291] development. For example, in photothermal cancer therapy (refer section 2.3.5. for the underlying principle), GNRs are preferred over GNPs because the position of L-LSPR can be tuned in entire near infrared regime (NIR) by varying AR. Since, human tissues are more transparent in NIR wavelength, tumours seated deep within tissue can be accessed and treated with GNRs [292,293].

In one of the sensing applications, Yu and Irudayaraj used the AR sensitive L-LSPR resonance to demonstrate multiplexed biosensor for detecting multiple target molecules [288]. For this, they synthesized GNRs with three different ARs (thus having three L-LSPR peaks), functionalised each with different antibodies and add them together to realise solution-phased based multiplex biosensor. The addition of a target molecules the solution caused significant red shift in the corresponding L-LSPR due to target specific binding and small shift in the other two peaks due to non-specific bindings. Similarly, addition of two targets and three targets resulted in red-shifts of corresponding two and three L-LSPR peaks respectively due to target specific bindings. Mubeen *et al.* showed the usage of GNRs in photovoltaic by developing the plasmonic photovoltaic device, which consists of dense array of vertically oriented GNRs coated with a 10 nm wide- band gap oxide (TiO_2) and a low work function metal (Ti) [291]. Here, the majority of charges were derived from excitation of localised surface plasmon in GNRs and short circuit photocurrent in the range 70-120 μAcm^2 were obtained for simulated one-sun AM1.5 illumination.

‘Bottom-up’ synthesis methods such as the seeded method [294], the electrochemical reduction method [295] or photochemical reduction [296] of GNRs generally produce poly-dispersed solutions with various ARs of the GNRs. Therefore, knowing the distribution of the ARs in the synthesized colloidal solution is important as it reveals the quality of the solution and hence its potential to be used in many possible applications. For example, it is important to have a narrow size distribution in solution for uniform and long self-assemblies of GNRs [19]. In this regard, TEM provides a very effective means for determining the actual size of the GNRs but obtaining a statistically accurate size distribution of the colloidal solution is difficult because of the limited numbers of GNRs spanning over a few selected images which are used to calculate the average AR. Further, GNRs tend to `self-sort' based on their sizes and shapes while drying on the TEM grid and therefore the selection of the position for imaging become important [297]. The measurement of even hundreds of GNRs from TEM images is an onerous process and most importantly, TEM devices are not readily accessible to all research groups. In recent years, use of DLS techniques have been introduced to determine the size distribution of nanoparticles but this approach is limited to spherical particles and it cannot be used for anisotropic particles, such as GNRs.

In previous work, Eustis & Sayed [298] have demonstrated that the Mie-Gans theory could be used to determine the distribution of ARs in a given solution, by theoretically fitting the inhomogeneously-broadened LSPR absorption spectrum obtained using UV-Visible spectrometer. However, the fitting technique used was manual and therefore very cumbersome. Further, all the fittings employed were based on the assumption that the solvent used was pure deionized water and therefore the effect of contamination or impurities in the solvent were ignored. In this work, these important drawbacks are addressed by developing an algorithm based on the Bellman Principle of Optimality, to automate the curve-fitting process. The effect of the external medium was considered by taking into account the dielectric constant, ε_m, of the solvent, while the fitting process was undertaken.

5.2 Background theory and algorithm formulation

According to the modified Gans' Model [211], the absorption coefficient (γ) of the GNRs in the colloidal solution considered is given by Eq. (5.1).

$$\gamma = \frac{2\pi N V \varepsilon_m^{\frac{3}{2}}}{3\lambda} \sum_{J=A,B,C} \frac{\left(1/P_J^2\right)\varepsilon_2}{\left(\varepsilon_1 + \left[\frac{1-P_J}{P_J}\right]\varepsilon_m\right)^2 + \varepsilon_2^2} \tag{5.1}$$

where,

$$P_A = \frac{1-e^2}{e^2}\left[\frac{1}{2e} ln\left(\frac{1+e}{1-e}\right) - 1\right] \tag{5.2}$$

$$P_B = P_C = \frac{1-P_A}{2}, \tag{5.3}$$

and

$$e = \sqrt{1-\left(\frac{W}{L}\right)^2} \tag{5.4}$$

In the above equations, P_A, P_B and P_C are dependent on the shape of the GNRs as they also depend on the variable, e, which in turn is an inverse function of the AR, i.e. the ratio of the length (L) to width (W). N is number of GNRs per unit volume, V is the volume per particle, λ is the wavelength, ε_m is the dielectric constant of the surrounding medium and ε_1 and ε_2 represent respectively the real and imaginary parts of the permittivity for the gold used.

In this work, the permittivity of the gold used was calculated by interpolating the data given by Johnson & Cristy [275]. Using an approach that is similar to that seen in the previous work, as reported by Eustis & Sayed in [298], V is considered as a constant, as, the average volume of the GNRs remains constant across the ARs in most of the seed synthesis methods. Figures 5.1(a) and (b) show the modelled dependence of the AR and ε_m respectively on the LSPR, obtained by using Eq. (5.1) for arbitrary chosen value of ε_m and AR. In Fig. 5.1(a), while studying the effect of AR, ε_m was kept constant at 1.77. Similarly, in Fig. 5.1(b), the effect of ε_m was observed for a fixed value of AR = 2.5. It can be seen from both figures that, with the increase in the AR and ε_m, L-LSPR shows a significant red wavelength shift.

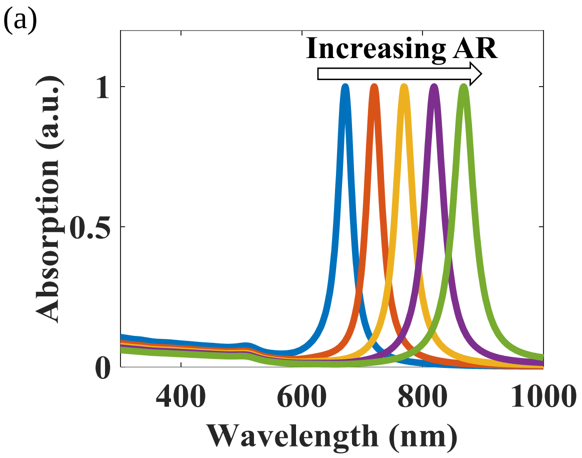

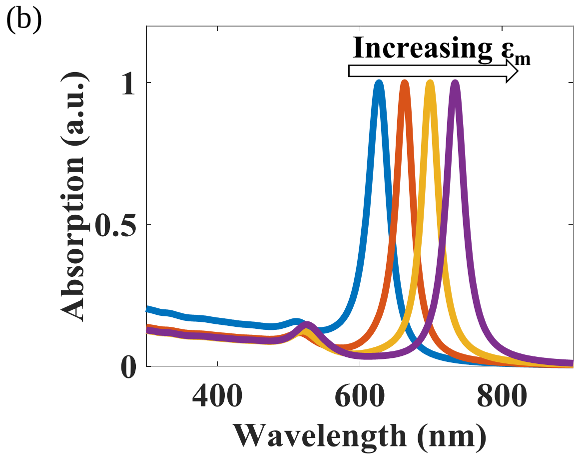

Figure 5. 1: Self-normalized modelled absorption spectra showing the red shift in the Longitudinal Localised Surface Plasmon Resonance due to an increase in (a) the Aspect Ratio (AR) and (b) the Permittivity of the surrounding medium (ε_m).

The first step in automating the theoretical fitting to the experimentally obtained value of L-LSPR is to rearrange and thus represent the absorption coefficient seen in Eq. (5.1), as the product of two variables, as shown in Eq. (5.5). The first variable (A_λ^{AR}), contains all the size and frequency dependent terms (as shown in Eq. (5.6)), whereas the second variable (N^{AR}) is the number of particles per unit volume of a given AR.

$$\gamma = A_\lambda^{AR} N^{AR}, \tag{5.5}$$

where,

$$A_\lambda^{AR} = \frac{2\pi\varepsilon_m^{\frac{3}{2}}}{3\lambda} \sum_{J=A,B,C} \frac{\left(1/P_J^2\right)\varepsilon_2}{\left(\varepsilon_1 + \left[\frac{1-P_J}{P_J}\right]\varepsilon_m\right)^2 + \varepsilon_2^2}, \tag{5.6}$$

In the self-normalized absorption spectrum of a poly-disperse colloidal solution, the value of N^{AR} varies from 0 and 1, thus indicating the contribution of GNRs of a particular AR in the total absorption. The N^{AR} equal to 0 shows that the solution is devoid of GNRs of a given AR, whereas N^{AR}equal to 1 indicates the mono-dispersed GNRs solution. Therefore, for a poly-dispersed colloidal solution having "*n*" varieties of ARs, the resultant absorption, at a given wavelength, say (λ_x), is the cumulative effect of the contribution of the individual ARs. Mathematically, this can be represented as shown by Eq. (5.7):

$$A_{\lambda_x}^{AR^1} N^{AR^1} + A_{\lambda_x}^{AR^2} N^{AR^2} + \cdots + A_{\lambda_x}^{AR^n} N^{AR^n} = A_{\lambda_x}^{exp} \tag{5.7}$$

where,

$A_{\lambda_x}^{AR^n}$is the absorption of the *n^th^* AR at λ_x, assuming N^{AR^n} is 1, i.e. the absorption of a mono-dispersed GNRs solution with respect to the *n*th AR GNRs. This is calculated using Eq. (5.6), for given λ_x at $\varepsilon_m = 1.77$. N^{AR^n} is the actual contribution of a *n*th AR, and, unknown in the present case. $A_{\lambda_x}^{exp}$ is the experimentally obtained value of the absorption at λ_x, obtained using an analysis of UV-Vis spectrum of a chemically-synthesized colloidal solution.

Spanning λ_x over the entire LSPR wavelength range i.e. ≥ 615 nm, in "m" steps will constitute an over-determined set of linear equations (with *n* variables, *m* equations; where $n \leq m$). This set of over-determined equations in the matrix notation can then be expressed as:

$$\underbrace{\begin{bmatrix} A_{\lambda_1}^{AR^1} & A_{\lambda_1}^{AR^2} & \cdots & A_{\lambda_1}^{AR^n} \\ A_{\lambda_2}^{AR^1} & A_{\lambda_2}^{AR^2} & \cdots & A_{\lambda_2}^{AR^n} \\ \vdots & \vdots & \ddots & \vdots \\ A_{\lambda_m}^{AR^1} & A_{\lambda_m}^{AR^2} & \cdots & A_{\lambda_m}^{AR^n} \end{bmatrix}}_{\boldsymbol{A}} \times \underbrace{\begin{bmatrix} N^{AR^1} \\ N^{AR^2} \\ \vdots \\ N^{AR^n} \end{bmatrix}}_{\boldsymbol{N}} = \underbrace{\begin{bmatrix} A_{\lambda_1}^{exp} \\ A_{\lambda_2}^{exp} \\ \vdots \\ A_{\lambda_m}^{exp} \end{bmatrix}}_{\boldsymbol{A_{exp}}} \tag{5.8}$$

Eq. (5.8), being over-determined in nature, cannot be solved to find the exact values of $\boldsymbol{N}$. Nevertheless, the value closest to the solution, represented by $\boldsymbol{N}^*$, can be found by using a Least Squares Approximation (LSA), employing Eq. (5.9), where ($\boldsymbol{A'}$) and ($\boldsymbol{A^{-1}}$) represent respectively the transpose and inverse of the matrix $\boldsymbol{A}$ [299] where

$$\boldsymbol{N}^* = ((\boldsymbol{A'A})^{-1}\,\boldsymbol{A'})\boldsymbol{A}_{exp} \tag{5.9}$$

However, the LSA may result in non-physical values of $\boldsymbol{N}^*$, such as negative values and/or those greater than unity. Therefore their optimal physical values i.e. those lying between 0 and 1, are found using Bellman's dynamic programming Principle of Optimality (BPO) [300].

Using the BPO approach, whatever the value of a given element of $\boldsymbol{N}$, say N^{AR^x}, is chosen, the calculated values of the remaining elements of $\boldsymbol{N}$ will be optimal with respect to the chosen value of N^{AR^x}. This ensures that each set of values (for every N^{AR^x}) is optimized and therefore, out of all the chosen values of N^{AR^x}, the value that yields the least fitting error will be the optimal value. Mathematically, to find the optimal value of N^{AR^1} lying between 0 and 1, it is varied between 0 to 1, using a step size of 0.001. For each step value, N^{AR^1} is multiplied by the first row of $\boldsymbol{A}$ in Eq. (5.8) and shifted to the right-hand side, represented by $\boldsymbol{A}_{red}^{(1)}$ in Eq.

(5.10). This operation modifies Eq. (5.8) to give Eq. (5.11), where $\boldsymbol{A_T^{(1)}}$, $\boldsymbol{N_T^{(1)}}$ and $\boldsymbol{A_{red}^{(1)}}$ are the truncated versions of $\boldsymbol{A}$, $\boldsymbol{N}$ and $\boldsymbol{A_{exp}}$ respectively.

$$\boldsymbol{A_{red}^{(1)}} = \boldsymbol{A_{exp}} - N^{AR^1}\begin{bmatrix} A_{\lambda_1}^{AR^1} \\ A_{\lambda_2}^{AR^1} \\ \vdots \\ A_{\lambda_m}^{AR^1} \end{bmatrix} \tag{5.10}$$

$$\underbrace{\begin{bmatrix} A_{\lambda_1}^{AR^2} & \cdots & A_{\lambda_1}^{AR^n} \\ A_{\lambda_2}^{AR^2} & \cdots & A_{\lambda_2}^{AR^n} \\ \vdots & \ddots & \vdots \\ A_{\lambda_m}^{AR^2} & \cdots & A_{\lambda_m}^{AR^n} \end{bmatrix}}_{\boldsymbol{A_T^{(1)}}} \times \underbrace{\begin{bmatrix} N^{AR^2} \\ \vdots \\ N^{AR^n} \end{bmatrix}}_{\boldsymbol{N_T^{(1)}}} = \boldsymbol{A_{red}^{(1)}} \tag{5.11}$$

In shorthand notation, the truncated matrices of Eq. (5.11) can be written as,

$$\boldsymbol{A_T^{(1)}}\boldsymbol{N_T^{(1)}} = \boldsymbol{A_{red}^{(1)}} \tag{5.12}$$

The closest unconstrained optimal values of $\boldsymbol{N_T^*}$ using the LSA, the corresponding Error ($\boldsymbol{Er}$) and Summed Square Error (SSE) are found using the following set of equations:

$$\boldsymbol{N_T^*} = \left(\left(\left(\boldsymbol{A_T^{(1)}}\right)'\boldsymbol{A_T^{(1)}}\right)^{-1}\left(\boldsymbol{A_T^{(1)}}\right)'\right)\boldsymbol{A_{red}^{(1)}} \tag{5.13}$$

$$\boldsymbol{Er} = \boldsymbol{A_{red}^{(1)}} - \boldsymbol{A_T^{(1)}}\boldsymbol{N_T^*} \tag{5.14}$$

$$SSE = \boldsymbol{Er'Er} \tag{5.15}$$

The SSE can be calculated for all the step values of N^{AR^1} and among them, the one which gives the least SSE is taken as the optimized value of N^{AR^1}, represented by $N_{opti}^{AR^1}$. Since, in calculating $N_{opti}^{AR^1}$, all the unconstrained possibilities of N^{AR^2} to N^{AR^n} are considered, there is no need to recalculate the value of N^{AR^1} while calculating their optimal values. For example, to calculate the optimal value of N^{AR^2}, it is varied between 0 to 1 with a step size of 0.001. Since, $N_{opti}^{AR^1}$ has already been calculated in the previous step, for each step value of N^{AR^2}, the first row of A (in Eq. (5.8)) is multiplied by $N_{opti}^{AR^1}$, the second row is multiplied by N^{AR^2} and shifted to the right-hand side, i.e. subtracted from $\boldsymbol{A_{exp}}$, as shown in Eq. (5.16). This operation will reduce the matrices $\boldsymbol{A}$, $\boldsymbol{N}$, $\boldsymbol{A_{exp}}$ in Eq. (5.8) to $\boldsymbol{A_T^{(2)}}$, $\boldsymbol{N_T^{(2)}}$, $\boldsymbol{A_{red}^{(2)}}$ respectively, as shown in Eq. (5.17).

$$\boldsymbol{A}_{\boldsymbol{red}}^{(2)} = \boldsymbol{A}_{\boldsymbol{exp}} - N_{opti}^{AR^1} \begin{bmatrix} A_{\lambda_1}^{AR^1} \\ A_{\lambda_2}^{AR^1} \\ \vdots \\ A_{\lambda_m}^{AR^1} \end{bmatrix} - N^{AR^2} \begin{bmatrix} A_{\lambda_1}^{AR^2} \\ A_{\lambda_2}^{AR^2} \\ \vdots \\ A_{\lambda_m}^{AR^2} \end{bmatrix} \tag{5.16}$$

$$\underbrace{\begin{bmatrix} A_{\lambda_1}^{AR^3} & \cdots & A_{\lambda_1}^{AR^n} \\ A_{\lambda_2}^{AR^3} & \cdots & A_{\lambda_2}^{AR^n} \\ \vdots & \ddots & \vdots \\ A_{\lambda_m}^{AR^3} & \cdots & A_{\lambda_m}^{AR^n} \end{bmatrix}}_{\boldsymbol{A}_{\boldsymbol{T}}^{(2)}} \times \underbrace{\begin{bmatrix} N^{AR^3} \\ \vdots \\ N^{AR^n} \end{bmatrix}}_{\boldsymbol{N}_{\boldsymbol{T}}^{(2)}} = \boldsymbol{A}_{\boldsymbol{red}}^{(2)} \tag{5.17}$$

The unconstrained value of $\boldsymbol{N}_{\boldsymbol{T}}^{(2)}$ using the LSA, $\boldsymbol{Er}$ and the SSE corresponding to each step is found following the steps taken and shown in Eq. (5.13) to Eq. (5.15) and the resultant value that then gives a minimum value of the SSE is selected as the optimal value of N^{AR^2}. Similarly, in calculating N^{AR^3}, N^{AR^1} and $N^{AR^2}$are kept equal to the optimal values found from the previous step. Likewise, after calculating all the values of $\boldsymbol{N}$, i.e. N^{AR^1} to N^{AR^n}, the final resultant (fitted) curve is obtained by post multiplying it by $\boldsymbol{A}$, as per Eq. (5.8).

In order to determine the effect of the solvent on the process, the fitted curve for ε_m taking values from 1.77 to 2.3 with a step size of 0.05 is generated following the above procedure. The error and SSE values determined from the experimental and the fitted curve ($\boldsymbol{Er} = \boldsymbol{A}_{\boldsymbol{exp}} - \boldsymbol{A}_{\boldsymbol{fitted}}$; $SSE = \boldsymbol{Er}'\boldsymbol{Er}$) are calculated for all the step values of ε_m and among them, the value of ε_m giving the minimum SSE is selected to generate the final fitted curve. The value of $\boldsymbol{N}$ corresponding to the final fitted curve is taken as the contribution of the individual ARs.

The algorithm was coded in MATLAB [301] and the source-code is provided in the Appendix 2.

5.3 Methodology

5.3.1 Chemicals

The following chemicals used in the synthesis of GNRs were purchased from Aldrich: Cetyltrimethylammonium Bromide (CTAB; $C_{19}H_{42}NBr$; 99%), Chloroauric acid ($HAuCl_4.3H_2O$; 99.9%), Sodium borohydride ($NaBH_4$, 99%), Silver nitride ($AgNO_3$; 99+%), Ascorbic acid ($C_6H_8O_6$, 99+%).

5.3.2 Chemical synthesis

GNRs were synthesized by using the seed-mediated used previously at City, University of London and reported by Jie Cao *et al.* [273]. In brief, the seed solution was prepared by reducing a solution containing 5 mL of 0.2 M CTAB and 5 mL of 0.5 mM $HAuCl_4 \cdot 3H_2O$ with 600 µL of 0.01 M ice-cold $NaBH_4$. After stirring the solution for an additional 2 minutes at 900 rpm, the seed solution was left undisturbed for 3 hours.

The growth solution was prepared by mixing a known amount of 20 mM $AgNO_3$ solution, 30 mL of 0.2 M CTAB solution and 30 mL of 1 mM $HAuCl_4 \cdot 3H_2O$ in the same sequence. To the mixed solution, 420 µL of 0.0788 M ascorbic acid solution was added, while stirring at 350 rpm. This step will change the colour of solution from bright yellow to colourless. Further, 100 µL of seed solution was added to the growth solution and the resulting solution was left undisturbed for 12 hours. Since CTAB is insoluble in deionized (DI) water at room temperature, all the synthesis steps were performed in a water bath maintained at a constant temperature of 301 K.

The excess of CTAB present in the GNR solution was removed by using two rounds of centrifugation at 3700g for 20 minutes for each round. After each round, the supernatant was decanted and the GNRs deposited at the bottom of the centrifuge tube were re-dispersed in the same quantity of DI water. The role of different chemicals used in synthesis of GNRs is given in Appendix 3.

5.3.3 Characterization

The absorption spectra of the GNRs solutions were measured by using a LAMBDA 35 UV-Vis spectrometer (Perkin Elmer Inc.) monitoring over the wavelength range from 400 nm to 1000 nm, in steps of 1 nm. The TEM images were taken from JEOL at accelerating voltages of 80kV and yielding 400k magnification. The dimensions of the GNRs from the TEM images were measure using ImageJ, which is an open source image processing software inspired by NIH image [302]. The DLS measurement was performed using a ZetaSizer Nano ZEN 3600 (Malvern Instruments).

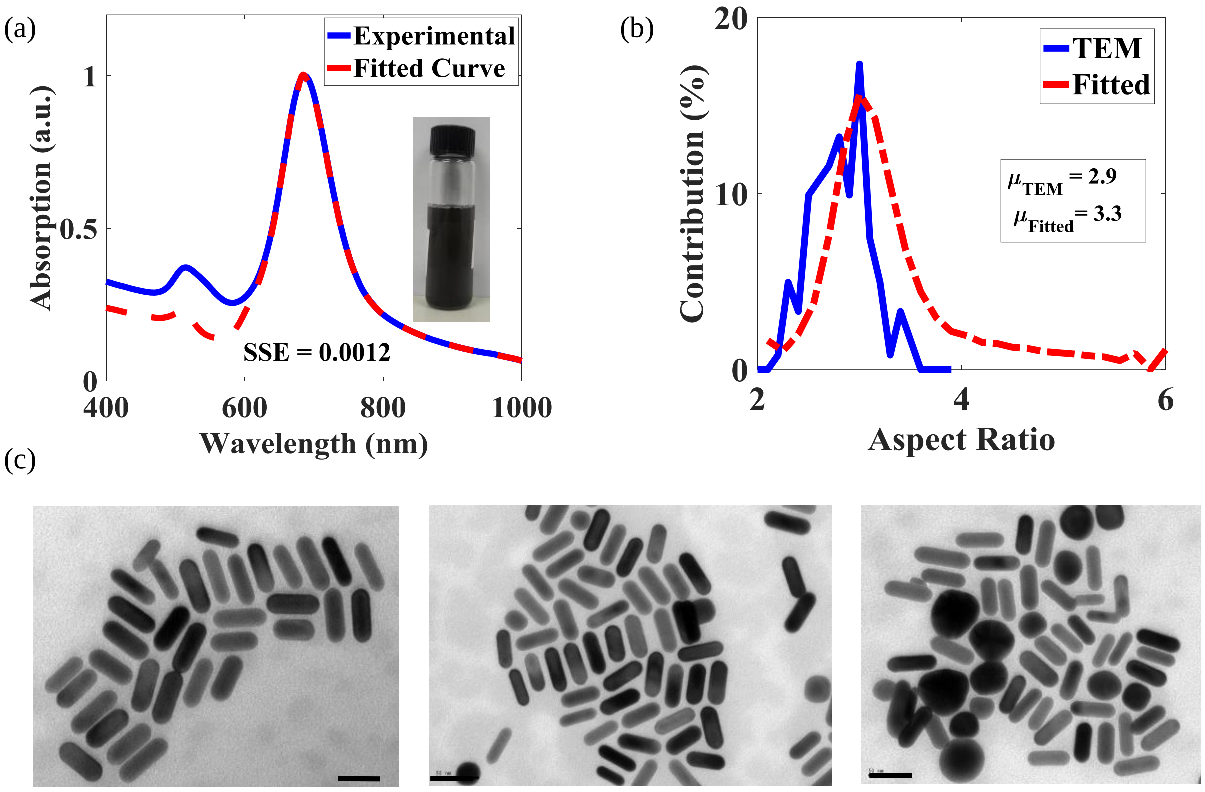

Figure 5. 2: (a) The UV-Vis absorption spectrum of the chemically synthesized sample (solid line) and the spectrum obtained by fitting the longitudinal resonance (dash line). Inset is shown a photograph of the GNRs solution (b) AR distributions curve obtained through the measurement with the TEM images measurement (solid line) and fitting of the UV-Vis spectrum (dashed line). The legend shows the mean value for both graphs. (c) TEM images taken at three different places on the TEM grid. The scale bar represents 50 nm.

5.4 Results and discussions

5.4.1 Comparison with TEM measurement

The experimental validation of the algorithm developed was performed by comparing the AR distribution obtained from the use of the algorithm with that obtained by manually measuring 121 GNRs from TEM images captured at three different places on the TEM grid. Figure 5.2(a) shows an experimentally-obtained UV-Vis spectrum and the absorption spectrum obtained by fitting an experimental data points in the L-LSPR region. As it can be seen from the figure, both graphs match well (SSE = 0.0012) in the LSPR region. Further, a picture of the actual synthesized colloidal solution is shown in the inset. The black color of the solution indicates the presence of a low number of GNPs. Figure 5.2(b) shows the distribution of the ARs obtained by measuring GNRs from TEM images and those obtained from the use of algorithm whereas, Fig. 5.2(c) shows the corresponding TEM images used for the ARs measurements. It can be seen in Fig. 5.2(b) that, the algorithm used correctly predicted the most probable AR, the value of which is 3. However, the overall AR distribution obtained from the TEM images is shifted towards lower ARs and consequently, the mean value of the distribution obtained by the use of TEM is lower than that of the obtained from developed algorithm (μ_{TEM}= 2.9; μ_{Fitted}= 3.3). This mismatch is due to the inability of the TEM to examine the macroscopic volume in comparison to using L-LSPR region of UV-Vis spectrum, which is very much sensitive to the macroscopic ARs distribution seen in the colloidal solution. To corroborate the above claim, the UV-Vis spectrum was reconstructed by substituting the contribution obtained from TEM measurement in Eq. (5.8), matching it with the experimentally obtained UV-Vis spectrum. As shown in Fig. 5.3(a), UV-Vis spectrum retrieved using the TEM measurements deviates significantly from the experimental UV-Vis spectrum SSE_{TEM} = 17.4839 is much larger than the value obtained from the algorithm $SSE_{algorithm}$ = 0.0012). It is important to note that due to the growth kinematics of seed-based synthesis, an AR cannot have a limitless combination of length and width, because of the same average volume of GNRs for a given colloidal solution. Therefore, any increase in the AR is caused by an increase in length and a correlated decrease in the width, as can be seen from the TEM measurements of the GNRs described in Fig. 5.3(b).

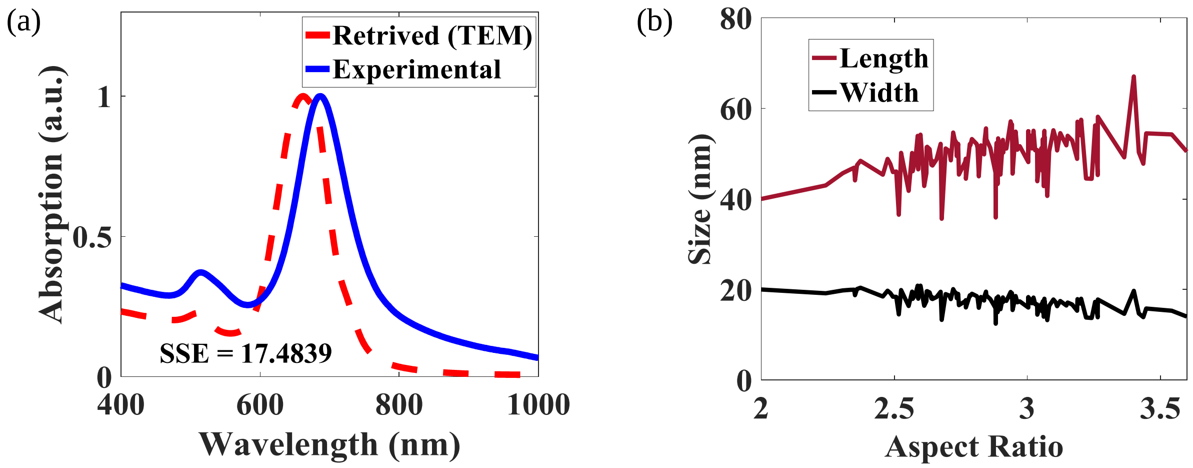

Figure 5. 3: (a) The UV-Vis absorption spectrum of the chemically synthesized sample (solid line) compared with spectrum retrieved from AR distribution obtained from TEM measurement (dashed line). (b) Dependence of length and width of GNRs on AR obtained from TEM measurement.

The inability to obtain a statistically accurate AR distribution from the TEM measurement was also reported by Eustis & Sayed [298] for 5 different samples, showing longitudinal resonance around 630 nm, 700 nm, 850 nm, 900 nm & 1000 nm. In this work, these UV-Vis spectra have been reconstructed after extracting data using a Webplot digitizer [303], followed by the use of the algorithm developed to calculate the AR distribution. Figure 5.4 (a) shows the reconstructed UV-Vis spectra and Fig. 5.4(b)-(e) show the comparison of AR distribution obtained from the developed algorithm and previously reported by Eustis & Sayed [298]. As it can be seen from figure, there is good agreement between the present and previously obtained AR distributions. This further validate the reliability of the developed algorithm.

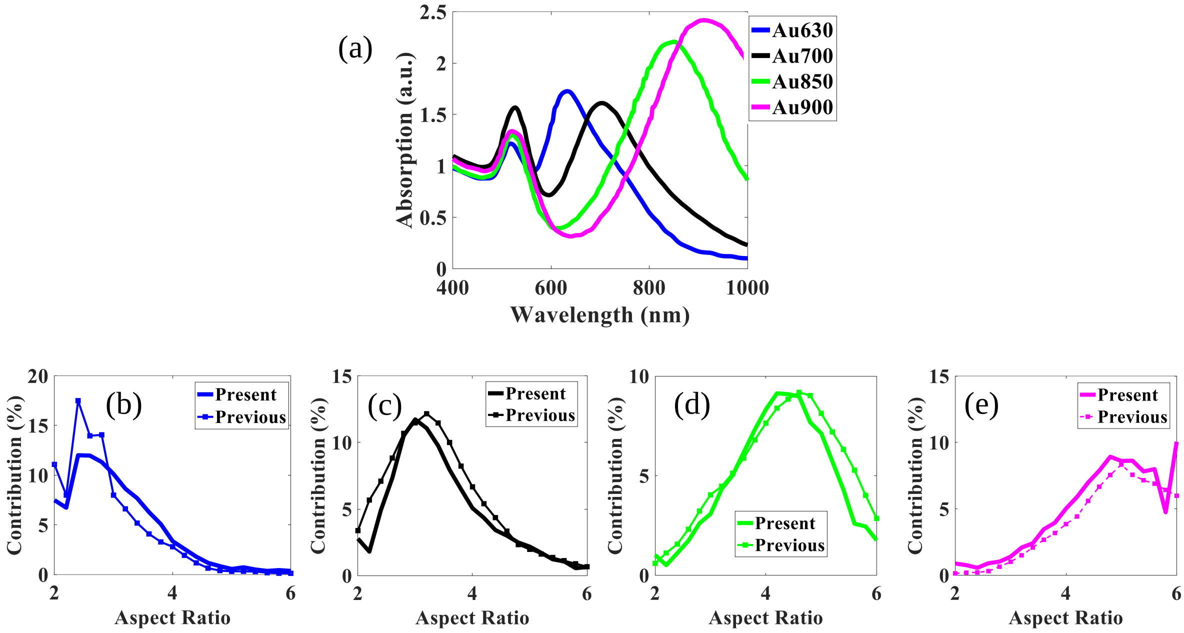

Figure 5. 4: (a) The UV-visible spectra extracted from the work of Eustin & Sayed [298] *. (b)-(e) Comparison of AR distribution obtained from the algorithm developed in present work with the one reported in the same publication.*

5.4.2 Comparison with DLS measurement

The size distribution of the chemically synthesized sample obtained from DLS measurement is shown in Fig. 5.5(a). It can be seen from the graph that the DLS measurement reports two peaks centred around 2.544 nm and 69.94 nm. The first peak can be attributed to seed GNPs which could not grow due to insufficient amount of gold in the growth solution, whereas second peak accounts for fully developed GNRs and GNPs. Since DLS gives the size distribution with respect to the hydrodynamic radius, i.e. the radius of an equivalent sphere having same diffusion coefficient, it is difficult to obtain the AR distribution from the graph shown, especially when spherical and cubic gold impurities are present in the colloidal solution. For example, few spherical GNPs impurities can be seen in right-hand TEM image, shown in Fig. 5.2(c). The inability of DLS to distinguish shape makes it unsuitable to measure the AR distribution. In contrast to the DLS measurement, the algorithm developed here is unaffected by the presence of large spherical GNPs impurities, because they do not exhibit a L-LSPR.

The algorithm developed was further benchmarked with the results of a numerical technique, as described in the next subsection, to circumvent the limitations discussed above and associated with the TEM and DLS measurements.

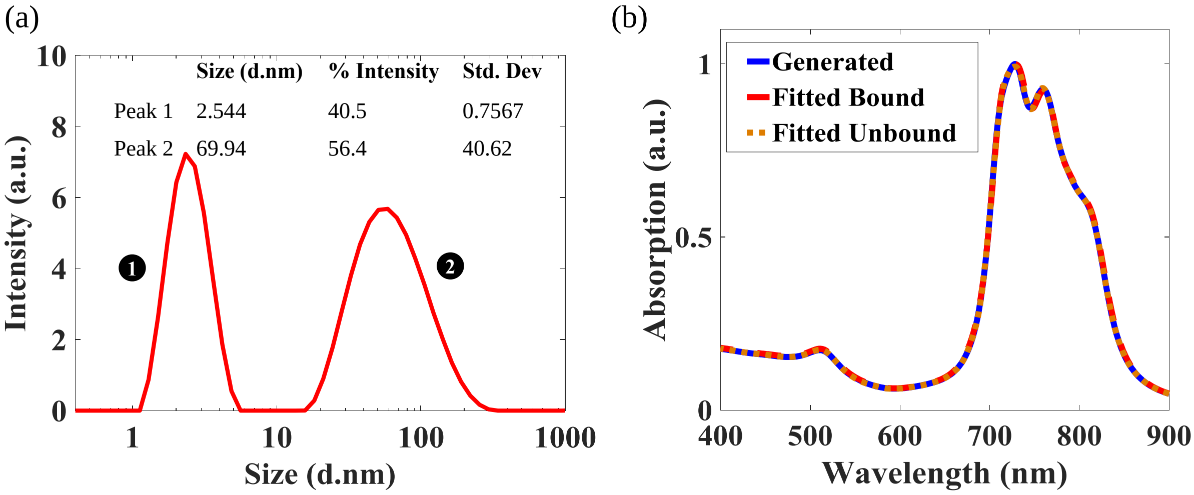

Figure 5. 5: (a) Size Distribution of chemically synthesized GNRs obtained by using the DLS technique (b) Quality of the fitting of the Absorption spectra generated by the test program, obtained by fitting the generated curve with the bounded and the unbounded coefficients.

5.4.3 Theoretical Benchmarking of the algorithm

For the most effective theoretical benchmarking of the algorithm developed, the absorption spectrum, resembling that of a chemically synthesized poly-dispersed colloidal solution, was generated numerically from the combination of 11 GNRs samples having AR values ranging between 3 and 4 (with a regular interval of 0.1), using Eq. (5.8). In Eq. (5.8), ***N*** was randomly generated by the use of an in-built random function generator on MATLAB and ***A*** was generated from Eq. (5.6) over the wavelength range from 400 to 900 nm, with a step size of 1 nm, at ε_m= 2.1.

The spectrum generated was input to the algorithm developed to retrieve the value of ε_m and the corresponding (bounded) values of ***N***. Further, to validate the point mentioned in the previous section i.e. solving the over-determined set of linear equations without any constrain may result in non-physical values, the LSA technique was used to obtain the unbounded values of ***N***. Both the unbounded and bounded values of ***N*** were cross compared with the known input (randomly generated) values of ***N*** to determine the accuracy of the methods used. Figure 5.5(b) shows the generated and retrieved absorption spectra. It can be seen from this that all three spectra, i.e. the generated spectrum and the spectra obtained using the developed algorithm and LSA match very closely at ε_m = 2.12. The value of ε_m= 2.12 was obtained by analyzing the variation of the values of the SSE with respect to ε_m, as shown in Fig. 5.6(a). The minimum SSE value was obtained at ε_m = 2.12 (and this is shown in the inset). It matches very well with the value of ε_m = 2.1 used for generating the input spectrum.

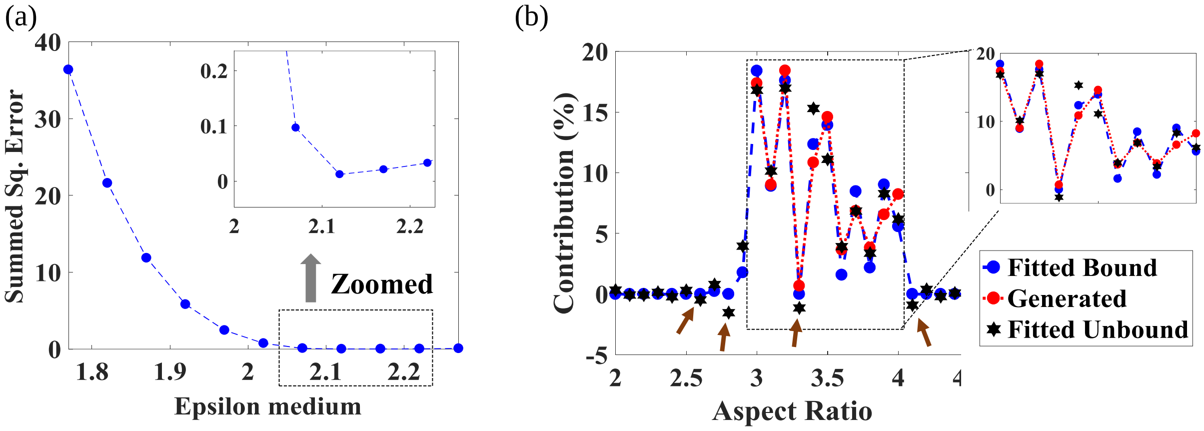

Figure 5. 6: (a) Fitted SSE as function of ε_m for the bounded coefficients. Inset shows the obtained minimum SSE for ε_m = 2.12. (b) Left: the figure compares the generated (test) AR contribution with that generated by the algorithm for the bounded and unbounded coefficients. Right: 'Zooming in' on the 3 ≤ AR ≤ 4 region from the main (Left) figure.

Figure 5.6(b) shows the input and retrieved values (i.e. the contribution), of ***N***, represented as a percentage, for different values of AR. The blue solid spheres show the value of the contribution obtained from the developed (bounded) algorithm. It can be seen from the figure that, outside the input regime i.e. AR < 3 & AR > 4, the developed algorithm correctly predicted the absence of any GNRs (i.e. a zero contribution) whereas for 3 ≤ AR ≤ 4, the values obtained from the algorithm are in good agreement with the input values (represented by the red solid spheres), as shown in zoomed right-hand figure and in Table 5.1. However, if the contributions obtained from the LSE is considered (shown by black stars in the main and the zoomed figure), it gives a negatives contribution for some values of the AR, as indicated by brown arrows in Fig. 5.6(b). Moreover, as given in Table 5.1, the SSE obtained from the Fitted Bound is much lower than the SSE obtained from Fitted Unbound situation (SSE_{bound}= 1.83; $SSE_{unbound}$ = 7.59). This result shows that the algorithm which has been developed is capable of correctly retrieving the contribution from the UV-Vis absorption spectrum of the poly-dispersed colloidal solution.

Table 5. 1 AR and corresponding contribution obtained from Generated, Fitted Bound, & Fitted Unbound techniques.

AR	Generated	Fitted Bound	Error	Fitted Unbound	Error
3	17.17	18.39	0.06	16.8	-0.03
3.1	9.01	8.9	-0.01	10.14	0.13
3.2	18.41	17.6	-0.04	16.98	-0.08
3.3	0.68	0	-1	-1.14	-2.68
3.4	10.84	12.34	0.14	15.30	0.41
3.5	14.59	13.92	-0.05	11.11	-0.23
3.6	3.65	1.58	-0.57	3.92	0.07
3.7	6.85	8.47	0.24	6.85	-4.00E-04
3.8	3.82	2.18	-0.43	3.38	-0.117
3.9	6.55	9.02	0.38	8.28	0.26
4	8.22	5.59	-0.32	6.18	-0.25
		SSE	1.83		7.59

5.4.4 Application on additional synthesized samples

After benchmarking, the bounded technique was used to determine the AR distributions in two further chemically synthesized samples having different AR. These two chemically synthesized samples were obtained by varying the amount of $AgNO_3$ added to growth solution because the silver ions present in $AgNO_3$ combine with Br^{2-} to form AgBr in the presence of CTAB and absorbs differentially to the facets of gold particles, thus promoting 1-D growth.

Figure 5.7(a) shows the L-LSPR fitting used in the case of a sample having well-separated L-LSPR and T-LSPR peaks. As can be seen from the figure, in the L-LSPR regime i.e. where the wavelength is ≥ 615 nm, the fitted curve matches closely the experimentally obtained absorption spectrum (SSE = 0.0086). Since, only the L-LSPR is used to obtain the contribution (as a percentage) of the individual ARs, extending the fitted spectrum to the T-LSPR spectral region (which is less than the wavelength of 615 nm) will give the ideal spectrum, i.e. the spectrum obtained in the absence of the GNPs ($1 \leq AR < 2$). Therefore, the mismatch in the T-LSPR regime between the fitted and the experimental curves can be used to visualize quantitatively the magnitude of the GNPs present in the colloidal solution, as shown as the dotted region in Fig. 5.7(a). This can be described as, in the absence of any GNPs, the experimental and the fitted curves would be matched closely around the T-LSPR as well. From the mismatch at the T-LSPR in Fig. 5.7(a), it can be concluded that a significant number of GNPs are present in the solution. Figure 5.7(b) shows the contribution (again as a percentage) of the AR present, where the calculated mean (μ) AR of the solution is 4, with a standard deviation (σ) of 0.8.

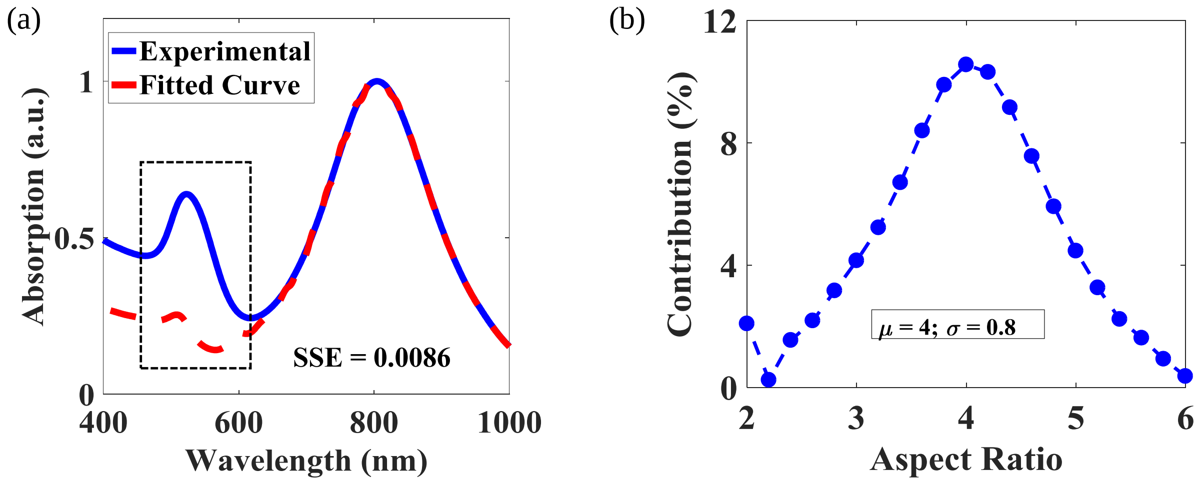

Figure 5. 7: (a) The absorption spectra of chemically synthesized sample (solid line), juxtaposed with the spectra obtained by fitting the longitudinal resonance (dashed line). The dotted section highlights the mismatch around transverse resonance. (b) AR distributions curve. The legend shows mean value and standard deviation. For both graphs, $\varepsilon_m = 1.92$ *was used.*

Figure 5.8(a) shows the quality of the curve fitting in the case of a solution where the T-LSPR and the L-LSPR cannot readily be distinguished. It can be seen that for a wavelength ≥ 615 nm, the theoretical curve fits well to the experimentally obtained spectrum. The mismatch between the fitted and the experimental curves around the T-LSPR, as illustrated by the dotted section on the graph, shows the presence of the GNPs. Figure 5.8(b) shows the AR contributions and, as expected, by comparison to an analysis of the previous colloidal solution, this solution has an abundance of less elongated GNRs ($\mu = 2.8$; $\sigma = 0.4$) and the amount of GNRs seen with an AR value greater than 4.2 is almost zero.

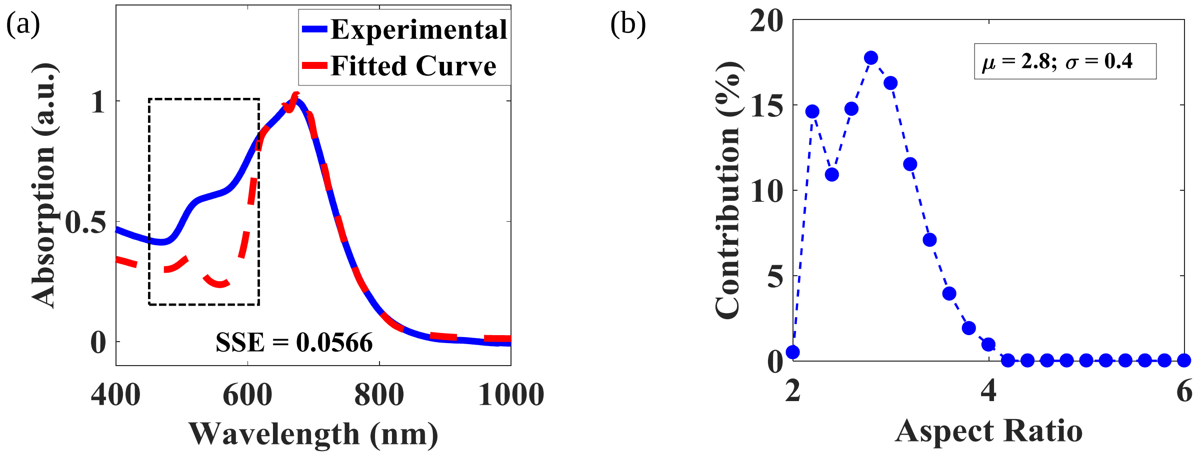

Figure 5. 8: (a) Measured (solid line) and fitted (dashed line) absorption spectra, for a low AR sample. Dotted section qualitatively highlights the number of particles having AR ≤ 2. (b) Contribution of various AR values to obtain the fitted curve in (a). The SSE was a minimum for $\varepsilon_m = 1.97$.

5.5 Summary

The research carried out and reported in this Chapter has shown that the algorithm developed in this paper using Bellman's dynamic technique was an effective approach for the rapid determination of the AR distribution of a synthesized GNRs colloidal solution by theoretically fitting the L-LSPR regime of the absorption spectrum. The developed algorithm, after numerical and experimental benchmarking, was applied additionally to two in-house synthesized solutions to determine the mean and standard deviations of the ARs. This technique has been shown to give both a cost-effective and rapid way to determine the quality of the synthesized solution as it avoids the need for more expensive TEM analysis of all of the samples synthesized.

Chapter 6

Summary and Future work

6.1 Summary of the work

The major objectives of the work, set out in Chapter 1, were achieved and several publications in high impact international journals were produced as a result.

The achievements of the research project, with reference to the objectives set out in Chapter 1 can be summarized as:

- In the beginning, the review of nanoparticles, their synthesis processes and important characterization techniques was conducted by analyzing data from several relevant published papers and book chapters. After the review, among the nanoparticles considered, rare-earth doped upconverting nanoparticles (UCNPs), due to their unique properties of having thermally coupled radiative energy levels, were selected for further exploration as the basis of the sensor head for luminescent temperature detection. However, the difficulty in modifying the UCNPs suitably for the development of heavy metals detection led to an investigation of gold nanoparticles as an alternative. A detailed review of the underlying principles of upconversion, the roles of dopants, the innovative ways to improve fluorescence and selected interesting applications reported in last 10 years have been delineated in Chapter 2. Moreover, in the last section of that chapter, the brief fundamentals of Localized Surface Plasmon Resonance (LSPR) pertaining to nanoparticles synthesized from gold have been considered.
- After completing the literature review and finalizing the work on UCNPs for the development of portable optical fibre-based temperature sensors, the ~56 nm hexagonal phased UCNPs ($NaYF_4$: (18%) Yb^{3+}; (2%) Er^{3+}) were synthesized using the solvothermal method. Subsequently, the colloidal solution of the synthesized UCNPs was mixed with PDMS in an appropriate ratio to obtain a UCNPs-PDMS composite and this was dip coated on the tip of multimode optical fibre to realise a reflection based optical sensor. The ratio of the thermally coupled emission of the green bands (centred around 525 nm and 545 nm) shows a linear response in useful range of 295 K to 473 K with, the sensitivity of (2.90 ±

0.40) $\times 10^{-3}$ K^{-1} and response time of ∼ 5 seconds. The UNCPs powder-based sensor, developed for cross-comparison, showed a higher sensitivity (4.91 ± 0.02) $\times 10^{-3}$ K^{-1} but showed a lesser mechanical stability over time. The obtained sensitivity of the developed powder and composite based sensors were of the same order as previously reported for several Er^{3+}/Yb^{3+} doped glass-based sensors but the advantages of the developed sensors lies in their portability and involved synthesis processes, which can be achieved with the instruments found in the chemistry laboratory available to me.

- For the development of the GNPs based heavy metal detection sensor, the colloidal solution was synthesized and coated onto the optical fibre. The selectivity of the coated GNPs towards heavy metal detection was achieved by modifying the surface with MUA and tested for various concentration of Pb^{2+} ions present in the aqueous solution. The LSPR wavelength shifted from 551.7 nm to 578.9 nm on varying the concentration of Pb^{2+} from 0 to 100 mM with a constant sensitivity of 0.28 nm/mM. This work has established the principle of creating a heavy metal sensor of this type by using such a coated optical fibre design.
- Several colloidal solutions of GNRs were chemically synthesized and their quality was determined by developing an algorithm to determine the AR distribution present by theoretically fitting the normalized broadened L-LSPR region ($\lambda \geq 615$ nm) of the UV-Vis spectrum. This fitting was carried out by first determining the individual L-LSPR spectrum for given AR (for $2 \leq AR \leq 6$), assuming uniform distribution using Gans' Model and then finding their amplitude (showing contribution) using the Bellman Principle of Optimality. The developed algorithm was benchmark with previously published results and cross-verified with the results by DLS and TEM. The obtained results show that the developed algorithm can be used as a cost-effective and rapid way to determine the quality of the synthesized solution specifically needed for many potential applications for the advanced sensor systems.
- The positive research outcomes achieved in this work have been widely disseminated via four peer reviewed journal publications and four international conference papers.

Thus, this provides the evidence, from the above points that the aims and objectives set out in Chapter 1 have been addressed to a large extent.

6.2 Proposal for future works

While working on the development of portable upconverting and gold nanoparticles based optical fibre sensors and an algorithm to determine AR of GNRs, the following ideas have been developed, which it is considered are worth pursuing in the future:

- The developed UCNPs-PDMS composite coated optical fibre sensor can only measure temperature at discrete points, however this work can be further extended to obtain a simultaneous thermal map of a large area. It can be achieved by first spin-coating the UCNPs-PDMS composite to create a uniform layer over the large area and then using colorimetric image detection technique instead of a more expensive spectrometer. This colorimetric image detection is feasible because out of three bands of Er^{3+} visible emissions i.e. those centred around 525 nm, 545 nm and 665 nm, where the only band around 545 nm shows considerable change in the intensity, thus causing discernible colour change.
- The UCNPs-PDMS composite showed a linear response (a desired quality for any sensor) in the temperature range of 295 K to 473 K. The linear response was attributed to an increase in non-radiative losses due to vibrational energy of the C-H stretching of PDMS and cannot model using existing Boltzmann's equation (ref. Eq. 3.1). Therefore, the development of a suitable model taking into account non-radiative losses which fits the experimental data very well would give more details about underlying processes and other related parameters.
- The developed UCNPs-PDMS composite and powder-based temperature sensor shows sensitivity comparable to several previously reported Yb^{3+}/Er^{3+} doped glass-based temperature sensors (ref. Table 3.2). It would thus be interesting to know the effect of PDMS on the response and sensitivity of core-shell UCNPs, plasmon enhanced nanoparticles and ratio of PDMS to UCNPs and this would be a fruitful area of exploration. Moreover, using silver reflective paint at the tip of UCNPs-PDMS composite based optical fibre sensor increased the upconversion intensity by ~23% (ref. Fig. 3.13(b)), which ideally could be optimized to increase the amount of luminescence reflected back. This low increase may be due to increase in scattering by the particle-based silver paint and hence reflection can be further enhanced by using smooth thinner film. The use of Tollens' regent for depositing thin film of silver would be a good option to explore [304]. An improvement in the reflection will enable use a cheaper, lower power laser source.
- The work has demonstrated the establishment of the principle of creating a portable heavy metal sensor by MUA functionalized GNPs needs to be extended for optimization in the synthesis processes such as the gold nanoparticle size and the MUA concentration to bring

its sensitivity further down from millimole range. Furthermore, investigation of the sensitivity of such sensors in different heavy metals is needed to determine the optimum performance of the sensor.

- In the current work, MUA has been used as linker to attach heavy metal ions to GNP's surface. However, there are several other linkers reported in literate such as pyrazinium thioacetate for detecting Pd^{2+} [305], chitosan for detecting Zn^{2+} and Cu^{2+} [306], Thiol-tagged DNA for all heavy metals [307], polyvinyl pyrrolidone for Hg^{2+} [263] and peptide molecules for detecting Cd^{2+} [308]. It would be nice to explore these linkers as an alternative to MUA along with the proper immobilization techniques to functionalize them on the surface of GNPs.
- The developed MUA functionalized GNPs sensor shows no spectral change in LN solutions; hence, it has to take out of the solution and dry it to observe a noticeable LSPR shift. It would be interesting to explore the exact reason behind this behaviour by studying the role of various coating parameters such as thickness and coverage area of GNPs on the optical fibre.
- The developed algorithm has shown to successfully to determine the AR in colloidal solution, but it is limited only to asymmetrical GNRs i.e. $2 \leq \mathrm{AR} \leq 6$. However, in the bottom-up synthesis of GNRs, there is always a presence of symmetrical GNPs ($\mathrm{AR} < 2$). In the current algorithm, the amount of GNPs is determined qualitatively by visualizing the mismatch in the T-LSPR regime between the fitted and the experimental curves because the quantitively determination of the variation of GNPs is challenging due to the dependence of their absorbance on several parameters [309]. In this regard, other techniques like "Machine learning" can be explored as an alternative solution. It will be valuable to have a single algorithm which can perform complete quantitative analysis of a given colloidal solution.

The above suggested directions show that the exploration of UNCPs and gold nanoparticles as novel sensor-heads will be a promising area of research for several years to come.

References

[1] Ulf Leonhardt, Invisibility Cup, Nat. Photonics. 1 (2007) 207–208. www.nature.com/naturephotonics.

[2] J. KUNCKEL, Ars vitraria experimentalis oder Vollkommene Glasmacherkunst, Frankfurt, 1689.

[3] Michael Faraday, 1997X. The Bakerian Lecture. —Experimental relations of gold (and other metals) to light, Phil. Trans. R. Soc. 47 (1857) 145–181. https://doi.org/https://doi.org/10.1098/rstl.1857.0011.

[4] A.G. Shard, V.D. Hodoroaba, W.E.S. Unger, Characterization of Nanoparticles: Measurement Processes for Nanoparticles, Elsevier, 2019. https://doi.org/10.1016/B978-0-12-814182-3.00001-8.

[5] T.Y. Masuo Hosokawa, Kiyoshi Nogi, Makio Naito, ed., Nanoparticle Technology Handbook, 2nd ed., Elsevier, 2012.

[6] Sensor Market Size And Forecast, Verif. Mark. Res. (2018) 108. https://www.verifiedmarketresearch.com/product/global-sensor-market-size-and-forecast-to-2025/ (accessed March 6, 2020).

[7] Y.H. Ghallab, Y. Ismail, CMOS Circuits and Systems for Lab-on-a-Chip Applications, in: Lab-on-a-Chip Fabr. Appl., InTech, 2016. https://doi.org/10.5772/63303.

[8] S. Ziegler, R.C. Woodward, H.H.C. Iu, L.J. Borle, Current sensing techniques: A review, IEEE Sens. J. 9 (2009) 354–376. https://doi.org/10.1109/JSEN.2009.2013914.

[9] Grattan K T V, Augousti A T, eds., Sensors VI: Technology, Systems, and Applications, Adam Hilger, London, 1991.

[10] K.O. Hill, Y. Fujii, D.C. Johnson, B.S. Kawasaki, Photosensitivity in optical fiber waveguides: Application to reflection filter fabrication, Appl. Phys. Lett. 32 (1978) 647–649. https://doi.org/10.1063/1.89881.

[11] A. Ghatak, K. Thyagarajan, An Introduction to Fiber Optics, Cambridge University

Press, 1998. https://doi.org/https://doi.org/10.1017/CBO9781139174770.

[12] K.T. V Grattan, T. Sun, Fiber optic sensor technology: an overview, 2000. www.elsevier.nlrlocatersna.

[13] M. Haase, H. Schäfer, Upconverting nanoparticles, Angew. Chemie - Int. Ed. 50 (2011) 5808–5829. https://doi.org/10.1002/anie.201005159.

[14] S. Hao, G. Chen, C. Yang, Sensing using rare-earth-doped upconversion nano-particles, Theranostics. 3 (2013) 331–345. https://doi.org/10.7150/thno.5305.

[15] X.D. Wang, O.S. Wolfbeis, R.J. Meier, Luminescent probes and sensors for temperature, Chem. Soc. Rev. 42 (2013) 7834–7869. https://doi.org/10.1039/c3cs60102a.

[16] S.Y. Njati, M.M. Maguta, Lead-based paints and children’s PVC toys are potential sources of domestic lead poisoning – A review, Environ. Pollut. 249 (2019) 1091–1105. https://doi.org/10.1016/j.envpol.2019.03.062.

[17] U. Bawa, A. Bukar, Y. Abdullahi, A Review of Lead Poisoning, Sources and Adverse Effects, ATBU J. Sci. Technol. Educ. 3 (2015) 71–79.

[18] A. Nicolli, G.G. Mina, D. De Nuzzo, I. Bortoletti, A. Gambalunga, A. Martinelli, F. Pasqualato, M. Cacciavillani, M. Carrieri, A. Trevisan, Unusual domestic source of lead poisoning, Int. J. Environ. Res. Public Health. 17 (2020) 1–7. https://doi.org/10.3390/ijerph17124374.

[19] B. Nikoobakht, Z.L. Wang, M.A. El-Sayed, Self-Assembly of Gold Nanorods, J. Phys. Chem. B. 104 (2000) 8635–8640. https://doi.org/10.1021/jp001287p.

[20] A.K. Singh, Introduction to Nanoparticles and Nanotoxicology, in: Eng. Nanoparticles, 2016: pp. 1–18. https://doi.org/10.1016/b978-0-12-801406-6.00001-7.

[21] D. Bera, L. Qian, T.-K. Tseng, P.H. Holloway, Quantum Dots and Their Multimodal Applications: A Review, Materials (Basel). 3 (2010) 2260–2345. https://doi.org/10.3390/ma3042260.

[22] S.M. Reimann, M. Manninen, Electronic structure of quantum dots, Rev. Mod. Phys. 74 (2002) 1283–1342. https://doi.org/10.1103/RevModPhys.74.1283.

[23] B. Ballou, B.C. Lagerholm, L.A. Ernst, M.P. Bruchez, A.S. Waggoner, Noninvasive

imaging of quantum dots in mice, Bioconjug. Chem. 15 (2004) 79–86.

[24] J. Wu, Y.F.M. Makableh, R. Vasan, M.O. Manasreh, B. Liang, C.J. Reyner, D.L. Huffaker, Strong interband transitions in InAs quantum dots solar cell, Appl. Phys. Lett. 100 (2012) 51907.

[25] H. Shen, W. Cao, N.T. Shewmon, C. Yang, L.S. Li, J. Xue, High-Efficiency, Low Turn-on Voltage Blue-Violet Quantum-Dot-Based Light-Emitting Diodes, Nano Lett. 15 (2015) 1211–1216. https://doi.org/10.1021/nl504328f.

[26] S. Coe-Sullivan, Optoelectronics: Quantum dot developments, Nat. Photonics. 3 (2009) 315–316. https://doi.org/10.1038/nphoton.2009.83.

[27] V.I. Klimov, S.A. Ivanov, J. Nanda, M. Achermann, I. Bezel, J.A. McGuire, A. Piryatinski, Single-exciton optical gain in semiconductor nanocrystals, Nature. 447 (2007) 441–446.

[28] C. Wang, B.L. Wehrenberg, C.Y. Woo, P. Guyot-Sionnest, Light emission and amplification in charged CdSe quantum dots, J. Phys. Chem. B. 108 (2004) 9027–9031.

[29] S. Nikazar, V.S. Sivasankarapillai, A. Rahdar, S. Gasmi, P.S. Anumol, M.S. Shanavas, Revisiting the cytotoxicity of quantum dots: an in-depth overview, Biophys. Rev. (2020) 1–16.

[30] Quantum Dots, (n.d.). https://www.sigmaaldrich.com/technical-documents/articles/materials-science/nanomaterials/quantum-dots.html.

[31] Quantum Dots: The Basics, (n.d.). https://www.findlight.net/blog/2018/08/02/quantum-dots-basics/ (accessed June 10, 2020).

[32] S. Szunerits, R. Boukherroub, Sensing using localised surface plasmon resonance sensors, Chem. Commun. 48 (2012) 8999–9010.

[33] T. Jiang, J. Song, W. Zhang, H. Wang, X. Li, R. Xia, L. Zhu, X. Xu, Au–Ag@ Au hollow nanostructure with enhanced chemical stability and improved photothermal transduction efficiency for cancer treatment, ACS Appl. Mater. Interfaces. 7 (2015) 21985–21994.

[34] A.M. Gobin, M.H. Lee, N.J. Halas, W.D. James, R.A. Drezek, J.L. West, Near-infrared resonant nanoshells for combined optical imaging and photothermal cancer therapy,

Nano Lett. 7 (2007) 1929–1934.

[35] Y. Zhang, P. Yang, M.A. Habeeb Muhammed, S.K. Alsaiari, B. Moosa, A. Almalik, A. Kumar, E. Ringe, N.M. Khashab, Tunable and linker free nanogaps in core–shell plasmonic nanorods for selective and quantitative detection of circulating tumor cells by SERS, ACS Appl. Mater. Interfaces. 9 (2017) 37597–37605.

[36] S.A. Maier, P.G. Kik, H.A. Atwater, S. Meltzer, E. Harel, B.E. Koel, A.A.G. Requicha, Local detection of electromagnetic energy transport below the diffraction limit in metal nanoparticle plasmon waveguides, Nat. Mater. 2 (2003) 229–232.

[37] D.F. Swearer, H. Zhao, L. Zhou, C. Zhang, H. Robatjazi, J.M.P. Martirez, C.M. Krauter, S. Yazdi, M.J. McClain, E. Ringe, Heterometallic antenna− reactor complexes for photocatalysis, Proc. Natl. Acad. Sci. 113 (2016) 8916–8920.

[38] E. Ringe, Shapes, Plasmonic Properties and Reactivity of Magnesium Nanoparticles, J. Phys. Chem. C. (2020). https://doi.org/10.1021/acs.jpcc.0c03871.

[39] Z. Zhu, Q. Sun, Z. Zhang, J. Dai, G. Xing, S. Li, X. Huang, W. Huang, Metal halide perovskites: stability and sensing-ability, J. Mater. Chem. C. 6 (2018) 10121–10137.

[40] S. Bai, Z. Yuan, F. Gao, Colloidal metal halide perovskite nanocrystals: Synthesis, characterization, and applications, J. Mater. Chem. C. 4 (2016) 3898–3904. https://doi.org/10.1039/c5tc04116c.

[41] M.M. Lee, J. Teuscher, T. Miyasaka, T.N. Murakami, H.J. Snaith, Efficient hybrid solar cells based on meso-superstructured organometal halide perovskites, Science (80-.). 338 (2012) 643–647.

[42] A. Kojima, K. Teshima, Y. Shirai, T. Miyasaka, Organometal halide perovskites as visible-light sensitizers for photovoltaic cells, J. Am. Chem. Soc. 131 (2009) 6050–6051.

[43] M. Berger, What is MOF ?, (n.d.). https://www.nanowerk.com/mof-metal-organic-framework.php (accessed July 9, 2020).

[44] V. V Butova, M.A. Soldatov, A.A. Guda, K.A. Lomachenko, C. Lamberti, Metal-organic frameworks: structure, properties, methods of synthesis and characterization, Russ. Chem. Rev. 85 (2016) 280–307. https://doi.org/10.1070/rcr4554.

[45] X. Fang, B. Zong, S. Mao, Metal–Organic Framework-Based Sensors for Environmental Contaminant Sensing, Nano-Micro Lett. 10 (2018) 64. https://doi.org/10.1007/s40820-018-0218-0.

[46] H. Li, K. Wang, Y. Sun, C.T. Lollar, J. Li, H.-C. Zhou, Recent advances in gas storage and separation using metal–organic frameworks, Mater. Today. 21 (2018) 108–121.

[47] H. Bin Wu, X.W.D. Lou, Metal-organic frameworks and their derived materials for electrochemical energy storage and conversion: Promises and challenges, Sci. Adv. 3 (2017) eaap9252.

[48] F. Wang, X. Liu, Recent advances in the chemistry of lanthanide-doped upconversion nanocrystals, Chem. Soc. Rev. 38 (2009) 976–989.

[49] X. Chen, D. Peng, Q. Ju, F. Wang, Photon upconversion in core–shell nanoparticles, Chem. Soc. Rev. 44 (2015) 1318–1330.

[50] Y. Zhong, G. Tian, Z. Gu, Y. Yang, L. Gu, Y. Zhao, Y. Ma, J. Yao, Elimination of photon quenching by a transition layer to fabricate a quenching-shield sandwich structure for 800 nm excited upconversion luminescence of Nd3+-sensitized nanoparticles, Adv. Mater. 26 (2014) 2831–2837.

[51] A.V. Rane, K. Kanny, V.K. Abitha, S. Thomas, Methods for Synthesis of Nanoparticles and Fabrication of Nanocomposites, in: Synth. Inorg. Nanomater., Elsevier Ltd., 2018: pp. 121–139. https://doi.org/10.1016/b978-0-08-101975-7.00005-1.

[52] G.B. Nair, V.B. Pawade, S.J. Dhoble, White light-emitting novel nanophosphors for LED applications, Elsevier Inc., 2018. https://doi.org/10.1016/B978-0-12-813731-4.00013-8.

[53] Coprecipitation, (n.d.). https://en.wikipedia.org/wiki/Coprecipitation (accessed May 14, 2020).

[54] W. Niu, L. Zhang, G. Xu, Seed-mediated growth of noble metal nanocrystals: crystal growth and shape control, Nanoscale. 5 (2013) 3172–3181. https://doi.org/10.1039/C3NR00219E.

[55] C.J. Murphy, T.K. Sau, A.M. Gole, C.J. Orendorff, J. Gao, L. Gou, S.E. Hunyadi, T. Li, Anisotropic Metal Nanoparticles: Synthesis, Assembly, and Optical Applications, J. Phys. Chem. B. 109 (2005) 13857–13870. https://doi.org/10.1021/jp0516846.

[56] S.H. Feng, G.H. Li, Hydrothermal and Solvothermal Syntheses, in: Mod. Inorg. Synth. Chem. Second Ed., 2017: pp. 73–104. https://doi.org/10.1016/B978-0-444-63591-4.00004-5.

[57] X. Wang, J. Zhuang, Q. Peng, Y. Li, A general strategy for nanocrystal synthesis, Nature. 437 (2005) 121–124. https://doi.org/10.1038/nature03968.

[58] Y. Inouye, S. Kawata, Near-field scanning optical microscope with a metallic probe tip, Opt. Lett. 19 (1994) 159–161.

[59] M.F. Ashby, P.J. Ferreira, D.L. Schodek, Chapter 8 - Nanomaterials: Synthesis and Characterization, in: Nanomater. Nanotechnologies Des., 2009: pp. 257–290. https://doi.org/10.1201/9781315123950-1.

[60] A. Diaspro, Confocal and two-photon microscopy: foundations, applications, and advances, Wiley-Liss New York:, 2002.

[61] X. Zhou, G.E. Thompson, Electron and Photon Based Spatially Resolved Techniques, (2017).

[62] M. RÜHLE, M. WILKENS, CHAPTER 11 - TRANSMISSION ELECTRON MICROSCOPY, in: R.W. CAHN, P.B.T.-P.M. (Fourth E. HAASEN† (Eds.), Phys. Metall. (Fourth, Revis. Enhanc. Ed., North-Holland, Oxford, 1996: pp. 1033–1113. https://doi.org/https://doi.org/10.1016/B978-044489875-3/50016-8.

[63] W. Zhou, R. Apkarian, Z.L. Wang, D. Joy, Fundamentals of scanning electron microscopy (SEM), in: Scanning Microsc. Nanotechnol., Springer, 2006: pp. 1–40.

[64] S.L. Flegler, S.L. Flegler, Scanning & Transmission Electron Microscopy, Oxford University Press, 1997.

[65] A. V Crewe, J. Wall, L.M. Welter, A high-resolution scanning transmission electron microscope, J. Appl. Phys. 39 (1968) 5861–5868.

[66] B. Voigtländer, Vibrational Spectroscopy with the STM BT - Scanning Probe Microscopy: Atomic Force Microscopy and Scanning Tunneling Microscopy, in: B. Voigtländer (Ed.), Springer Berlin Heidelberg, Berlin, Heidelberg, 2015: pp. 335–340. https://doi.org/10.1007/978-3-662-45240-0_22.

[67] D. Rugar, P. Hansma, Atomic force microscopy, Phys. Today. 43 (1990) 23–30.

[68] A.J. d’Alfonso, B. Freitag, D. Klenov, L.J. Allen, Atomic-resolution chemical mapping using energy-dispersive x-ray spectroscopy, Phys. Rev. B. 81 (2010) 100101.

[69] J.L. Hart, A.C. Lang, A.C. Leff, P. Longo, C. Trevor, R.D. Twesten, M.L. Taheri, Direct Detection Electron Energy-Loss Spectroscopy: A Method to Push the Limits of Resolution and Sensitivity, Sci. Rep. 7 (2017) 8243. https://doi.org/10.1038/s41598-017-07709-4.

[70] B.C. Smith, Fundamentals of Fourier transform infrared spectroscopy, CRC press, 2011.

[71] H.H. Mantsch, D. Chapman, Infrared spectroscopy of biomolecules, Wiley-Liss New York, 1996.

[72] D.A. Long, Raman spectroscopy, 1977.

[73] H.W. Wyckoff, X-ray diffraction analysis of the structure of deoxyribonucleic acid, (1955).

[74] B.J. Berne, R. Pecora, Dynamic light scattering: with applications to chemistry, biology, and physics, Courier Corporation, 2000.

[75] X. Liu, C.-H. Yan, J.A. Capobianco, Photon upconversion nanomaterials, Chem. Soc. Rev. 44 (2015) 1299–1301.

[76] W. Zheng, P. Huang, D. Tu, E. Ma, H. Zhu, X. Chen, Lanthanide-doped upconversion nano-bioprobes: electronic structures, optical properties, and biodetection, Chem. Soc. Rev. Chem. Soc. Rev. 44 (2015) 1379–1415. www.rsc.org/chemsocrev (accessed September 30, 2017).

[77] N. Bloembergen, Solid state infrared quantum counters, Phys. Rev. Lett. 2 (1959) 84.

[78] F. Auzel, Upconversion and Anti-Stokes Processes with f and d Ions in Solids, Chem. Rev. 104 (2004) 139–173. https://doi.org/10.1021/cr020357g.

[79] B.M. Walsh, JUDD-OFELT THEORY: PRINCIPLES AND PRACTICES, in: Adv. Spectrosc. Lasers Sens., 2006: pp. 403--433. http://www.kinetics.nsc.ru/chichinin/books/spectroscopy/articles/Walsh06_403.pdf (accessed October 5, 2017).

[80] J.F. Suyver, J. Grimm, M.K. Van Veen, D. Biner, K.W. Krämer, H.-U. Güdel, Upconversion spectroscopy and properties of NaYF4 doped with Er3+, Tm3+ and/or

Yb3+, J. Lumin. 117 (2006) 1–12.

[81] F. Vetrone, J.-C. Boyer, J.A. Capobianco, A. Speghini, M. Bettinelli, Significance of Yb3+ concentration on the upconversion mechanisms in codoped Y2O3:Er3+, Yb3+ nanocrystals, J. Appl. Phys. 96 (2004) 661–667. https://doi.org/10.1063/1.1739523.

[82] D. Matsuura, Red, green, and blue upconversion luminescence of trivalent-rare-earth ion-doped Y 2 O 3 nanocrystals, Appl. Phys. Lett. 81 (2002) 4526–4528.

[83] L. Yang, H. Song, L. Yu, Z. Liu, S. Lu, Unusual power-dependent and time-dependent upconversion luminescence in nanocrystals Y2O3: Ho3+/Yb3+, J. Lumin. 116 (2006) 101–106.

[84] J. Yang, C. Zhang, C. Peng, C. Li, L. Wang, R. Chai, J. Lin, Controllable red, green, blue (RGB) and bright white upconversion luminescence of Lu2O3: Yb3+/Er3+/Tm3+ nanocrystals through single laser excitation at 980 nm, Chem. Eur. J. 15 (2009) 4649–4655.

[85] H. Liu, L. Wang, S. Chen, Effect of Yb3+ concentration on the upconversion of Er3+ ion doped La2O3 nanocrystals under 980 nm excitation, Mater. Lett. 61 (2007) 3629–3631.

[86] R.M. Petoral Jr, F. Soderlind, A. Klasson, A. Suska, M.A. Fortin, N. Abrikossova, L. Selegård, P.-O. Kall, M. Engstrom, K. Uvdal, Synthesis and characterization of Tb3+-doped Gd2O3 nanocrystals: a bifunctional material with combined fluorescent labeling and MRI contrast agent properties, J. Phys. Chem. C. 113 (2009) 6913–6920.

[87] A.M. Pires, O.A. Serra, M.R. Davolos, Yttrium oxysulfide nanosized spherical particles doped with Yb and Er or Yb and Tm: efficient materials for up-converting phosphor technology field, J. Alloys Compd. 374 (2004) 181–184.

[88] X. Luo, W. Cao, Ethanol-assistant solution combustion method to prepare La2O2S: Yb, Pr nanometer phosphor, J. Alloys Compd. 460 (2008) 529–534.

[89] Z. Li, L. Zheng, L. Zhang, L. Xiong, Synthesis, characterization and upconversion emission properties of the nanocrystals of Yb3+/Er3+-codoped YF3–YOF–Y2O3 system, J. Lumin. 126 (2007) 481–486.

[90] Y.-P. Du, Y.-W. Zhang, L.-D. Sun, C.-H. Yan, Luminescent monodisperse nanocrystals of lanthanide oxyfluorides synthesized from trifluoroacetate precursors in high-boiling

solvents, J. Phys. Chem. C. 112 (2008) 405–415.

[91] S. Heer, O. Lehmann, M. Haase, H. Guedel, Blue, green, and red upconversion emission from lanthanide-doped LuPO4 and YbPO4 nanocrystals in a transparent colloidal solution, Angew. Chemie Int. Ed. 42 (2003) 3179–3182.

[92] A.Z. Zainurul, M.N. Asiah, C.H. Rosmani, F.S. Husairi, M. Rusop, S. Abdullah, Preparation of LaPO4 with Different Morphologies and Fluorescence Properties by Sol-Gel Spin-Coating Method, in: Adv. Mater. Res., Trans Tech Publ, 2014: pp. 562–566.

[93] Z. Chen, W. Bu, N. Zhang, J. Shi, Controlled construction of monodisperse La2 (MoO4) 3: Yb, Tm microarchitectures with upconversion luminescent property, J. Phys. Chem. C. 112 (2008) 4378–4383.

[94] G. Yi, B. Sun, F. Yang, D. Chen, Y. Zhou, J. Cheng, Synthesis and characterization of high-efficiency nanocrystal up-conversion phosphors: Ytterbium and erbium codoped lanthanum molybdate, Chem. Mater. 14 (2002) 2910–2914.

[95] N. Xue, X. Fan, Z. Wang, M. Wang, Synthesis process and luminescence properties of Ln3+ doped NaY (WO4) 2 nanoparticles, Mater. Lett. 61 (2007) 1576–1579.

[96] J. Su, F. Song, H. Tan, L. Han, F. Zhou, J. Tian, G. Zhang, Z. Cheng, H. Chen, Phonon-assisted mechanisms and concentration dependence of Tm3+ blue upconversion luminescence in codoped NaY (WO4) 2 crystals, J. Phys. D. Appl. Phys. 39 (2006) 2094.

[97] F. Pandozzi, F. Vetrone, J.-C. Boyer, R. Naccache, J.A. Capobianco, A. Speghini, M. Bettinelli, A spectroscopic analysis of blue and ultraviolet upconverted emissions from Gd3Ga5O12: Tm3+, Yb3+ nanocrystals, J. Phys. Chem. B. 109 (2005) 17400–17405.

[98] Y. Kuisheng, Z. Fang, W. Rina, L. Hansheng, Z. Xiyan, Upconversion luminescent properties of YVO4: Yb3+, Er3+ nano-powder by sol-gel method, J. Rare Earths. 24 (2006) 162–166.

[99] L. Liang, X. Zhang, H. Hu, L. Feng, M. Wu, Q. Su, Up-conversion properties in KGd2F7: Yb3+/Er3+, Mater. Lett. 59 (2005) 2186–2190.

[100] V. Mahalingam, F. Vetrone, R. Naccache, A. Speghini, J.A. Capobianco, Structural and optical investigation of colloidal Ln 3+/Yb 3+ co-doped KY3F10 nanocrystals, J. Mater. Chem. 19 (2009) 3149–3152.

[101] R. Naccache, F. Vetrone, V. Mahalingam, L.A. Cuccia, J.A. Capobianco, Controlled synthesis and water dispersibility of hexagonal phase NaGdF4: Ho3+/Yb3+ nanoparticles, Chem. Mater. 21 (2009) 717–723.

[102] X. Pei, Y. Hou, S. Zhao, Z. Xu, F. Teng, Frequency upconversion of Tm3+ and Yb3+ codoped YLiF4 synthesized by hydrothermal method, Mater. Chem. Phys. 90 (2005) 270–274.

[103] G.-S. Yi, G.-M. Chow, Colloidal LaF3: Yb, Er, LaF3: Yb, Ho and LaF3: Yb, Tm nanocrystals with multicolor upconversion fluorescence, J. Mater. Chem. 15 (2005) 4460–4464.

[104] S. Xiao, X. Yang, J.W. Ding, X.H. Yan, Up-Conversion in Yb3+−Tm3+ Co-Doped Lutetium Fluoride Particles Prepared by a Combustion−Fluorization Method, J. Phys. Chem. C. 111 (2007) 8161–8165. https://doi.org/10.1021/jp067323n.

[105] L. Gao, X. Ge, Z. Chai, G. Xu, X. Wang, C. Wang, Shape-controlled synthesis of octahedral α-NaYF 4 and its rare earth doped submicrometer particles in acetic acid, Nano Res. 2 (2009) 565–574.

[106] G. Wang, W. Qin, J. Zhang, J. Zhang, C. Cao, L. Wang, G. Wei, P. Zhu, R. Kim, Synthesis, growth mechanism, and tunable upconversion luminescence of Yb3+/Tm3+-codoped YF3 nanobundles, J. Phys. Chem. C. 112 (2008) 12161–12167.

[107] B.C. Grabmaier, Luminescent materials, Springer Verlag, 1994.

[108] F. Wang, Y. Han, C.S. Lim, Y. Lu, J. Wang, J. Xu, H. Chen, C. Zhang, M. Hong, X. Liu, Simultaneous phase and size control of upconversion nanocrystals through lanthanide doping, Nature. 463 (2010) 1061. https://doi.org/10.1038/nature08777.

[109] X. Ye, J.E. Collins, Y. Kang, J. Chen, D.T.N. Chen, A.G. Yodh, C.B. Murray, Morphologically controlled synthesis of colloidal upconversion nanophosphors and their shape-directed self-assembly, Proc. Natl. Acad. Sci. U. S. A. 107 (2010) 22430–22435. https://doi.org/10.1073/pnas.1008958107.

[110] M. Wang, G. Abbineni, A. Clevenger, C. Mao, S. Xu, Upconversion nanoparticles: Synthesis, surface modification and biological applications, Nanomedicine Nanotechnology, Biol. Med. 7 (2011) 710–729. https://doi.org/10.1016/j.nano.2011.02.013.

[111] D.L. Dexter, A Theory of Sensitized Luminescence in Solids, J. Chem. Phys. 21 (1953) 836–850. https://doi.org/10.1063/1.1699044.

[112] B. Zhou, B. Shi, D. Jin, X. Liu, Controlling upconversion nanocrystals for emerging applications, Nat. Nanotechnol. 10 (2015) 924–936. https://doi.org/10.1038/nnano.2015.251.

[113] M.-F. Joubert, Photon avalanche upconversion in rare earth laser materials, Opt. Mater. (Amst). 11 (1999) 181–203.

[114] J.S. Chivian, W.E. Case, D.D. Eden, The photon avalanche: A new phenomenon in Pr3+-based infrared quantum counters, Appl. Phys. Lett. 35 (1979) 124–125.

[115] J.M.F. Van Dijk, M.F.H. Schuurmans, On the nonradiative and radiative decay rates and a modified exponential energy gap law for 4 f–4 f transitions in rare-earth ions, J. Chem. Phys. 78 (1983) 5317–5323.

[116] F. Wang, J. Wang, X. Liu, Direct Evidence of a Surface Quenching Effect on Size-Dependent Luminescence of Upconversion Nanoparticles, Angew. Chemie Int. Ed. 49 (2010) 7456–7460. https://doi.org/10.1002/anie.201003959.

[117] I. Clarkson, R. Dickins, A. de Sousa, Non-radiative deactivation of the excited states of europium, terbium and ytterbium complexes by proximate energy-matched OH, NH and CH oscillators: an improved luminescence method for establishing solution hydration states, J. Chem. Soc. Perkin Trans. 2. (1999) 493–504.

[118] F. Wang, X. Liu, Upconversion multicolor fine-tuning: visible to near-infrared emission from lanthanide-doped NaYF4 nanoparticles, J. Am. Chem. Soc. 130 (2008) 5642–5643.

[119] D. Przybylska, A. Ekner-Grzyb, B.F. Grześkowiak, T. Grzyb, Upconverting SrF 2 nanoparticles doped with Yb 3+/Ho 3+, Yb 3+/Er 3+ and Yb 3+/Tm 3+ ions–optimisation of synthesis method, structural, spectroscopic and cytotoxicity studies, Sci. Rep. 9 (2019) 1–12.

[120] J. Wang, F. Wang, C. Wang, Z. Liu, X. Liu, Single-band upconversion emission in lanthanide-doped KMnF3 nanocrystals, Angew. Chemie - Int. Ed. 50 (2011) 10369–10372. https://doi.org/10.1002/anie.201104192.

[121] G. Tian, Z. Gu, L. Zhou, W. Yin, X. Liu, L. Yan, S. Jin, W. Ren, G. Xing, S. Li, Mn2+

dopant-controlled synthesis of NaYF4: Yb/Er upconversion nanoparticles for in vivo imaging and drug delivery, Adv. Mater. 24 (2012) 1226–1231.

[122] F. Zhang, Upconversion Luminescence of Lanthanide Ion-Doped Nanocrystals, in: Phot. Upconversion Nanomater. Nanostructure Sci. Technol., Springer, Berlin, Heidelberg, 2014: pp. 73–119. https://doi.org/https://doi.org/10.1007/978-3-662-45597-5_3.

[123] C. Ming, F. Song, L. Yan, Spectroscopic study and green upconversion of Pr3+/Yb3+-codoped NaY (WO4) 2 crystal, Opt. Commun. 286 (2013) 217–220.

[124] F. Pellé, M. Dhaouadi, L. Michely, P. Aschehoug, A. Toncelli, S. Veronesi, M. Tonelli, Spectroscopic properties and upconversion in Pr 3+: YF3 nanoparticles, Phys. Chem. Chem. Phys. 13 (2011) 17453–17460.

[125] G.S. Maciel, R.B. Guimarães, P.G. Barreto, I.C.S. Carvalho, N. Rakov, The influence of Yb3+ doping on the upconversion luminescence of Pr3+ in aluminum oxide based powders prepared by combustion synthesis, Opt. Mater. (Amst). 31 (2009) 1735–1740.

[126] R. Naccache, F. Vetrone, A. Speghini, M. Bettinelli, J.A. Capobianco, Cross-relaxation and upconversion processes in Pr3+ singly doped and Pr3+/Yb3+ codoped nanocrystalline Gd3Ga5O12: the sensitizer/activator relationship, J. Phys. Chem. C. 112 (2008) 7750–7756.

[127] C. Joshi, S.B. Rai, Structural, thermal, and optical properties of Pr3+/Yb3+ co-doped oxyhalide tellurite glasses and its nano-crystalline parts, Solid State Sci. 14 (2012) 997–1003.

[128] F. Wang, R. Deng, J. Wang, Q. Wang, Y. Han, H. Zhu, X. Chen, X. Liu, Tuning upconversion through energy migration in core–shell nanoparticles, Nat. Mater. 10 (2011) 968–973. https://doi.org/10.1038/nmat3149.

[129] Q. Su, S. Han, X. Xie, H. Zhu, H. Chen, C.-K. Chen, R.-S. Liu, X. Chen, F. Wang, X. Liu, The effect of surface coating on energy migration-mediated upconversion, J. Am. Chem. Soc. 134 (2012) 20849–20857.

[130] C. Liu, D. Chen, Controlled synthesis of hexagon shaped lanthanide-doped LaF 3 nanoplates with multicolor upconversion fluorescence, J. Mater. Chem. 17 (2007) 3875–3880.

[131] X. Qin, T. Yokomori, Y. Ju, Flame synthesis and characterization of rare-earth (Er 3+, Ho 3+, and Tm 3+) doped upconversion nanophosphors, Appl. Phys. Lett. 90 (2007) 73104.

[132] O. Ehlert, R. Thomann, M. Darbandi, T. Nann, A four-color colloidal multiplexing nanoparticle system, ACS Nano. 2 (2008) 120–124.

[133] S. Heer, K. Kömpe, H. Güdel, M. Haase, Highly efficient multicolour upconversion emission in transparent colloids of lanthanide-doped NaYF4 nanocrystals, Adv. Mater. 16 (2004) 2102–2105.

[134] G.S. Yi, G.M. Chow, Synthesis of hexagonal-phase NaYF4: Yb, Er and NaYF4: Yb, Tm nanocrystals with efficient up-conversion fluorescence, Adv. Funct. Mater. 16 (2006) 2324–2329.

[135] X. Zhang, P. Yang, C. Li, D. Wang, J. Xu, S. Gai, J. Lin, Facile and mass production synthesis of β-NaYF 4: Yb 3+, Er 3+/Tm 3+ 1D microstructures with multicolor up-conversion luminescence, Chem. Commun. 47 (2011) 12143–12145.

[136] V. Mahalingam, F. Vetrone, R. Naccache, A. Speghini, J.A. Capobianco, Colloidal Tm3+/Yb3+-doped LiYF4 nanocrystals: multiple luminescence spanning the UV to NIR regions via low-energy excitation, Adv. Mater. 21 (2009) 4025–4028.

[137] S. Fischer, N.D. Bronstein, J.K. Swabeck, E.M. Chan, A.P. Alivisatos, Precise tuning of surface quenching for luminescence enhancement in core–shell lanthanide-doped nanocrystals, Nano Lett. 16 (2016) 7241–7247.

[138] N.J.J. Johnson, S. He, S. Diao, E.M. Chan, H. Dai, A. Almutairi, Direct evidence for coupled surface and concentration quenching dynamics in lanthanide-doped nanocrystals, J. Am. Chem. Soc. 139 (2017) 3275–3282.

[139] S.K.W. MacDougall, A. Ivaturi, J. Marques-Hueso, K.W. Krämer, B.S. Richards, Ultra-high photoluminescent quantum yield of β-NaYF 4: 10% Er 3+ via broadband excitation of upconversion for photovoltaic devices, Opt. Express. 20 (2012) A879–A887.

[140] J. Zhao, D. Jin, E.P. Schartner, Y. Lu, Y. Liu, A. V Zvyagin, L. Zhang, J.M. Dawes, P. Xi, J.A. Piper, Single-nanocrystal sensitivity achieved by enhanced upconversion luminescence, Nat. Nanotechnol. 8 (2013) 729–734.

[141] Q. Huang, J. Yu, E. Ma, K. Lin, Synthesis and characterization of highly efficient near-

infrared upconversion Sc3+/Er3+/Yb3+ tridoped NaYF4, J. Phys. Chem. C. 114 (2010) 4719–4724.

[142] M.D. Wisser, S. Fischer, C. Siefe, A.P. Alivisatos, A. Salleo, J.A. Dionne, Improving quantum yield of upconverting nanoparticles in aqueous media via emission sensitization, Nano Lett. 18 (2018) 2689–2695.

[143] W. Zou, C. Visser, J.A. Maduro, M.S. Pshenichnikov, J.C. Hummelen, Broadband dye-sensitized upconversion of near-infrared light, Nat. Photonics. 6 (2012) 560–564.

[144] J. Zhang, C.M. Shade, D.A. Chengelis, S. Petoud, A strategy to protect and sensitize near-infrared luminescent Nd3+ and Yb3+: organic tropolonate ligands for the sensitization of Ln3+-doped NaYF4 nanocrystals, J. Am. Chem. Soc. 129 (2007) 14834–14835.

[145] G.-S. Yi, G.-M. Chow, Water-soluble NaYF4: Yb, Er (Tm)/NaYF4/polymer core/shell/shell nanoparticles with significant enhancement of upconversion fluorescence, Chem. Mater. 19 (2007) 341–343.

[146] L. Liang, A. Care, R. Zhang, Y. Lu, N.H. Packer, A. Sunna, Y. Qian, A. V. Zvyagin, Facile Assembly of Functional Upconversion Nanoparticles for Targeted Cancer Imaging and Photodynamic Therapy, ACS Appl. Mater. Interfaces. 8 (2016) 11945–11953. https://doi.org/10.1021/acsami.6b00713.

[147] X. Li, D. Shen, J. Yang, C. Yao, R. Che, F. Zhang, D. Zhao, Successive layer-by-layer strategy for multi-shell epitaxial growth: shell thickness and doping position dependence in upconverting optical properties, Chem. Mater. 25 (2013) 106–112.

[148] F. Vetrone, R. Naccache, V. Mahalingam, C.G. Morgan, J.A. Capobianco, The active-core/active-shell approach: A strategy to enhance the upconversion luminescence in lanthanide-doped nanoparticles, Adv. Funct. Mater. 19 (2009) 2924–2929.

[149] J. Shan, J. Chen, J. Meng, J. Collins, W. Soboyejo, J.S. Friedberg, Y. Ju, Biofunctionalization, cytotoxicity, and cell uptake of lanthanide doped hydrophobically ligated NaYF 4 upconversion nanophosphors, J. Appl. Phys. 104 (2008) 94308.

[150] D.M. Wu, A. García-Etxarri, A. Salleo, J.A. Dionne, Plasmon-Enhanced Upconversion, J. Phys. Chem. Lett. 5 (2014) 4020–4031. https://doi.org/10.1021/jz5019042.

[151] D. Lu, S.K. Cho, S. Ahn, L. Brun, C.J. Summers, W. Park, Plasmon enhancement

mechanism for the upconversion processes in NaYF4: Yb3+, Er3+ nanoparticles: Maxwell versus Förster, ACS Nano. 8 (2014) 7780–7792.

[152] M. Saboktakin, X. Ye, S.J. Oh, S.-H. Hong, A.T. Fafarman, U.K. Chettiar, N. Engheta, C.B. Murray, C.R. Kagan, Metal-enhanced upconversion luminescence tunable through metal nanoparticle–nanophosphor separation, ACS Nano. 6 (2012) 8758–8766.

[153] W. Deng, L. Sudheendra, J. Zhao, J. Fu, D. Jin, I.M. Kennedy, E.M. Goldys, Upconversion in NaYF4:Yb, Er nanoparticles amplified by metal nanostructures, Nanotechnology. 22 (2011). https://doi.org/10.1088/0957-4484/22/32/325604.

[154] W. Xu, X. Chen, H. Song, Upconversion manipulation by local electromagnetic field, Nano Today. 17 (2017) 54–78. https://doi.org/10.1016/J.NANTOD.2017.10.011.

[155] H. Zhang, Y. Li, I.A. Ivanov, Y. Qu, Y. Huang, X. Duan, Plasmonic modulation of the upconversion fluorescence in NaYF4: Yb/Tm hexaplate nanocrystals using gold nanoparticles or nanoshells, Angew. Chemie Int. Ed. 49 (2010) 2865–2868.

[156] P. Kannan, F.A. Rahim, X. Teng, R. Chen, H. Sun, L. Huang, D.-H. Kim, Enhanced emission of NaYF4: Yb, Er/Tm nanoparticles by selective growth of Au and Ag nanoshells, RSC Adv. 3 (2013) 7718–7721.

[157] K. Poorkazem, A. V Hesketh, T.L. Kelly, Plasmon-enhanced triplet–triplet annihilation using silver nanoplates, J. Phys. Chem. C. 118 (2014) 6398–6404.

[158] S. Schietinger, T. Aichele, H.-Q. Wang, T. Nann, O. Benson, Plasmon-enhanced upconversion in single NaYF4: Yb3+/Er3+ codoped nanocrystals, Nano Lett. 10 (2010) 134–138.

[159] S. Baluschev, F. Yu, T. Miteva, S. Ahl, A. Yasuda, G. Nelles, W. Knoll, G. Wegner, Metal-Enhanced Up-Conversion Fluorescence: Effective Triplet− Triplet Annihilation near Silver Surface, Nano Lett. 5 (2005) 2482–2484.

[160] W. Zhang, F. Ding, S.Y. Chou, Large Enhancement of Upconversion Luminescence of NaYF4: Yb3+/Er3+ Nanocrystal by 3D Plasmonic Nano-Antennas, Adv. Mater. 24 (2012) OP236–OP241.

[161] E. Verhagen, L. Kuipers, A. Polman, A.G. Brolo, S.C. Kwok, M.D. Cooper, M.G. Moffitt, C. Wang, R. Gordon, J. Riordon, K.L. Kavanagh, W. Fan, S. Zhang, K.J. Malloy, S.R. J Brueck, N.C. Panoiu, R.M. Osgood, Field enhancement in metallic

subwavelength aperture arrays probed by erbium upconversion luminescence, Second Harmon. Gener. from a Nanopatterned Isotropic Nonlinear Mater. Nano Lett. 17 (2009) 1027–1030. https://www.osapublishing.org/DirectPDFAccess/C4D52AF4-A3EF-40E0-6E8DE0E225398036_184318/oe-17-17-14586.pdf?da=1&id=184318&seq=0&mobile=no (accessed January 25, 2018).

[162] J. Wang, R. Deng, M.A. MacDonald, B. Chen, J. Yuan, F. Wang, D. Chi, T.S. Andy Hor, P. Zhang, G. Liu, Y. Han, X. Liu, Enhancing multiphoton upconversion through energy clustering at sublattice level, Nat. Mater. 13 (2013) 157–162. https://doi.org/10.1038/nmat3804.

[163] S. Wu, G. Han, D.J. Milliron, S. Aloni, V. Altoe, D. V Talapin, B.E. Cohen, P.J. Schuck, Non-blinking and photostable upconverted luminescence from single lanthanide-doped nanocrystals, Proc. Natl. Acad. Sci. 106 (2009) 10917–10921.

[164] H. Zijlmans, J. Bonnet, J. Burton, K. Kardos, T. Vail, R.S. Niedbala, H.J. Tanke, Detection of cell and tissue surface antigens using up-converting phosphors: a new reporter technology, Anal. Biochem. 267 (1999) 30–36.

[165] M. Nyk, R. Kumar, T.Y. Ohulchanskyy, E.J. Bergey, P.N. Prasad, High contrast in vitro and in vivo photoluminescence bioimaging using near infrared to near infrared up-conversion in Tm3+ and Yb3+ doped fluoride nanophosphors, Nano Lett. 8 (2008) 3834–3838.

[166] D.J. Gargas, E.M. Chan, A.D. Ostrowski, S. Aloni, M.V.P. Altoe, E.S. Barnard, B. Sanii, J.J. Urban, D.J. Milliron, B.E. Cohen, Engineering bright sub-10-nm upconverting nanocrystals for single-molecule imaging, Nat. Nanotechnol. 9 (2014) 300–305.

[167] Y. Sun, J. Peng, W. Feng, F. Li, Upconversion nanophosphors NaLuF4: Yb, Tm for lymphatic imaging in vivo by real-time upconversion luminescence imaging under ambient light and high-resolution X-ray CT, Theranostics. 3 (2013) 346.

[168] M. Wang, C.-C. Mi, W.-X. Wang, C.-H. Liu, Y.-F. Wu, Z.-R. Xu, C.-B. Mao, S.-K. Xu, Immunolabeling and NIR-excited fluorescent imaging of HeLa cells by using NaYF4: Yb, Er upconversion nanoparticles, ACS Nano. 3 (2009) 1580–1586.

[169] S. Jiang, Y. Zhang, K.M. Lim, E.K.W. Sim, L. Ye, NIR-to-visible upconversion nanoparticles for fluorescent labeling and targeted delivery of siRNA, Nanotechnology.

20 (2009) 155101.

[170] Y. Yang, B. Velmurugan, X. Liu, B. Xing, NIR photoresponsive crosslinked upconverting nanocarriers toward selective intracellular drug release, Small. 9 (2013) 2937–2944.

[171] C. Wang, L. Cheng, Z. Liu, Drug delivery with upconversion nanoparticles for multi-functional targeted cancer cell imaging and therapy, Biomaterials. 32 (2011) 1110–1120.

[172] N.M. Idris, M.K. Gnanasammandhan, J. Zhang, P.C. Ho, R. Mahendran, Y. Zhang, In vivo photodynamic therapy using upconversion nanoparticles as remote-controlled nanotransducers, Nat. Med. 18 (2012) 1580–1585. https://doi.org/10.1038/nm.2933.

[173] Q. Chen, C. Wang, L. Cheng, W. He, Z. Cheng, Z. Liu, Protein modified upconversion nanoparticles for imaging-guided combined photothermal and photodynamic therapy, Biomaterials. 35 (2014) 2915–2923.

[174] Y. Tang, W. Di, X. Zhai, R. Yang, W. Qin, NIR-responsive photocatalytic activity and mechanism of NaYF4: Yb, Tm@ TiO2 core–shell nanoparticles, Acs Catal. 3 (2013) 405–412.

[175] W. Wang, M. Ding, C. Lu, Y. Ni, Z. Xu, A study on upconversion UV–vis–NIR responsive photocatalytic activity and mechanisms of hexagonal phase NaYF4: Yb3+, Tm3+@ TiO2 core–shell structured photocatalyst, Appl. Catal. B Environ. 144 (2014) 379–385.

[176] W. Su, M. Zheng, L. Li, K. Wang, R. Qiao, Y. Zhong, Y. Hu, Z. Li, Directly coat TiO 2 on hydrophobic NaYF 4: Yb, Tm nanoplates and regulate their photocatalytic activities with the core size, J. Mater. Chem. A. 2 (2014) 13486–13491.

[177] Z.Q. Li, X.D. Li, Q.Q. Liu, X.H. Chen, Z. Sun, C. Liu, X.J. Ye, S.M. Huang, Core/shell structured NaYF4:Yb 3+/Er 3+/Gd +3 nanorods with Au nanoparticles or shells for flexible amorphous silicon solar cells, Nanotechnology. 23 (2012). https://doi.org/10.1088/0957-4484/23/2/025402.

[178] W. Qin, D. Zhang, D. Zhao, L. Wang, K. Zheng, Near-infrared photocatalysis based on YF3:Yb3+, Tm3+/TiO2 core/shell nanoparticles, Chem. Commun. 46 (2010) 2304–2306. https://doi.org/10.1039/b924052g.

[179] Q. Tian, W. Yao, W. Wu, C. Jiang, NIR light-activated upconversion semiconductor photocatalysts, Nanoscale Horizons. 4 (2019) 10–25. https://doi.org/10.1039/c8nh00154e.

[180] J. Moma, Modified Titanium Dioxide for Photocatalytic Applications, in: J.B.E.-S.B.K.E.-K. Akhtar (Ed.), IntechOpen, Rijeka, 2019: p. Ch. 3. https://doi.org/10.5772/intechopen.79374.

[181] S. Obregón, A. Kubacka, M. Fernández-García, G. Colón, High-performance Er3+-TiO2 system: Dual up-conversion and electronic role of the lanthanide, J. Catal. 299 (2013) 298–306. https://doi.org/10.1016/j.jcat.2012.12.021.

[182] J. Wang, T. Wei, X. Li, B. Zhang, J. Wang, C. Huang, Q. Yuan, Near-Infrared-Light-Mediated Imaging of Latent Fingerprints based on Molecular Recognition, Angew. Chemie. 126 (2014) 1642–1646. https://doi.org/10.1002/ange.201308843.

[183] M. You, J. Zhong, Y. Hong, Z. Duan, M. Lin, F. Xu, Inkjet printing of upconversion nanoparticles for anti-counterfeit applications, Nanoscale. 7 (2015) 4423–4431. https://doi.org/10.1039/C4NR06944G.

[184] Y. Lu, J. Zhao, R. Zhang, Y. Liu, D. Liu, E.M. Goldys, X. Yang, P. Xi, A. Sunna, J. Lu, Y. Shi, R.C. Leif, Y. Huo, J. Shen, J.A. Piper, J.P. Robinson, D. Jin, Tunable lifetime multiplexing using luminescent nanocrystals, Nat. Photonics. 8 (2014) 32–36. https://doi.org/10.1038/nphoton.2013.322.

[185] J.M. Meruga, A. Baride, W. Cross, J.J. Kellar, P.S. May, Red-green-blue printing using luminescence-upconversion inks, J. Mater. Chem. C. 2 (2014) 2221–2227.

[186] C. Zhang, H.P. Ou, L.Y. Liao, W. Feng, W. Sun, Z.X. Li, C.H. Xu, C.J. Fang, L.D. Sun, Y.W. Zhang, C.H. Yan, Luminescence modulation of ordered upconversion nanopatterns by a photochromic diarylethene: Rewritable optical storage with nondestructive readout, Adv. Mater. 22 (2010) 633–637. https://doi.org/10.1002/adma.200901722.

[187] H.S. Mader, O.S. Wolfbeis, Optical ammonia sensor based on upconverting luminescent nanoparticles, Anal. Chem. 82 (2010) 5002–5004. https://doi.org/10.1021/ac1007283.

[188] R. Ali, S.M. Saleh, R.J. Meier, H.A. Azab, I.I. Abdelgawad, O.S. Wolfbeis, Upconverting nanoparticle based optical sensor for carbon dioxide, Sensors Actuators,

B Chem. 150 (2010) 126–131. https://doi.org/10.1016/j.snb.2010.07.031.

[189] A. Lay, D.S. Wang, M.D. Wisser, R.D. Mehlenbacher, Y. Lin, M.B. Goodman, W.L. Mao, J.A. Dionne, Upconverting Nanoparticles as Optical Sensors of Nano- to Micro-Newton Forces, Nano Lett. 17 (2017) 4172–4177. https://doi.org/10.1021/acs.nanolett.7b00963.

[190] S.M. Saleh, R. Ali, T. Hirsch, O.S. Wolfbeis, Detection of biotin–avidin affinity binding by exploiting a self-referenced system composed of upconverting luminescent nanoparticles and gold nanoparticles, J. Nanoparticle Res. 13 (2011) 4603–4611.

[191] L. Yao, J. Zhou, J. Liu, W. Feng, F. Li, Iridium-Complex-Modified Upconversion Nanophosphors for Effective LRET Detection of Cyanide Anions in Pure Water, Adv. Funct. Mater. 22 (2012) 2667–2672.

[192] Q. Liu, J. Peng, L. Sun, F. Li, High-efficiency upconversion luminescent sensing and bioimaging of Hg (II) by chromophoric ruthenium complex-assembled nanophosphors, ACS Nano. 5 (2011) 8040–8048.

[193] D.E. Achatz, R.J. Meier, L.H. Fischer, O.S. Wolfbeis, Luminescent sensing of oxygen using a quenchable probe and upconverting nanoparticles, Angew. Chemie - Int. Ed. 50 (2011) 260–263. https://doi.org/10.1002/anie.201004902.

[194] L.-N. Sun, H. Peng, M.I.J. Stich, D. Achatz, O.S. Wolfbeis, pH sensor based on upconverting luminescent lanthanide nanorods, Chem. Commun. (2009) 5000–5002.

[195] C.D.S. Brites, S. Balabhadra, L.D. Carlos, Lanthanide-Based Thermometers: At the Cutting-Edge of Luminescence Thermometry, Adv. Opt. Mater. 7 (2019) 1801239. https://doi.org/10.1002/adom.201801239.

[196] V.K. Rai, Temperature sensors and optical sensors, Appl. Phys. B Lasers Opt. 88 (2007) 297–303. https://doi.org/10.1007/s00340-007-2717-4.

[197] H. Suo, C. Guo, J. Zheng, B. Zhou, C. Ma, X. Zhao, T. Li, P. Guo, E.M. Goldys, Sensitivity Modulation of Upconverting Thermometry through Engineering Phonon Energy of a Matrix, ACS Appl. Mater. Interfaces. 8 (2016) 30312–30319. https://doi.org/10.1021/acsami.6b12176.

[198] F. Vetrone, R. Naccache, A. Zamarrón, A.J. De La Fuente, F. Sanz-Rodríguez, L.M. Maestro, E.M. Rodriguez, D. Jaque, J.G. Sole, J.A. Capobianco, Temperature sensing

using fluorescent nanothermometers, ACS Nano. 4 (2010) 3254–3258. https://doi.org/10.1021/nn100244a.

[199] R. Kumar, L. Binetti, T.H. Nguyen, L.S.M. Alwis, T. Sun, K.T. V Grattan, Optical fibre thermometry using ratiometric green emission of an upconverting nanoparticle-polydimethylsiloxane composite, Sensors Actuators A Phys. (2020) 112083.

[200] A. Lay, D.S. Wang, M.D. Wisser, R.D. Mehlenbacher, Y. Lin, M.B. Goodman, W.L. Mao, J.A. Dionne, Upconverting Nanoparticles as Optical Sensors of Nano- to Micro-Newton Forces, Nano Lett. (2017). https://doi.org/10.1021/acs.nanolett.7b00963.

[201] J. Wang, T. Ming, Z. Jin, J. Wang, L.D. Sun, C.H. Yan, Photon energy upconversion through thermal radiation with the power efficiency reaching 16%, Nat. Commun. 5 (2014) 1–9. https://doi.org/10.1038/ncomms6669.

[202] Y. Liu, A. Teitelboim, A. Fernandez-Bravo, K. Yao, M.V.P. Altoe, S. Aloni, C. Zhang, B.E. Cohen, P.J. Schuck, E.M. Chan, Controlled Assembly of Upconverting Nanoparticles for Low-Threshold Microlasers and Their Imaging in Scattering Media, ACS Nano. 14 (2020) 1508–1519.

[203] Y. Liu, Y. Lu, X. Yang, X. Zheng, S. Wen, F. Wang, X. Vidal, J. Zhao, D. Liu, Z. Zhou, C. Ma, J. Zhou, J.A. Piper, P. Xi, D. Jin, Amplified stimulated emission in upconversion nanoparticles for super-resolution nanoscopy, Nature. 543 (2017) 229–233. https://doi.org/10.1038/nature21366.

[204] R. Deng, F. Qin, R. Chen, W. Huang, M. Hong, X. Liu, Temporal full-colour tuning through non-steady-state upconversion, Nat. Nanotechnol. 10 (2015) 237–242. https://doi.org/10.1038/nnano.2014.317.

[205] M. Yin, L. Wu, Z. Li, J. Ren, X. Qu, Facile in situ fabrication of graphene–upconversion hybrid materials with amplified electrogenerated chemiluminescence, Nanoscale. 4 (2012) 400–404. https://doi.org/10.1039/C1NR11393C.

[206] A. Kumar, X.-J. Liang, Gold Nanomaterials as Prospective Metal-based Delivery Systems for Cancer Treatment BT - Encyclopedia of Metalloproteins, in: R.H. Kretsinger, V.N. Uversky, E.A. Permyakov (Eds.), Springer New York, New York, NY, 2013: pp. 875–887. https://doi.org/10.1007/978-1-4614-1533-6_579.

[207] J. Turkevitch, P.C. Stevenson, J. Hillier, Nucleation and growth process in the synthesis

of colloidal gold. Discuss. Faraday Soc, (1951).

[208] M. Brust, M. Walker, D. Bethell, D.J. Schiffrin, R. Whyman, Synthesis of thiol-derivatised gold nanoparticles in a two-phase liquid–liquid system, J. Chem. Soc. Chem. Commun. (1994) 801–802.

[209] S.E. Lohse, C.J. Murphy, The Quest for Shape Control: A History of Gold Nanorod Synthesis, Chem. Mater. 25 (2013) 1250–1261. https://doi.org/10.1021/cm303708p.

[210] G. Mie, Beiträge zur Optik trüber Medien, speziell kolloidaler Metallösungen, Ann. Phys. 330 (1908) 377–445.

[211] S. Link, M.A. El-Sayed, Simulation of the optical absorption spectra of gold nanorods as a function of their aspect ratio and the effect of the medium dielectric constant, J. Phys. Chem. B. 109 (2005) 10531–10532.

[212] Market Research Report, Temperature Sensors Market Analysis By Application (Automotive, Consumer Electronics, Environmental, Medical, Process Industries) and Segment Forecasts to 2020, San Francisco, 2015. https://doi.org/ISBN 978-1-68038-495-6.

[213] K.T.V. Grattan, P. A.W, Wilson, A miniaturised microcomputer-based neodymium “decay-time” temperature sensor, J. Phys. E. 20 (1987) 1201–1205. https://doi.org/10.1088/0022-3735/20/10/010.

[214] K.T.V. Grattan, A.W. Palmer, Infrared fluorescence “decay-time” temperature sensor, Rev. Sci. Instrum. 56 (1985) 1784–1787. https://doi.org/10.1063/1.1138094.

[215] S. Pal, J. Mandal, T. Sun, K.T.V. Grattan, M. Fokine, F. Carlsson, P.Y. Fonjallaz, S.A. Wade, S.F. Collins, Characteristics of potential fibre Bragg grating sensor-based devices at elevated temperatures, Meas. Sci. Technol. 14 (2003) 1131–1136. https://doi.org/10.1088/0957-0233/14/7/331.

[216] Z.Y. Zhang, K.T.V. Grattan, A.W. Palmer, B.T. Meggitt, T. Sun, Fluorescence decay-time characteristics of erbium-doped optical fiber at elevated temperatures, Rev. Sci. Instrum. 68 (1997) 2764–2766. https://doi.org/10.1063/1.1148192.

[217] L.M. Maestro, C. Jacinto, U.R. Silva, F. Vetrone, J.A. Capobianco, D. Jaque, J.G. Solé, CdTe quantum dots as nanothermometers: Towards highly sensitive thermal imaging, Small. 7 (2011) 1774–1778. https://doi.org/10.1002/smll.201002377.

[218] H.F. Arata, P. Löw, K. Ishizuka, C. Bergaud, B. Kim, H. Noji, H. Fujita, Temperature distribution measurement on microfabricated thermodevice for single biomolecular observation using fluorescent dye, Sensors Actuators, B Chem. 117 (2006) 339–345. https://doi.org/10.1016/j.snb.2005.11.017.

[219] R.H. Compton, K.T.V. Grattan, T. Morrow, Photophysical parameters for potential vapour-phase dye-laser media, Appl. Phys. 22 (1980) 307–311. https://doi.org/10.1007/BF00899883.

[220] Y. Wang, W. Cao, S. Li, W. Wen, Facile and high spatial resolution ratio-metric luminescence thermal mapping in microfluidics by near infrared excited upconversion nanoparticles, Appl. Phys. Lett. 108 (2016). https://doi.org/10.1063/1.4940746.

[221] K. Binnemans, Lanthanide-based luminescent hybrid materials, Chem. Rev. 109 (2009) 4283–4374. https://doi.org/10.1021/cr8003983.

[222] S. Zheng, W. Chen, D. Tan, J. Zhou, Q. Guo, W. Jiang, C. Xu, X. Liu, J. Qiu, Lanthanide-doped NaGdF4 core-shell nanoparticles for non-contact self-referencing temperature sensors, Nanoscale. 6 (2014) 5675–5679. https://doi.org/10.1039/c4nr00432a.

[223] S.F. León-Luis, U.R. Rodríguez-Mendoza, P. Haro-González, I.R. Martín, V. Lavín, Role of the host matrix on the thermal sensitivity of Er 3+ luminescence in optical temperature sensors, Sensors Actuators, B Chem. 174 (2012) 176–186. https://doi.org/10.1016/j.snb.2012.08.019.

[224] B. Dong, T. Yang, M.K. Lei, Optical high temperature sensor based on green up-conversion emissions in Er3+ doped Al2O3, Sensors Actuators, B Chem. 123 (2007) 667–670. https://doi.org/10.1016/j.snb.2006.10.002.

[225] S. Balabhadra, M.L. Debasu, C.D.S. Brites, R.A.S. Ferreira, L.D. Carlos, Upconverting Nanoparticles Working As Primary Thermometers in Different Media, J. Phys. Chem. C. 121 (2017) 13962–13968. https://doi.org/10.1021/acs.jpcc.7b04827.

[226] A. Li, D. Xu, H. Lin, S. Yang, Y. Shao, Y. Zhang, NaGd(MoO4)2 nanocrystals with diverse morphologies: Controlled synthesis, growth mechanism, photoluminescence and thermometric properties, Sci. Rep. 6 (2016). https://doi.org/10.1038/srep31366.

[227] A. Pandey, S. Som, V. Kumar, V. Kumar, K. Kumar, V.K. Rai, H.C. Swart, Enhanced

upconversion and temperature sensing study of Er3+-Yb3+ codoped tungsten-tellurite glass, Sensors Actuators, B Chem. 202 (2014) 1305–1312. https://doi.org/10.1016/j.snb.2014.06.074.

[228] M. Kochanowicz, D. Dorosz, J. Zmojda, J. Dorosz, P. Miluski, Influence of temperature on upconversion luminescence in tellurite glass co-doped with Yb3+/Er3+ and Yb3+/Tm 3+, J. Lumin. 151 (2014) 155–160. https://doi.org/10.1016/j.jlumin.2014.02.012.

[229] D. Manzani, J.F. da S. Petruci, K. Nigoghossian, A.A. Cardoso, S.J.L. Ribeiro, A portable luminescent thermometer based on green up-conversion emission of Er3+/Yb3+ co-doped tellurite glass, Sci. Rep. 7 (2017) 41596. https://doi.org/10.1038/srep41596.

[230] S.F. León-Luis, U.R. Rodríguez-Mendoza, I.R. Martín, E. Lalla, V. Lavín, Effects of Er3+ concentration on thermal sensitivity in optical temperature fluorotellurite glass sensors, Sensors Actuators, B Chem. 176 (2013) 1167–1175. https://doi.org/10.1016/j.snb.2012.09.067.

[231] W. Xu, H. Zhao, Z. Zhang, W. Cao, Highly sensitive optical thermometry through thermally enhanced near infrared emissions from Nd3+/Yb3+ codoped oxyfluoride glass ceramic, Sensors Actuators, B Chem. 178 (2013) 520–524. https://doi.org/10.1016/j.snb.2012.12.050.

[232] L. Feng, B. Lai, J. Wang, G. Du, Q. Su, Spectroscopic properties of Er3+ in a oxyfluoride glass and upconversion and temperature sensor behaviour of Er3+/Yb3+-codoped oxyfluoride glass, J. Lumin. 130 (2010) 2418–2423. https://doi.org/10.1016/j.jlumin.2010.08.005.

[233] P. Haro-González, S.F. León-Luis, S. González-Pérez, I.R. Martín, Analysis of Er3+ and Ho3+ codoped fluoroindate glasses as wide range temperature sensor, Mater. Res. Bull. 46 (2011) 1051–1054. https://doi.org/10.1016/j.materresbull.2011.03.010.

[234] G.S. et al. Maciel, Temperature sensor based on frequency upconversion in Er3+-doped fluoroindate glass, IEEE Photon. Technol. Lett. 7 (1995) 1474–1476.

[235] P. V Dos Santos, M.T. De Araujo, A.S. Gouveia-Neto, J.A.M. Neto, A.S.B. Sombra, Optical Thermometry Through Infrared Excited Upconversion Fluorescence Emission

in Er3+- and Er3+-Yb3+-doped Chalcogenide Glasses, IEEE J. Quantum Electron. 35 (1999) 395. https://doi.org/10.1109/3.748846.

[236] B. Lai, L. Feng, J. Wang, Q. Su, Optical transition and upconversion luminescence in Er3+ doped and Er3+-Yb3+ co-doped fluorophosphate glasses, Opt. Mater. (Amst). 32 (2010) 1154–1160. https://doi.org/10.1016/j.optmat.2010.03.023.

[237] Y. Zhao, X. Wang, Y. Zhang, Y. Li, X. Yao, Optical temperature sensing of up-conversion luminescent materials: Fundamentals and progress, J. Alloys Compd. 817 (2020). https://doi.org/10.1016/j.jallcom.2019.152691.

[238] J. Cao, M.H. Tu, T. Sun, K.T.V. Grattan, Wavelength-based localized surface plasmon resonance optical fiber biosensor, Sensors Actuators, B Chem. 181 (2013) 611–619. https://doi.org/10.1016/j.snb.2013.02.052.

[239] A. Aebischer, M. Hostettler, J. Hauser, K. Krämer, T. Weber, H.U. Güdel, H.B. Bürgi, Structural and spectroscopic characterization of active sites in a family of light-emitting sodium lanthanide tetrafluorides, Angew. Chemie - Int. Ed. 45 (2006) 2802–2806. https://doi.org/10.1002/anie.200503966.

[240] A. Piruska, I. Nikcevic, S.H. Lee, C. Ahn, W.R. Heineman, P.A. Limbach, C.J. Seliskar, The autofluorescence of plastic materials and chips measured under laser irradiation, Lab Chip. 5 (2005) 1348–1354. https://doi.org/10.1039/b508288a.

[241] F. Wang, R. Deng, X. Liu, Preparation of core-shell NaGdF4 nanoparticles doped with luminescent lanthanide ions to be used as upconversion-based probes, Nat. Protoc. 9 (2014) 1634. https://doi.org/10.1038/nprot.2014.111.

[242] H. Althues, R. Palkovits, A. Rumplecker, P. Simon, W. Sigle, M. Bredol, U. Kynast, S. Kaskel, Synthesis and characterization of transparent luminescent ZnS:Mn/PMMA nanocomposites, Chem. Mater. 18 (2006) 1068–1072. https://doi.org/10.1021/cm0477422.

[243] S. Lee, H.J. Shin, S.M. Yoon, D.K. Yi, J.Y. Choi, U. Paik, Refractive index engineering of transparent ZrO2- polydimethylsiloxane nanocomposites, J. Mater. Chem. 18 (2008) 1751–1755. https://doi.org/10.1039/b715338d.

[244] N. Bogdan, F. Vetrone, G.A. Ozin, J.A. Capobianco, Synthesis of ligand-free colloidally stable water dispersible brightly luminescent lanthanide-doped upconverting

nanoparticles, Nano Lett. 11 (2011) 835–840. https://doi.org/10.1021/nl1041929.

[245] H. Schäfer, P. Ptacek, R. Kömpe, M. Haase, Lanthanide-doped NaYF4 nanocrystals in aqueous solution displaying strong up-conversion emission, Chem. Mater. 19 (2007) 1396–1400. https://doi.org/10.1021/cm062385b.

[246] C.D.S. Brites, X. Xie, M.L. Debasu, Instantaneous ballistic velocity of suspended Brownian nanocrystals measured by upconversion nanothermometry, Nat. Nanotechnol. 11 (2016) 851. https://doi.org/10.1038/nnano.2016.111.

[247] W.A. Pisarski, J. Pisarska, R. Lisiecki, W. Ryba-Romanowski, Sensitive optical temperature sensor based on up-conversion luminescence spectra of Er3+ ions in PbO–Ga2O3–XO2 (X = Ge, Si) glasses, Opt. Mater. (Amst). 59 (2016) 87–90. https://doi.org/10.1016/j.optmat.2016.01.037.

[248] S.F. León-Luis, U.R. Rodríguez-Mendoza, E. Lalla, V. Lavín, Temperature sensor based on the Er3+ green upconverted emission in a fluorotellurite glass, Sensors Actuators, B Chem. 158 (2011) 208–213. https://doi.org/10.1016/j.snb.2011.06.005.

[249] L.A. Risebergt, H.W. Moos, Multiphonon Orbit-Lattice Relaxation of Excited States of Rare-Earth Ions in Crystals, Phys. Rev. 174 (1968) 429. https://doi.org/https://doi.org/10.1103/PhysRev.174.429.

[250] A. Rohatgi, Webplotdigitizer, Version 4.2. (2019). https://automeris.io/WebPlotDigitizer (accessed March 3, 2020).

[251] X. Huang, J. Liu, H. Pan, C. Tian, H. Zhang, X. Chen, A. Huang, Z. Xiao, Temperature-dependent upconversion luminescence and spectra characteristic of Er 3+ /Yb 3+ co-doped fluorotellurite glasses, J. Lumin. 207 (2019) 41–47. https://doi.org/10.1016/j.jlumin.2018.10.028.

[252] Y. Zhang, J. Li, X. Chai, X. Wang, Y. Li, X. Yao, Enhanced electrical properties, color-tunable up-conversion luminescence, and temperature sensing behaviour in Er-doped Bi3Ti1.5W0.5O9 multifunctional ferroelectric ceramics, J. Appl. Phys. 121 (2017) 0–7. https://doi.org/10.1063/1.4979096.

[253] C. Li, B. Dong, S. Li, C. Song, Er3+-Yb3+ co-doped silicate glass for optical temperature sensor, Chem. Phys. Lett. 443 (2007) 426–429. https://doi.org/10.1016/j.cplett.2007.06.081.

[254] J.K. Cao, F.F. Hu, L.P. Chen, H. Guo, C. Duan, M. Yin, Optical thermometry based on up-conversion luminescence behavior of Er3+-doped KYb2F7nano-crystals in bulk glass ceramics, J. Alloys Compd. 693 (2017) 326–331. https://doi.org/10.1016/j.jallcom.2016.09.163.

[255] J.K. Cao, F.F. Hu, L.P. Chen, H. Guo, C. Duan, M. Yin, Wide-range thermometry based on green up-conversion luminescence of K3LuF6:Yb3+/Er3+ bulk oxyfluoride glass ceramics, J. Am. Ceram. Soc. 100 (2017) 2108–2115. https://doi.org/10.1111/jace.14606.

[256] X. Li, J. Cao, Y. Wei, Z. Yang, H. Guo, Optical Thermometry Based on Up-Conversion Luminescence Behavior of Er3+ -Doped Transparent Sr2YbF7 Glass-Ceramics, J. Am. Ceram. Soc. 98 (2015) 3824–3830. https://doi.org/10.1111/jace.13804.

[257] D. Chen, Z. Wan, Y. Zhou, P. Huang, J. Zhong, M. Ding, W. Xiang, X. Liang, Z. Ji, Bulk glass ceramics containing Yb3+/Er3+: β-NaGdF4 nanocrystals: Phase-separation-controlled crystallization, optical spectroscopy and upconverted temperature sensing behavior, J. Alloys Compd. 638 (2015) 21–28. https://doi.org/10.1016/j.jallcom.2015.02.170.

[258] United States Environmental Protection Agency, Children’s Health Month: EPA Offers nearly $30 million to Support Cleaner Water and Air for America’s Schoolchildren, (n.d.). https://archive.epa.gov/epa/newsreleases/childrens-health-month-epa-offers-nearly-30-million-support-cleaner-water-and-air.html (accessed September 8, 2020).

[259] C. Wang, C. Yu, Detection of chemical pollutants in water using gold nanoparticles as sensors: a review, Rev. Anal. Chem. 32 (2013) 1–14.

[260] C. Yu, Y. Guo, H. Liu, N. Yan, Z. Xu, G. Yu, Y. Fang, Y. Liu, Ultrasensitive and selective sensing of heavy metal ions with modified graphene, Chem. Commun. 49 (2013) 6492–6494.

[261] J.D.S. Newman, J.M. Roberts, G.J. Blanchard, Optical organophosphate sensor based upon gold nanoparticle functionalized fumed silica gel, Anal. Chem. 79 (2007) 3448–3454.

[262] N.M. Nawi, S. Abdullah, A.A.A. Bakar, Gold nanoparticles/graphene oxide/polyaniline nanocomposites film as sensitive LSPR-based sensor for Pb (II) ions detection, in: 2014

IEEE 5th Int. Conf. Photonics, IEEE, 2014: pp. 188–190.

[263] N. Misra, V. Kumar, N.K. Goel, L. Varshney, Radiation synthesized poly (n-vinyl-2-pyrrolidone)-stabilized-gold nanoparticles as LSPR-based optical sensor for mercury ions estimation, J. Nanoparticle Res. 17 (2015) 279.

[264] Y. Kim, R.C. Johnson, J.T. Hupp, Gold nanoparticle-based sensing of “spectroscopically silent” heavy metal ions, Nano Lett. 1 (2001) 165–167.

[265] I. Klimant, M. Otto, A fiber optical sensor for heavy metal ions based on immobilized xylenol orange, Microchim. Acta. 108 (1992) 11–17.

[266] T.-J. Lin, M.-F. Chung, Using monoclonal antibody to determine lead ions with a localized surface plasmon resonance fiber-optic biosensor, Sensors. 8 (2008) 582–593.

[267] R. Bharadwaj, S. Mukherji, Gold nanoparticle coated U-bend fibre optic probe for localized surface plasmon resonance based detection of explosive vapours, Sensors Actuators B Chem. 192 (2014) 804–811.

[268] T.-J. Lin, M.-F. Chung, Detection of cadmium by a fiber-optic biosensor based on localized surface plasmon resonance, Biosens. Bioelectron. 24 (2009) 1213–1218.

[269] T.C. Ho, M.Z.M. Jafri, L.H. San, M.Y. Chong, Detection of heavy metal ions in aqueous solution using fiber optic sensor, in: 2012 Int. Conf. Comput. Commun. Eng., IEEE, 2012: pp. 267–270.

[270] K. Bhavsar, E. Hurston, R. Prabhu, G.P. Joseph, Fibre optic sensor to detect heavy metal pollutants in water environments, in: Ocean. 2017-Aberdeen, IEEE, 2017: pp. 1–4.

[271] R. Raghunandhan, L.H. Chen, H.Y. Long, L.L. Leam, P.L. So, X. Ning, C.C. Chan, Chitosan/PAA based fiber-optic interferometric sensor for heavy metal ions detection, Sensors Actuators B Chem. 233 (2016) 31–38.

[272] A.D. McFarland, C.L. Haynes, C.A. Mirkin, R.P. Van Duyne, H.A. Godwin, Color my nanoworld, J. Chem. Educ. 81 (2004) 544A.

[273] J. Cao, E.K. Galbraith, T. Sun, K.T.V. Grattan, Effective surface modification of gold nanorods for localized surface plasmon resonance-based biosensors, Sensors Actuators B Chem. 169 (2012) 360–367. https://doi.org/10.1016/J.SNB.2012.05.019.

[274] C.F. Bohren, D.R. Huffman, Absorption and scattering of light by small particles, John

Wiley & Sons, 2008.

[275] P.B. Johnson, R.-W. Christy, Optical constants of the noble metals, Phys. Rev. B. 6 (1972) 4370.

[276] P. Dhara, R. Kumar, L. Binetti, H.T. Nguyen, L.S. Alwis, T. Sun, K.T. V Grattan, Optical fiber-based heavy metal detection using the Localized Surface Plasmon Resonance technique, IEEE Sens. J. 19 (2019) 8720–8726.

[277] N.D. Burrows, W. Lin, J.G. Hinman, J.M. Dennison, A.M. Vartanian, N.S. Abadeer, E.M. Grzincic, L.M. Jacob, J. Li, C.J. Murphy, Surface chemistry of gold nanorods, Langmuir. 32 (2016) 9905–9921.

[278] K. Park, L.F. Drummy, R.C. Wadams, H. Koerner, D. Nepal, L. Fabris, R.A. Vaia, Growth mechanism of gold nanorods, Chem. Mater. 25 (2013) 555–563.

[279] T. Kitamura, Y. Niidome, Colloidal Dispersion of Gold Nanorods and Gold-Silver Core-Shell Nanorods in Polar Organic Solvents, Bull. Chem. Soc. Jpn. 90 (2017) 161–168.

[280] J. Pérez-Juste, I. Pastoriza-Santos, L.M. Liz-Marzán, P. Mulvaney, Gold nanorods: synthesis, characterization and applications, Coord. Chem. Rev. 249 (2005) 1870–1901.

[281] B. Jang, J.-Y. Park, C.-H. Tung, I.-H. Kim, Y. Choi, Gold nanorod- photosensitizer complex for near-infrared fluorescence imaging and photodynamic/photothermal therapy in vivo, ACS Nano. 5 (2011) 1086–1094.

[282] N. Elahi, M. Kamali, M.H. Baghersad, Recent biomedical applications of gold nanoparticles: A review, Talanta. 184 (2018) 537–556.

[283] C.J. Murphy, H.-H. Chang, P. Falagan-Lotsch, M.T. Gole, D.M. Hofmann, K.N.L. Hoang, S.M. McClain, S.M. Meyer, J.G. Turner, M. Unnikrishnan, others, Virus-Sized Gold Nanorods: Plasmonic Particles for Biology, Acc. Chem. Res. (2019).

[284] N.S. Abadeer, C.J. Murphy, Recent Progress in Cancer Thermal Therapy Using Gold Nanoparticles, J. Phys. Chem. C. (2016). https://doi.org/10.1021/acs.jpcc.5b11232.

[285] J. Cao, E.K. Galbraith, T. Sun, K.T. V Grattan, Cross-comparison of surface plasmon resonance-based optical fiber sensors with different coating structures, IEEE Sens. J. 12 (2012) 2355–2361.

[286] X. Lu, L. Tao, D. Song, Y. Li, F. Gao, Bimetallic Pd@ Au nanorods based ultrasensitive

acetylcholinesterase biosensor for determination of organophosphate pesticides, Sensors Actuators B Chem. 255 (2018) 2575–2581.

[287] C. Martín-Sánchez, G. González-Rubio, P. Mulvaney, A. Guerrero-Martínez, L.M. Liz-Marzán, F. Rodríguez, Monodisperse Gold Nanorods for High-Pressure Refractive Index Sensing, J. Phys. Chem. Lett. 10 (2019) 1587–1593. https://doi.org/10.1021/acs.jpclett.9b00636.

[288] C. Wang, J. Irudayaraj, Gold nanorod probes for the detection of multiple pathogens, Small. 4 (2008) 2204–2208.

[289] N.J. Durr, T. Larson, D.K. Smith, B.A. Korgel, K. Sokolov, A. Ben-Yakar, Two-photon luminescence imaging of cancer cells using molecularly targeted gold nanorods, Nano Lett. 7 (2007) 941–945.

[290] Y.-S. Chen, Y. Zhao, S.J. Yoon, S.S. Gambhir, S. Emelianov, Miniature gold nanorods for photoacoustic molecular imaging in the second near-infrared optical window, Nat. Nanotechnol. 14 (2019) 465.

[291] S. Mubeen, J. Lee, W. Lee, N. Singh, G.D. Stucky, M. Moskovits, On the plasmonic photovoltaic, ACS Nano. 8 (2014) 6066–6073.

[292] X. Huang, I.H. El-Sayed, W. Qian, M.A. El-Sayed, Cancer cell imaging and photothermal therapy in the near-infrared region by using gold nanorods, J. Am. Chem. Soc. 128 (2006) 2115–2120.

[293] M.R.K. Ali, M.A. Rahman, Y. Wu, T. Han, X. Peng, M.A. Mackey, D. Wang, H.J. Shin, Z.G. Chen, H. Xiao, Efficacy, long-term toxicity, and mechanistic studies of gold nanorods photothermal therapy of cancer in xenograft mice, Proc. Natl. Acad. Sci. 114 (2017) E3110–E3118.

[294] B. Nikoobakht, M.A. El-Sayed, Preparation and growth mechanism of gold nanorods (NRs) using seed-mediated growth method, Chem. Mater. 15 (2003) 1957–1962.

[295] C. Ji, P.C. Searson, Synthesis and characterization of nanoporous gold nanowires, J. Phys. Chem. B. 107 (2003) 4494–4499.

[296] K. Esumi, K. Matsuhisa, K. Torigoe, Preparation of rodlike gold particles by UV irradiation using cationic micelles as a template, Langmuir. 11 (1995) 3285–3287.

[297] L. Scarabelli, A. Sánchez-Iglesias, J. Pérez-Juste, L.M. Liz-Marzán, A “Tips and Tricks” Practical Guide to the Synthesis of Gold Nanorods, J. Phys. Chem. Lett. (2015). https://doi.org/10.1021/acs.jpclett.5b02123.

[298] S. Eustis, M.A. El-Sayed, Determination of the aspect ratio statistical distribution of gold nanorods in solution from a theoretical fit of the observed inhomogeneously broadened longitudinal plasmon resonance absorption spectrum, J. Appl. Phys. (2006). https://doi.org/10.1063/1.2244520.

[299] S. Das, Binary Solutions for Overdetermined Systems of Linear Equations, (2011).

[300] G. Williams, Overdetermined systems of linear equations, Am. Math. Mon. 97 (1990) 511–513.

[301] J.E. Parks, R. Popovtzer, A. Agrawal, N.A. Kotov, A. Popovtzer, J. Balter, T.E. Carey, R. Kopelman, Y.-B. Lu, X. Kong, X. Chen, D.G. Cooke, H. Guo, I. Weiner ’01, T.D. Donnelly, I. Weiner, M. Rust, T.D. Donnelly, A. Ertü, C.P. Mauch, F. Hellal, F. Förstner, T. Keck, K. Becker, MATLAB version 9.1.0.441655 (R2016b), (2016). http://dx.doi.org/10.1119/1.1311785 (accessed February 23, 2017).

[302] W.S. Rasband, ImageJ, U. S. National Institutes of Health, Bethesda, Maryland, USA, (1997). https://imagej.net/Welcome (accessed August 20, 2011).

[303] A. Rohatgi, WebPlotDigitizer,{Version 4.2}, (2019).

[304] T. Textor, M.M.G. Fouda, B. Mahltig, Deposition of durable thin silver layers onto polyamides employing a heterogeneous Tollens’ reaction, Appl. Surf. Sci. 256 (2010) 2337–2342.

[305] A. Anwar, A. Minhaz, N.A. Khan, K. Kalantari, A.B.M. Afifi, M.R. Shah, Synthesis of gold nanoparticles stabilized by a pyrazinium thioacetate ligand: A new colorimetric nanosensor for detection of heavy metal Pd (II), Sensors Actuators B Chem. 257 (2018) 875–881.

[306] A. Sugunan, C. Thanachayanont, J. Dutta, J.G. Hilborn, Heavy-metal ion sensors using chitosan-capped gold nanoparticles, Sci. Technol. Adv. Mater. 6 (2005) 335–340. https://doi.org/10.1016/j.stam.2005.03.007.

[307] Z. He, H. Yin, C.-C. Chang, G. Wang, X. Liang, Interfacing DNA with Gold Nanoparticles for Heavy Metal Detection, Biosensors. 10 (2020) 167.

[308] Y. Gan, T. Liang, Q. Hu, L. Zhong, X. Wang, H. Wan, P. Wang, In-situ detection of cadmium with aptamer functionalized gold nanoparticles based on smartphone-based colorimetric system, Talanta. 208 (2020) 120231.

[309] W. Haiss, N.T.K. Thanh, J. Aveyard, D.G. Fernig, Determination of size and concentration of gold nanoparticles from UV-Vis spectra, Anal. Chem. 79 (2007) 4215–4221. https://doi.org/10.1021/ac0702084.

Appendix 1

```
close all; clc;clearvars;

% Reading exp. value of RI from Johnson & Christy (1972) given at the end of program
experimental_refractive_index = data_john_christy();
wavelength_john = experimental_refractive_index (:,1);
n_exp = experimental_refractive_index (:,2);
k_exp = experimental_refractive_index (:,3);


% reading experimental values
filename = 'gnp.Sample'; %%% UV_VIS spectrum file name (without header):
filename = [filename '.csv']; %%%%  UV-Vis file format (wavelength, Absorption (nm))
data_exp = load (filename);
absorb_exp1 = data_exp (101:601,2);
absorb_exp1_norm = absorb_exp1./max(absorb_exp1);
lambda_exp = data_exp (101:601,1);
len = length(lambda_exp);

%interpolation of experimental epsilon data over 300 to 900 at step of 1
ref_real_interpolated = interp1(wavelength_john, n_exp,lambda_exp,'spline');
ref_imag_interpolated = interp1(wavelength_john, k_exp,lambda_exp,'spline');

%calculating relative permittivity from ref. index data
epsilon_exp = (ref_real_interpolated+1i.*ref_imag_interpolated).^2;
epsilon_real_interpolated = real(epsilon_exp);
epsilon_imag_interpolated = imag(epsilon_exp);

ref_medium = 1.333;
radius = 44;

for i = 1:len
lambda = lambda_exp(i);
ref_sphere_real = ref_real_interpolated(i);
ref_sphere_img = ref_imag_interpolated(i);
n_angle = 11;

S1 = zeros(1,(2*n_angle-1));
S2 = zeros(1,(2*n_angle-1));
tau = zeros(1,n_angle);
pi_n = zeros(1,(n_angle));
pi_n_0 = zeros(1,(n_angle));
pi_n_1 = ones(1,(n_angle));

ref_relative = ref_sphere_real+1j*ref_sphere_img;
x = 2*pi*radius*ref_medium/lambda; % size parameter

d_angle = 1.570796327/(n_angle-1);

%%%%%%% program for calculating scattering

dx = x;
```

```
y = x*ref_relative;
x_stop = round(x + 4*x^(1/3)+2);
N_stop = round(max(x_stop,abs(y)))+15;
N_stop_2 = N_stop+2;
j = 1:n_angle;
theta = (j-1)*d_angle;
mu = cos(theta);
%%%%%%% calculating D by backward recurrence
D = zeros(1,N_stop);
for n = N_stop:-1:2
 D(n-1) = (n/y)-(1/(D(n)+(n/y)));
end
%%%%%%% upward recurrence
psi_n = zeros(1,N_stop_2);
chi = zeros(1,N_stop_2);
ksi_n = zeros(1,N_stop_2);
psi_n(1) = cos(dx);
psi_n(2) = sin(dx);
chi(1)= -sin(x);
chi(2)= cos(x);
ksi_n(1)= psi_n(1)-1j.*chi(1);
ksi_n(2)= psi_n(2)-1j.*chi(2);
Q_sca = 0;
for n = 1:N_stop
 FN = (2*n+1)/(n*(n+1));
 psi_n(n+2) = ((2*n-1)/dx)*psi_n(n+1)-psi_n(n);
 chi(n+2) = ((2*n-1)/dx)*chi(n+1)-chi(n);
 ksi_n(n+2) = psi_n(n+2) - 1j*chi(n+2);
 a_num = (D(n)/ref_relative + n/x)*psi_n(n+2) -psi_n(n+1);
 a_deno = (D(n)/ref_relative + n/x)*ksi_n(n+2) -ksi_n(n+1);
 an = a_num/a_deno;
 b_num = (ref_relative*D(n)+ n/x)*psi_n(n+2) -psi_n(n+1);
 b_deno = (ref_relative*D(n) + n/x)*ksi_n(n+2) -ksi_n(n+1);
 bn = b_num/b_deno;
 Q_sca = Q_sca+(2*n+1)*((abs(an))^2+(abs(bn))^2);
%%%%%%% for different polarization
 for j = 1:n_angle
     jj = 2*n_angle-j;
     pi_n(j)= pi_n_1(j);
     tau(j) = n*mu(j)*pi_n(j)-(n+1)*pi_n_0(j);
     S1(j) = S1(j)+FN*(an*pi_n(j)+bn*tau(j));
     S2(j) = S2(j)+FN*(bn*pi_n(j)+an*tau(j));
     P = (-1)^(n-1);
     T = (-1)^n;
     if(j ~= jj)
      S1(jj) =S1(jj)+FN*(an*pi_n(j)*P+bn*tau(j)*T);
      S2(jj) =S2(jj)+FN*(bn*pi_n(j)*P+an*tau(j)*T);
     end
 end
    RN = n+1;
 for j = 1:n_angle
     pi_n_1(j) = ((2*RN-1)/(RN-1))*mu(j)*pi_n(j)-((RN/(RN-1))*pi_n_0(j));
     pi_n_0(j)=pi_n(j);
 end


end
Q_sca_array(i) = (2/(x^2))*Q_sca;
```

```
Q_ext_array(i) = (4/(x^2))*real(S1(1));
Q_back_array(i) = (4/(x^2))*abs(S1(2*n_angle-1))^2;
end
Absorb_calculated = pi*(radius)^2.*Q_ext_array./2.303;
Absorb_calculated_norm = Absorb_calculated./max(Absorb_calculated);
Q_ext_array_norm = Q_ext_array./max(Q_ext_array);

figure();
plot(lambda_exp,Q_ext_array_norm,lambda_exp,absorb_exp1./max(absorb_exp1),'Linewidth',6);
set ( gca , 'FontSize' , 30 , 'fontweight' , 'b' , 'FontName' , 'Times New Roman') ;
xlabel ( 'Wavelength(nm)' , 'FontSize' , 30 , 'fontweight' , 'b' ,'FontName' , 'Times New
Roman') ;
ylabel ( 'Absorbance (a.u.)', 'FontSize' , 30 , 'fontweight' , 'b', 'FontName' , 'Times New
Roman' ) ;
legend ('Modelling','Experimental');
xlim([400,800]);

%%%% GOld refractive index were taken from following reference
% P.B. Johnson and R.W. Christy, “Optical constants of the noble metals,” Phys. Rev. B, vol.
6, pp. 4370, 1972.
% Data format [wavelength (nm), real (refractive index), img (refractive_index)]

function y = data_john_christy()
y = [983.968254       0.22    6.350
    891.942446 0.17    5.663
    821.0596026       0.16    5.083
    755.9756098       0.14    4.542
    704.4318182       0.13    4.103
    659.4680851       0.14    3.697
    616.8159204       0.21    3.272
    582.0657277       0.29    2.863
    548.5840708       0.43    2.455
    520.9243697       0.62    2.081
    495.9200000 1.04    1.833
    471.4068441       1.31    1.849
    450.8363636       1.38    1.914
    430.4861111       1.45    1.948
    413.2666667       1.46    1.958
    397.3717949       1.47    1.952
    381.4769231       1.46    1.933
    367.8931751       1.48    1.895
    354.2285714       1.5     1.866
    342.4861878       1.48    1.871
    331.4973262       1.48    1.883
    320.3617571       1.54    1.898
    310.726817 1.53    1.893
    300.9223301       1.53    1.889
    292.4056604       1.49    1.878];
end
```

Appendix 2

```
close all; clc;clearvars;
```

%%%% Reading exp. value of RI from Johnson & Christy (1972) given at the end of program

```
experimental_refractive_index = data_john_christy();
wavelength_john = experimental_refractive_index (:,1);
n_exp = experimental_refractive_index (:,2);
k_exp = experimental_refractive_index (:,3);

%%%% reading experimental UV-Vis values from external file
filename = 'example.Sample'; %%% UV_VIS spectrum file name (without header):
filename = [filename '.csv']; %%%%  UV-Vis file format (wavelength, Absorption (nm))
UV_Vis_data_exp = load (filename);

% finding row number corresponding to wavelength 400 nm, 617 nm & 1000
...wavelength_index is a subroutine, whose body is defined in the end

index_400 = wavelength_index(UV_Vis_data_exp (:,1),400);
index_618 = wavelength_index(UV_Vis_data_exp (:,1),618);
index_1000 = wavelength_index(UV_Vis_data_exp (:,1),1000);

%extracting data from UV-VIS spectum file
%LR stands for Longitudinal Resonance

absorb_exp_LR = UV_Vis_data_exp (index_1000:index_618,2);
absorb_exp1_normalized = absorb_exp_LR./max(absorb_exp_LR);
absorb_exp_complete_spectrum_normalized = UV_Vis_data_exp
(index_1000:index_400,2)./max(UV_Vis_data_exp (index_1000:index_400,2));
lambda_complete = UV_Vis_data_exp (index_1000:index_400,1); %% lambda = 400 nm to 1000 nm
lambda_LR = UV_Vis_data_exp (index_1000:index_618,1);
len_lamba = length(lambda_LR);

%interpolation of experimental refractive index data over 300 to 900 at step of 1
ref_real_interpolated = interp1(wavelength_john, n_exp,lambda_LR,'spline');
ref_imag_interpolated = interp1(wavelength_john, k_exp,lambda_LR,'spline');

%calculating relative permittivity from interpolated refractive index data
epsilon_exp_complete = (ref_real_interpolated+1i.*ref_imag_interpolated).^2;
epsilon_real_interpolated = real(epsilon_exp_complete);
epsilon_imag_interpolated = imag(epsilon_exp_complete);

%%%%%%%%%%%%%%%% Applying Gans theory  %%%%%%%%%%%%%%
AR = 2 : 0.2 : 6;
epsilon_medium = 1.77:0.05:2.1;
Absob_coff_transpose = zeros(length(AR),length(lambda_LR));
Absob_coff_transpose_normalized = zeros(length(AR),length(lambda_LR)); %% Normalized
Absorption Coefficient
N = 1; % Initial contribution
V = 1; %volume
% Loop to find AR and Epsilon_medium having minimum Summed Square Error %%%
```

```
% Refer main paper for algorithm
for k = 1:length(epsilon_medium)
    for i = 1:length(AR)
        elong = sqrt (1-(1/(AR(i)^2)));
        PA = ((1-elong^2)/elong^2)*(1./(2*elong)* log ((1+elong)/(1-elong))-1);
        PB = (1-PA)/2;
        PC = PB;
        coff_A = ((1/PA^2).*epsilon_imag_interpolated)./((epsilon_real_interpolated + ((1-
PA)/PA)*epsilon_medium(k)).^2 + epsilon_imag_interpolated.^2);
        coff_B = ((1/PB^2).*epsilon_imag_interpolated)./((epsilon_real_interpolated + ((1-
PB)/PB)*epsilon_medium(k)).^2 + epsilon_imag_interpolated.^2);
        coff_C = coff_B;
        Absob_coff_transpose (i,:) = (2*pi*N*V*(epsilon_medium(k))^(3/2))./(3.*lambda_LR)
.*(coff_A + coff_B + coff_C);
        Absob_coff_transpose_normalized (i,:) = Absob_coff_transpose (i,:) ./
max(Absob_coff_transpose (i,:));
    end
    Absob_coff_norm = transpose(Absob_coff_transpose_normalized);
    factor = 0:0.001:1;
    absorb_exp1_norm_new = absorb_exp1_normalized;
    for i = 1:(length(AR))
        if (i<length(AR))
            trun_coff = Absob_coff_norm(:,i+1:length(AR));
        else
            trun_coff = Absob_coff_norm(:,length(AR));
        end
        trun_coff_tran = transpose (trun_coff);
        factor_1 = factor .* Absob_coff_norm(:,i);

        for j = 1:length(factor)
            absorb_exp1_norm_new_1 = absorb_exp1_norm_new-factor_1(:,j);
            if (i<length(AR))
                P1 =(trun_coff_tran*trun_coff)\trun_coff_tran;
                error_value_1 = P1*absorb_exp1_norm_new_1;
                error_value = trun_coff*error_value_1;
            else
                absorb_exp1_norm_new_1 = absorb_exp1_norm_new;
                error_value = factor_1(:,j);
            end
            SSE(i,j) = transpose(absorb_exp1_norm_new_1-error_value)*(absorb_exp1_norm_new_1-
error_value);
        end
        [min_SSE,min_index] = min(SSE(i,:));
        freq(k,i,1)= factor(min_index);
        absorb_exp1_norm_new = absorb_exp1_norm_new-factor_1(:,min_index);
    end
    fitted_curve= Absob_coff_norm * transpose(freq(k,:));
    error_final = absorb_exp1_normalized-fitted_curve;
    SSE_final(k) = transpose(error_final)*(error_final);
end
[min_SSE_eps,min_index_eps] = min(SSE_final);
epsilon_minimum = epsilon_medium(min_index_eps);


%%%% for plotting complete curve i.e lambda = 400 nm to 1000 nm

%interpolation of experimental epsilon data over 300 to 900 at step of 1
ref_real_interpolated = interp1(wavelength_john, n_exp,lambda_complete,'spline');
```

```
ref_imag_interpolated = interp1(wavelength_john, k_exp,lambda_complete,'spline');

%calculating relative permittivity from ref. index data
epsilon_exp_complete = (ref_real_interpolated+1i.*ref_imag_interpolated).^2;
epsilon_real_interpolated = real(epsilon_exp_complete);
epsilon_imag_interpolated = imag(epsilon_exp_complete);

% intialization corresponding to complete lambda
Absob_coff_transpose = zeros(length(AR),length(lambda_complete));
Absob_coff_transpose_normalized = zeros(length(AR),length(lambda_complete));

% Calculating complete UV-Vis form fitted contribution

for i = 1:length(AR)
    elong = sqrt (1-(1/(AR(i)^2)));
    PA = ((1-elong^2)/elong^2)*(1./(2*elong)* log ((1+elong)/(1-elong))-1);
    PB = (1-PA)/2;
    PC = PB;
    coff_A = ((1/PA^2).*epsilon_imag_interpolated)./((epsilon_real_interpolated + ((1-
PA)/PA)*epsilon_medium(min_index_eps)).^2 + epsilon_imag_interpolated.^2);
    coff_B = ((1/PB^2).*epsilon_imag_interpolated)./((epsilon_real_interpolated + ((1-
PB)/PB)*epsilon_medium(min_index_eps)).^2 + epsilon_imag_interpolated.^2);
    coff_C = coff_B;
    Absob_coff_transpose (i,:) =
(2*pi*N*V*(epsilon_medium(min_index_eps))^(3/2))./(3.*lambda_complete) .*(coff_A + coff_B +
coff_C);
    Absob_coff_transpose_normalized (i,:) = Absob_coff_transpose (i,:) ./
max(Absob_coff_transpose (i,:));
end

Absob_coff_norm = transpose(Absob_coff_transpose_normalized);
fitted_curve_1= Absob_coff_norm * transpose(freq(min_index_eps,:));

% calculating mean & standard deviation
mean = round(sum(AR.*freq(min_index_eps,:))/sum(freq(min_index_eps,:)),1);
variance_sum = (freq(min_index_eps,:).*(AR-mean).^2);
std_deviation = round(sqrt(sum(variance_sum)/sum(freq(min_index_eps,:))),1);


%%%%% plotting figures %%%%%%%%%%%%%%

% plotting uv-vis spectrum
figure ();
p = plot (lambda_complete,absorb_exp_complete_spectrum_normalized,lambda_complete,
fitted_curve_1,'Linewidth',6);
p(1).LineStyle = '-';
p(1).LineWidth = 6;
p(1).Color ='[0,0,1]';
p(2).LineStyle = '--';
p(2).LineWidth = 6;
p(2).Color ='[1,0,0]';
set ( gca , 'FontSize' , 30 , 'fontweight' , 'b' , 'FontName' , 'Times New Roman') ;
xlabel ( 'Wavelength (nm)' , 'FontSize' , 30 , 'fontweight' , 'b' ,'FontName' , 'Times New
Roman') ;
ylabel ( 'Absorption (a.u.)', 'FontSize' , 30 , 'fontweight' , 'b', 'FontName' , 'Times New
Roman' ) ;
legend ( 'Experimental' ,'Fitted Curve') ;
xlim([400,1000]);
```

```
dimension = [0.2 0.5 0.3 0.3];
str = {'SSE:', num2str(min_SSE_eps)};
annotation('textbox',dimension,'String',str,'FitBoxToText','on','FontSize' , 20 ,
'fontweight' , 'b' ,'FontName' , 'Times New Roman');


% plotting contribution
figure();
p = plot (AR,(freq(min_index_eps,:)./sum(freq(min_index_eps,:)))*100);
p(1).LineStyle = '--';
p(1).LineWidth = 2;
p(1).Color ='[0,0,1]';
p(1).Marker = 'o';
p(1).MarkerSize = 10;
p(1).MarkerEdgeColor = '[0,0,1]';
p(1).MarkerFaceColor = '[0,0,1]';
set ( gca , 'FontSize' , 30 , 'fontweight' , 'b' , 'FontName' , 'Times New Roman') ;
xlabel ( 'Aspect Ratio' , 'FontSize' , 30 , 'fontweight' , 'b' ,'FontName' , 'Times New
Roman') ;
ylabel ( 'Contribution (%)', 'FontSize' , 30 , 'fontweight' , 'b', 'FontName' , 'Times New
Roman' ) ;
dimension = [0.2 0.5 0.3 0.3];
str = {'\mu / \sigma:', num2str(mean) num2str(std_deviation)};
annotation('textbox',dimension,'String',str,'FitBoxToText','on','FontSize' , 20 ,
'fontweight' , 'b' ,'FontName' , 'Times New Roman');




%%%% GOld refractive index were taken from following reference
% P.B. Johnson and R.W. Christy, “Optical constants of the noble metals,” Phys. Rev. B, vol.
6, pp. 4370, 1972.
% Data format [wavelength (nm), real (refractive index), img (refractive_index)]

function y = data_john_christy()
y = [983.968254       0.22   6.350
    891.942446 0.17    5.663
    821.0596026       0.16   5.083
    755.9756098       0.14   4.542
    704.4318182       0.13   4.103
    659.4680851       0.14   3.697
    616.8159204       0.21   3.272
    582.0657277       0.29   2.863
    548.5840708       0.43   2.455
    520.9243697       0.62   2.081
    495.9200000 1.04   1.833
    471.4068441       1.31   1.849
    450.8363636       1.38   1.914
    430.4861111       1.45   1.948
    413.2666667       1.46   1.958
    397.3717949       1.47   1.952
    381.4769231       1.46   1.933
    367.8931751       1.48   1.895
    354.2285714       1.5    1.866
    342.4861878       1.48   1.871
    331.4973262       1.48   1.883
    320.3617571       1.54   1.898
    310.726817 1.53    1.893
```

```
    300.9223301        1.53    1.889
    292.4056604        1.49    1.878];
end

% wavelength subroutine Body
function y = wavelength_index(wavelen, wave)
[~, index_400] = min (abs(wavelen(:,1)-wave));
y = index_400;
end
```

Appendix 3

Chemicals used of Gold Nanorods Preparation

1) Cetrltrimethylammoniumbromide (CTAB)
    - Chemical Formula: $C_{19}H_{42}NBr$; Molecular Weight: 364.45 g/mol
    - It is surface capping agent which promotes one-dimensional growth of Nano rods by forming a bilayer on them. It also controls the approach rates of gold ions and ascorbic acid to the seed particles. Therefore, lowering of the CTAB concentration leads to nonrod-shaped particles.

2) Chloroauric acid:
    - Chemical Formula: $HAuCl_4$; Molecular Weight: 393.833 g/mol (trihydrate)
    - It is source of the seed particles (come from seed solution) and gold (Au^{3+}) ions (come from growth solutions). Increasing its content in seed solution will decrease nano-rods length and eventually lead to spherical shaped particles. This is due to less availability of Au^{3+}ions in growth solution per seed particle. Due to same reason, decreasing of Au^{3+} will also results in rounded particles.

3) Sodium borohydride:
    - Chemical Formula: $NaBH_4$; Molecular Weight: 37.83 g/mol
    - It acts as reducing agent which help in in-situ formation of seed particles.

4) Silver Nitrate:
    - Chemical Formula: $AgNO_3$; Molecular Weight: 169.87 g/mol
    - It may form AgBr in the presence of CTAB, which (AgBr) absorbs differentially to the facets of Gold particles, thus promoting 1-D growth.
    - Increasing and decreasing amount of $AgNO_3$ results in formation of nonrod-shaped particles.

5) Ascorbic Acid:
    - Chemical Formula: $C_6H_8O_6$; Molecular Weight: 176.12 g/mol

- It provides necessary pH needed for reduction of Au^{3+} ions to Au^0 acts as reducing agent.
- Increasing the concentration of Ascorbic acid will decrease the aspect ratio.

List of Publications

Journal Papers

1. **R. Kumar**, L. Binetti, H. Nguyen, L. Alwis, A. Agrawal, T. Sun and K. Grattan, "Optical fibre thermometry using ratiometric green emission of an upconverting nanoparticle-polydimethylsiloxane composite." *Sensors & Actuators A: Physical*, 312, (2020), 112083.
2. **R. Kumar**, L. Binetti, H. Nguyen, L. Alwis, A. Agrawal, T. Sun and K. Grattan, "Determination of aspect-ratio distribution of gold nanorods in a colloidal solution using Bellman Principle of Optimality" *Scientific Reports*, 9, (2019), 1-10
3. P. Dhara*, **R. Kumar***, L. Binetti, H. Nguyen, L. Alwis, T. Sun and K. Grattan, "Optical fiber-based heavy metal detection using the Localized Surface Plasmon Resonance technique" *IEEE sensors Journal*, 19, (2019), 8720-8726. ***Equal Contribution**
4. K. P. W. Dissanayak, P. Dhara, **R. Kumar**, S. Ghosh, H. Nguyen, T. Sun and K.Grattan, "Fibre optic chemical sensors for environmental monitoring using sensitive nano-material coatings" *Asian Journal of Physics*, 28, (2019), 567-576. Invited

Conference Papers

1. **R. Kumar**, S. Ghosh, H. Nguyen, T. Sun, K.T.V Grattan, "Portable optical fibre temperature sensor based on green fluorescence emission from NaYF4: (18%) Yb3+, (2%) Er3+ nanoparticle PDMS composite", Nanophotonics Conference 2019, Munich, Germany, 4-6 September 2019
2. **R. Kumar**, P. Dhara, H. Nguyen, T. Sun, K.T.V Grattan, "Optical fiber based upconversion thermometry", *Photonics2018*, Delhi, India, 12-15 December 2018.
3. **R. Kumar**, H. Nguyen, A. Agrawal, T. Sun and Grattan, K. T., "Estimation of the aspect-ratio distribution in chemically synthesized gold nanorods solution using UV-visible absorption spectroscopy", *Journal of Physics: Conference Series*, 1065, August 2018.
4. K. P. W. Dissanayake, **R. Kumar**, H. Nguyen, W. Wu, T. Sun and Grattan, K. T., "Stability of Graphene Oxide encapsulated Gold Nanorods for optical sensing purposes", *Journal of Physics: Conference Series*, 1065, August 2018.